UNIVERSIDAD COMPLUTENSE DE MADRID

FACULTAD DE CIENCIAS FÍSICAS

Departamento de Física de la Tierra, Astronomía y Astrofísica I (Geofísica y Meteorología) (Astronomía y Geodesia)

TESIS DOCTORAL

Modelización físico-numérica 2D y 3D de procesos de subducción. Influencia de las características de las placas superior e inferior y de la interacción con el flujo mantélico

Numerical modeling of suduction processes in 2D and 3D. Influence of the characteristics of the overrinding and subducting plates and interaction with the mantle flow

MEMORIA PARA OPTAR AL GRADO DE DOCTOR

PRESENTADA POR

Juan Rodríguez González

Directoras

Ana M. Negredo Moreno
Magali I. Billen

Madrid, 2013

UNIVERSIDAD COMPLUTENSE DE MADRID

Facultad de Ciencias Físicas

Dpto. de Física de la Tierra, Astronomía y Astrofísisíca I
(Geofísica y Meteorología)

Modelización físico-numérica 2D y 3D de procesos de subducción. Influencia de las características de las placas superior e inferior y de la interacción con el flujo mantélico.

Numerical modeling of subduction processes in 2D and 3D. Influence of the characteristics of the overriding and subducting plates and interaction with the mantle flow.

Memoria presentada por

Juan Rodríguez González

Directoras:

Ana M. Negredo Moreno

Universidad Complutense de Madrid

Magali I. Billen

University of California Davis

To Marta,
You make every minute worth living.

INDEX

AGRADECIMIENTOS

Durante los últimos cinco años he dedicado una enorme parte de mi tiempo al trabajo y a esta tesis, por lo que ha pasado ha formar parte de mi vida. Afortunadamente, no la más importante. La gente con la que he compartido este camino es la que ha conseguido que cada día merezca la pena. Por eso, gracias.

En primer lugar tengo que darle las gracias a Ana Negredo, mi directora de tesis. Gracias no solo por todo lo que he aprendido durante estos años y tu enorme apoyo profesional. Gracias también por estar siempre pendiente de mi carrera y mi futuro. Gracias por haber ayudado a que la investigación sea algo apasionante interesante y divertido, a pesar de las lamentables trabas con las que nos encontramos en esta profesión. Pero sobre todo, muchas gracias por ser más que una jefa y ser también una amiga.

I would also like to thank Magali Billen for her help during the thesis writing process and her support during my visits to Davis. I did not know that it was possible to learn so much in such a short time.

Quiero también agradecer al equipo de dirección y a todos mis compañeros del departamento (tanto PAS como PDI) el apoyo durante estos años y las facilidades que me han puesto durante la fase final de la elaboración de esta tesis. Gracias en especial a Marisa Osete, por su ayuda en distintos momentos y por las ocasionales conversaciones sobre geofísica. Muchas gracias también a aquellos con los que he compartido docencia: Javi, Maurizio, Greg, Fátima y Belén. Da gusto poder aprender cuando estás enseñando.

Una mención especial merecen aquellos con los que he compartido más que una mera relación laboral, porque afortunadamente no todo ha sido trabajo. Gracias a los otros tres "mediocres" por esos partidos de pádel de alto nivel. Gracias a Fátima, me resulta difícil especificar por qué, pero creo que mereces una mención especial en estas líneas. Gracias a Álvaro, Jorge, Javi (todos ellos), Marta (Ábalos y Martín, obviamente), Teresa, Irene (Polo y Melero), Belén, Maurizio, Elsa, Luis, Victor y Juan Luis. Gracias a todos por las conversaciones, debates, risas y discusiones compartidas entre cafés, cañas, comidas y copas, tanto dentro como fuera de la facultad. Y gracias a todos aquellos con los que he coincidido durante largas horas en el 213, el despacho donde empecé y, contra todo pronóstico, voy a terminar. Sobre todo gracias a Javi y a Sara, que son los que más me han sufrido. Gracias Javi por esas tormentas de surrealismo que

hacen posible sobrevivir a tantas horas de trabajo. Y gracias Sara por no tener demasiado en cuenta mi mal humor y mis bordearías y gracias por no dejar de contarme tus pequeñas historias.

Grazie anche a Eugenio Carminati, per i suoi insegnamenti su geologia, il suo aiuto, la collaborazione scientifica e tutta la pazienza che ha avuto nel corso di questi anni.

Thanks also to everyone on Magali Billen's group: John, Pierre, Katrina and Joy. I really hope I have the chance to work with all of you again. Thanks also to the rest of the friends I made in Davis for making me feel closer to home.

Muchas gracias también al resto de gente que no tiene nada que ver con la geofísica. Muchas gracias a Juanra, mi padre, que obviamente es responsable de que haya llegado hasta aquí. Gracias por apoyarme siempre para que me dedicase a lo que me gusta y gracias por hacer de tu principal preocupación que fuese una mejor persona. Gracias también a mi madre, por ayudar a hacerme quien soy hoy, me habría gustado poder compartirlo con ella. Gracias al resto de mi familia, en especial a Nieves, con la que he aprendido que dos personas completamente diferentes pueden compartir grandes momentos. Gracias a todos mis amigos: "Los Alforjas" (presentes y pasados), "los de la carrera" y "los del Erasmus" . Dudo que ninguno llegue a leer esto, pero sin ellos el camino recorrido habría sido realmente aburrido.

Por último, y por ello más importante, quiero darle las gracias a Marta. Por todo.

Este trabajo ha sido realizado gracias a una beca predoctoral de la Universidad Complutense de Madrid entre Enero y Julio de 2008 y una beca FPU del Gobierno de España entre Agosto de 2008 y Diciembre de 2012. Este trabajo también ha sido desarrollado gracias a los proyectos TOPO-IBERIA CSD2006-00041 del MEC y 3DLOC CGL2009-13103 del MICINN; y a la financiación para grupos de investigación de la UCM. Mi primera estancia en la Universidad de California Davis (cuatro meses en el año 2010) fue financiada dentro del programa FPU y la segunda estancia (cuatro meses en 2012) fue financiada por el programa de movilidad del CSIC. Los resultados de modelización en 3D han sido obtenidos en los *clusters Amala* e *Ymir* del grupo de la Profesora Magali I. Billen en la Universidad de California Davis.

RESUMEN/ SUMMARY

Resumen

Introducción

La dinámica del hundimiento de litosfera en las zonas de subducción ejerce un control importante en la evolución del sistema manto-placas tectónicas. En consecuencia, se han desarrollado durante las últimas décadas una gran cantidad de estudios centrados en diferentes tipos de observaciones, así como en modelización analítica, en laboratorio y numérica. Sin embargo, algunos aspectos importantes del proceso de subducción aún no se comprenden bien, como es el caso de la contribución relativa de los diferentes factores que causan la variabilidad observada en los ángulos de subducción. Por ejemplo, cabría esperar que la litosfera joven, y por tanto relativamente caliente y poco densa, causara una flotabilidad negativa pequeña y en consecuencia su buzamiento fuese menor. Sin embargo, esto contrasta con el elevado buzamiento de la litosfera joven de la placa de Cocos bajo Centroamérica.

Además del torque gravitacional asociado a la flotabilidad de la laja (*slab*), interviene un torque de succión hidrodinámica generado por el flujo inducido en la cuña mantélica (entre el techo de la laja y la base de la placa superior). Este torque tiende a succionar la laja hacia arriba y disminuir su buzamiento. El balance entre estos torques controla el buzamiento resultante de la laja. Como punto de partida de este trabajo, se hipotetizó que el estado térmico de la placa superior debía ejercer un importante control sobre la estructura de viscosidad en esta cuña, y por tanto sobre el torque de succión hidrodinámica. Previamente a este trabajo de tesis doctoral, se había estudiado con modelos numéricos 2D el efecto del espesor de la placa superior, pero no se había realizado un estudio de los efectos del estado térmico de dicha placa en la dinámica de la subducción. Además, se observa comúnmente importantes heterogeneidades térmicas de la placa superior, tanto en dirección paralela como perpendicular a la fosa de subducción. Es estudio de la influencia de estas heterogeneidades no se ha realizado en ningún estudio previo a esta tesis y requiere considerar una geometría 3D.

Objetivos

En esta tesis doctoral se desarrolla un estudio exhaustivo de la influencia del estado térmico de la placa superior. Se ha desarrollado modelos numéricos termo-mecánicos en 2D y 3D, con el objetivo de mejorar la comprensión de la dinámica de la subducción y de explorar diferentes factores que pueden jugar un papel importante en la geometría de la laja y el flujo mantélico asociado. Nos planteamos, además, los siguientes objetivos específicos.

- Analizar la influencia del estado térmico tanto de las places superior y subducente en la geometría de la laja.
- Analizar la influencia de un hipotético flujo mantélico horizontal en la geometría de la laja y en la evolución a largo plazo de los procesos de subducción.
- Aumentar el realismo de los modelos incorporando las características 3D. En particular, nos planteamos analizar los efectos de las heterogeneidades térmicas de la placa superior y de la existencia de flujo alrededor de los bordes de la laja en la geometría de la misma y en la distribución de flujo mantélico resultante.

Resultados

Se ha aplicado el método de los elementos finitos para resolver el sistema de ecuaciones acopladas de conservación de la masa, momento y energía para un fluido incompresible. En los Capítulo 3 y 4 se ha desarrollado modelos en los que se fuerza cinemáticamente la subducción, utilizando el código comercial Comsol Multiphysics. Estos modelos predicen que la subducción bajo placas superiores viejas ocurre con ángulos menores. Este efecto es más importante para lajas jóvenes (curvas en color rojo en la Figura 1), además, resulta ser más importante y persistente en el tiempo que el de la edad de la placa que subduce.

Combinando diferentes edades de ambas placas, hemos sido capaces de reproducir un amplio rango de estilos de subducción: plana, de bajo y de alto ángulo. Deducimos que la subducción de la placa de Cocos bajo Norteamérica tiene un ángulo menor que bajo la placa Caribe debido al estado térmico mas caliente de la segunda.

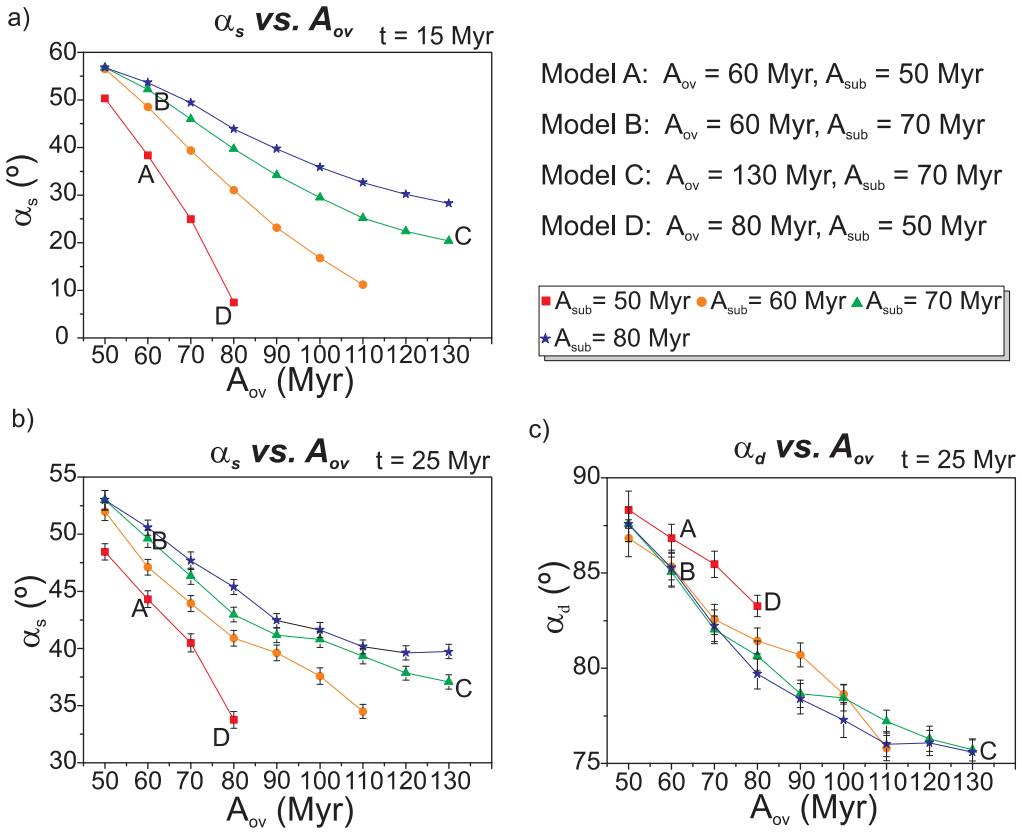

Figura 1: Influencia de la placa superior en el buzamiento de la laja. Buzamiento medio en función de la edad de la placa superior para diferentes edades de la placa subducente, medido (a) entre profundidades de 100 y 200 km (α_s) después de 15 Ma de evolución y (b) después de 25 Ma; (c) buzamiento α_d medido entre 300 y 400 km después de 25 Ma. La letras mayúsculas indican los modelos A-D mostrados en la Figure 3.4. Nótese que la escala del eje vertical es variable.

El objetivo del Capítulo 4 es realizar un análisis sistemático de un flujo mantélico hipotético (ya sea global o regional) en el ángulo y en la evolución a largo plazo de la subducción. Se muestra que este flujo produce desviaciones notables de ángulo de subducción, incluso considerando lajas resistentes.

Finalmente, en el Capítulo 5 se desarrolla una serie de modelos 3D más realistas, donde la subducción es forzada dinámicamente por el propio peso de la laja, utilizando el código abierto CitcomS. El objetivo era generalizar los resultados de la geometría 2D y evaluar el efecto en la geometría de la laja y en el flujo mantélico de las variaciones a lo largo de la fosa del estado térmico de la placa superior. Estos modelos indican que la mayor succión hidrodinámica bajo la porción fría de la placa superior es suficiente para mantener a lo largo del

tiempo las variaciones preexistentes del ángulo de subducción. Además, se muestra que esta succión variable es capaz de deformar lajas inicialmente uniformes, creando variaciones importantes de ángulo de subducción a lo largo de la fosa. Este resultado supone una aportación importante respecto a los modelos 3D recientes, en los que las variaciones de ángulo no se obtenían de manera autoconsistente, sino que eran impuestas y fijadas desde el principio. Debido a la variación de succión hidrodinámica y geometría de la laja, se crean intensas celdas de flujo horizontal en la zona donde cambia el estado térmico de la placa superior. Estas celdas producen una componente de flujo en la dirección paralela a la fosa, lejos de los bordes de la laja, que además no está relacionado con el flujo alrededor de estos bordes.

Cuando se añaden placas laterales en estos modelos 3D, se permite que el material del manto fluya alrededor de los bordes de la laja, lo que genera amplias regiones de flujo paralelo a la fosa, por debajo y por encima de la laja (Figura 2).

A los largo de todos los capítulos, se ha comparado en términos cualitativos los resultados obtenidos con ejemplos reales de zonas de subducción. En particular, se ha discutido las variaciones del ángulo de subducción observadas en las zonas de Centroamérica y Sudamérica en relación con los factores estudiados.

Discusión y Conclusiones

En los modelos desarrollados en esta tesis, se ha realizado simplificaciones para poder aislar los efectos que se deseaba estudiar. Una simplificación importante ha sido imponer una posición fija del límite de placas. En este sentido, una mejora futura que se espera introducir es permitir el movimiento de este límite, lo cual aumentará el realismo de los modelos. Otra mejora que permitirá la comparación directa de las predicciones con los datos de anisotropía sísmica es calcular las direcciones de propagación rápida de ondas de cizalla a partir de las predicciones de distribución 3D de flujo mantélico.

La aplicación futura de los modelos al estudio de zonas concretas de subducción permitirá validar y perfeccionar estos modelos.

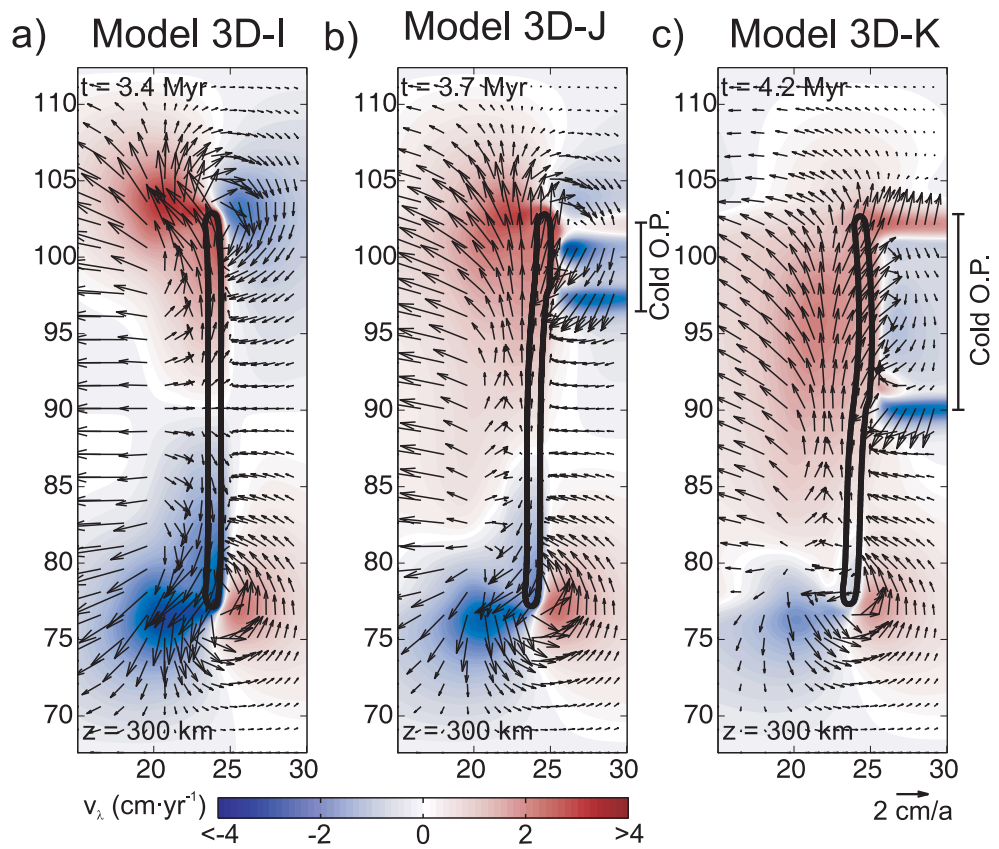

Figura 2: Sección horizontal a 300 km de profundidad que muestra la distribución de velocidades (flechas) en un modelo 3D donde se permite el flujo alrededor de los bordes de la laja. La escala de colores indica la componente de velocidad paralela a la fosa. La línea gruesa indica el contorno de la laja, que subduce de izquierda a derecha. En los modelos con una porción fría en la placa superior (b y c) aparece un importante flujo paralelo a la fosa incluso lejos de los bordes de la laja.

En esta tesis hemos extraído las siguientes conclusiones:

- Las placas de mayor edad son más densas y por tanto están sometidas a un torque gravitacional mayor. Como consecuencia, subducen con un mayor ángulo que placas jóvenes.

- El material del manto bajo una placa superior vieja es más frío y por tanto la succión hidrodinámica es mayor. Como consecuencia, el ángulo de subducción es menor.

- La influencia del estado térmico de la placa superior en el ángulo de subducción es más importante y persistente que la del estado térmico de la placa que subduce.

- Las predicciones son consistentes con las variaciones del ángulo de subducción de la placa de Cocos. La subducción plana o de bajo ángulo se relaciona con la litosfera fría de Norte América, mientras la subducción de alto ángulo se relaciona con la litosfera más caliente de la placa del Caribe.

- Existe una fuerte influencia del flujo mantélico horizontal en la dinámica a largo plazo de la subducción. Para un flujo en el mismo sentido que la subducción el ángulo disminuye con el tiempo, pudiendo dar lugar al acoplamiento de las placas y al cese de la subducción.

- Hemos desarrollado modelos 3D que incluyen geometrías, condiciones de contorno y reologías más realistas.

- La mayor succión bajo las porciones frías de la placa superior es capaz de mantener variaciones preexistentes del ángulo de subducción, e incluso de generar estas variaciones a partir de una laja inicialmente uniforme.

- Las variaciones de succión hidrodinámica producen fuertes variaciones del flujo en la cuña mantélica.

- Los modelos con placas laterales y variaciones de la placa superior predicen la aparición de amplias zonas de flujo paralelo a la fosa, tanto bajo la laja como en la cuña. Esto es consistente con las direcciones de anisotropía sísmica.

Summary

The dynamics of sinking lithosphere at subduction zones has a strong control on the evolution of plate-mantle system. Accordingly, a large number of studies focusing on observational data, as well as analytical, laboratory and numerical models have been developed during the last decades. However, some important aspects of subduction process remain poorly understood, such as the relative contribution of different factors causing the observed variability of slab dip. While the effects of overriding plate thickness on slab dip and on trench motion have been recently studied by means of 2D modeling, a systematic analysis of the effect of overriding plate thermal state has not been performed before this thesis. In the present study, 2D and 3D numerical thermo-mechanical modeling were developed to obtain a better understanding of the dynamics of subduction, and to explore different factors that might play an important role in controlling the geometry of the slab and associated mantle flow.

The finite element method was applied to solve the coupled equations of mass, momentum and energy conservation for an incompressible fluid. In Chapters 3 and 4, 2D numerical models of kinematically-driven subduction using the commercial software Comsol Multiphysics were developed. Modeling results indicate that plates subducting underneath cold overriding plates are predicted to subduct with lower slab dip, and this effect is predicted to be more important and persistent than that of the subducting lithosphere age. The purpose of the study in Chapter 4 is to perform a systematic analysis of the effect of a hypothetical mantle flow (either global or regional) on slab dip and long-term evolution of subduction processes. This mantle flow is shown to produce significant slab dip deviations even for strong slabs.

Finally, more realistic 3D dynamically-driven models with a more complex rheology are developed in Chapter 5, using the open source code CitcomS. The purpose was to generalize the results from 2D modeling and to test the effect of along-trench variations of the thermal state of the overriding both on slab geometry and the resulting pattern of mantle flow. Models of dynamically-driven subduction indicate that the increased suction beneath the cold portion of the overriding plate is enough to maintain though time preexisting variations of the slab dip. Moreover, this variable suction is shown to be even able to deform an

initially uniform slab, creating significant variations on the slab dip along the trench. Due to the variations on the hydrodynamic suction and slab geometry, intense toroidal cells are generated in the region where the thermal state changes. These cells produce a component of trench-parallel flow far away from the edges of the slab, and not related to mantle flow around slab edges. Adding lateral plates to 3D models enables the material from the mantle to flow around the edges of the slab, which leads to wide regions of intense trench-parallel flow both beneath and above the slab.

Through all the chapters, the results obtained in the models were compared on qualitative grounds with natural examples. Slab dip variations found in some subduction zones (e.g., Central and South America) were discussed in terms of the studied factors.

1

INTRODUCTION

1.1. Subduction processes

The subduction process (Figure 1.1) is a vital ingredient of plate tectonics (see *Anderson*, 2001; *Conrad and Lithgow-Bertelloni*, 2002 and references there in). Subduction zones are a major component of the plate-mantle system, where the lithosphere enters into the underlying mantle. Oceanic lithosphere, which was created at oceanic ridges, and sediments, including volatile compounds such as water, are recycled back into the mantle. Once subduction is initiated it may work for several tens of millions years. Subducting slabs are the dominant source of gravitational potential energy, an important driving force for mantle convection and plate tectonics. Earth is the only terrestrial planet in the Solar System with active subduction zones, and it is possible that it is the only planet where the process of subduction as we know it ever occurred. Moreover, it is possible that without subduction, Earth would not have been a suitable place for life to develop, as subduction is a crucial part of the global cycle that maintains the carbon balance between atmosphere, hydrosphere and lithosphere.

Although Plate Tectonics theory was first formulated by Alfred Wegener in 1912, the discovery of subduction was one of the last developments and the concept of complete underthrusting of the oceanic plate was not accepted until after the magnitude 9.2 Alaska earthquake in 1964. Prior to this, deep seismicity was interpreted to occur on a "mega-fault" extending from the surface to a depth of 700 km (*Benioff*, 1954). With the development of regular determination of earthquake focal mechanisms for several of the world's zones of deep seismicity, intermediate and deep earthquakes were properly understood as reflecting the internal deformation of sinking lithosphere (*Isacks and Molnar*, 1969).

The first quantitative studies of subduction dynamics used analytic models that approximated the highly viscous slab as a perfectly rigid plate sinking into the mantle at a fixed dip and rate (*McKenzie*, 1969). This model predicted that the slab sinking into the mantle would induce a corner flow in the wedge between the base of the upper plate and the top of the slab that creates an upward suction force on the top of the slab. Other analytic models showed that steady-state balance between the buoyancy force (causing the slab to sink) and the suction (pulling the slab up) provided an accurate prediction of the average dip of slabs in the upper mantle (*Stevenson and Turner*, 1977; *Tovish et al.*, 1978; see section 3.1).

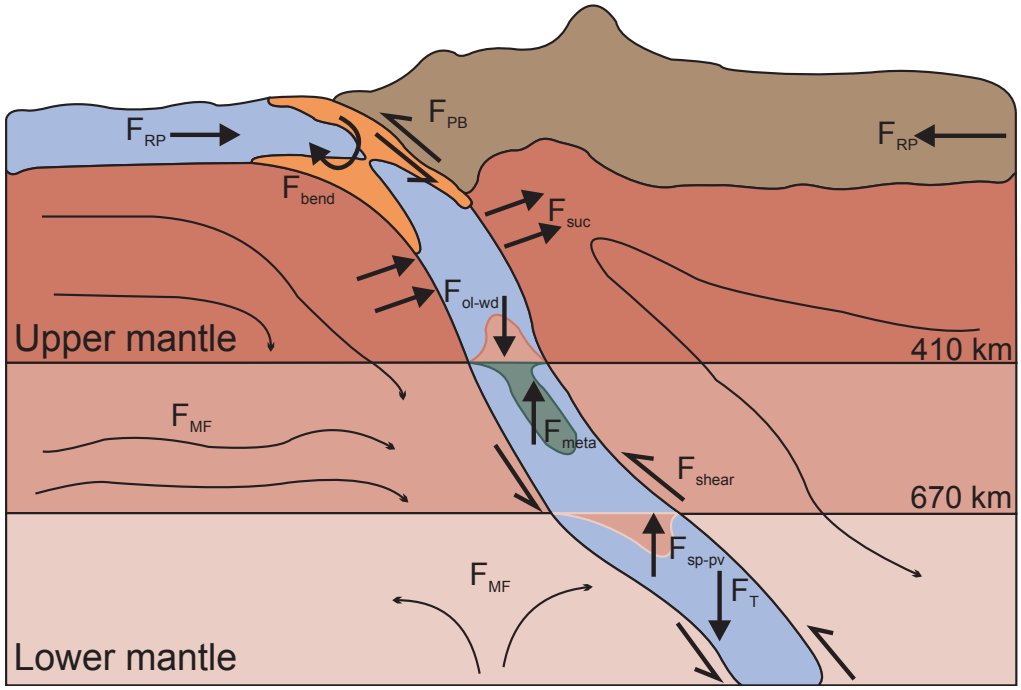

Figure 1.1: Schematic illustration of the forces acting on slabs. Driving forces include negative buoyancy caused by the colder temperature of the slab (F_T) and olivine-wadsleyite phase change at 410 km ($F_{ol\text{-}wd}$) and ridge push (F_{RP}). Resisting forces at shallow depth include bending of the plate in the trench (F_{bend}) and coupling to the overriding plate (F_{PB}). In the upper mantle, subduction is resisted by viscous shear (F_{shear}) and positive buoyancy (lower density) due to the spinel-perovskite phase transition at 660 km ($F_{sp\text{-}pr}$) and/or meta-stable olivine below 410 km (F_{meta}). In addition, flow-induced suction in the mantle wedge (F_{suc}) and large-scale mantle flow (F_{MF}) affect the evolution of the slab. From Billen (2008)

Most of the recent studies involve either laboratory (analog) or numerical simulations. Analog models use laboratory materials to simulate subduction processes setting up a scaled configuration that represents the subduction zone. Numerical models use computers to obtain approximated solutions for the equations of conservation of mass, momentum and energy inside a particular geometry, using specific boundary and initial conditions and rheology (see Chapter 2 for more details). Both modeling techniques have their strengths and weaknesses, and choosing one over the other depends on the specific question being addressed and/or the observations one seeks to understand. Laboratory models, for example, do not include temperature variations and density and viscosity variations are included ad hoc by using different materials. Pressure and temperature dependence of rheology and the implementation of melting, are features that analog models cannot yet reproduce. Moreover, major difficulties

often occur with experiments reproducibility and with extraction of quantitative information. In contrast, one of the main advantages of using analog models is the natural stress-free boundary on the top surface, which is more difficult to incorporate into numerical simulations. In addition, analog models are able to account simultaneously for the solid and fluid behavior of different materials. The main advantages of numerical simulations of slab dynamics are complete quantification of the flow field, inclusion of larger viscosity variations and a more realistic stress-dependent viscosity, the size of the model domain (depth and horizontal extent), and potential to directly include the effects of melting or hydration/dehydration on density and viscosity. The third option is to combine different techniques to study the same problem, and the joint study of laboratory experiments and analytical or numerical methods has a long history in subduction-related fluid dynamics (*Kincaid and Olson*, 1987; *Piromallo et al.*, 2006).

Models of subduction have so far concentrated on two aspects: the first approach is global and focused on reproducing first-order observations, including force-balanced plate motions, the geoid, deep slab anomalies and surface plate velocities and stresses (*Becker and Faccenna*, 2009). The second approach is regional, and studies how an isolated slab enters into the mantle and the forces acting on it. Recent 2D regional models of subduction, have focused on thermal structure (*King*, 2007), composition (*van Hunen et al.*, 2004) and rheology (*Billen*, 2008). Recent advances include the incorporation of laboratory-derived rheologies to test how temperature-dependent viscosities plus plastic yielding may explain slab morphology (e.g., *Billen and Hirth*, 2007; *Čížcová et al.*, 2007) and what processes might assist subduction initiation (*Toth and Gurnis*, 1998).

The improvement of computer technology and numerical methods have made possible the study of time-dependent slab dynamics in three dimensions, which is focused on the main effects of trench motion and toroidal flow around the edges of slabs (see section 5.1). Trenches are not stationary features, but are often found to retreat or advance with respect to the subducting plate and to the lower mantle. Any trench migration has important consequences for tectonics such as back-arc spreading or slab stagnation in the base of the upper mantle (*Piromallo et al.*, 2006; *Stegman et al.*, 2010). Both numerical and laboratory experiments in 3D have shown that shear resistance to subduction at depth can lead to either advancing or retreating motion of the trench depending on the slab

strength (*di Giuseppe et al.*, 2008; *Funiciello et al.*, 2008) or the slab width (*Stegman et al.*, 2006; *Schellart*, 2007).

Regarding the different approaches used to force subduction, there are three main groups of numerical models: fully-kinematic models, dynamically-driven models and kinematically-driven models. In fully-kinematic models, the geometry of the slab and subduction velocity are imposed, and are often used to study local processes, such as melting, slab dehydration, wedge hydration and induced mantle flow (*Bodri and Bodri*, 1978; *Eberle et al.*, 2002; *van Keken et al.*, 2002; *Kneller and van Keken*, 2007; *Becker and Faccenna*, 2009). In dynamically-driven models the slab is allowed to evolve freely, changing its shape and subduction velocity depending and the different forces acting on the slab (e.g., *Schellart et al.*, 2007; *Burkett and Billen*, 2009; *Yamato et al.*, 2009). Finally, kinematically-driven models are somewhere in between, where only the subduction velocity is imposed as a boundary condition, which allows to study the geometry and thermal evolution of the slab and the mantle wedge (*van Hunen et al.*, 2004; *Billen and Hirth*, 2007; *Rodríguez-González et al.*, 2012).

The evolution of subducted slabs depends on the balance of driving and resisting forces, on the way these forces change with depth and time, and on the geometry imposed by the larger-scale tectonic environment (Figure 1.1). Driving forces include ridge-push and slab negative buoyancy related to positive density contrasts due both to compositional and thermal differences with respect to the surrounding mantle. Resisting forces include bending of the lithosphere and frictional plate-coupling at shallow depths, viscous shear in the mantle, and positive buoyancy forces. Large-scale mantle flow and flow-induced pressure anomalies also affect the sinking rate and geometry of subducting lithosphere.

A number of studies have focused on the relative importance of each of the driving and resisting forces and how they depend on the details of the subduction history (e.g., age of the subducting lithosphere, plate boundary dip and mechanical properties, sinking rate, duration of subduction). However, how slabs deform and transmit stresses to the subducting plate remains unclear (e.g., *Conrad and Hager*, 1999; *Conrad and Lithgow-Bertelloni*, 2002; *Buffett and Rowley*, 2006; *Billen and Hirth*, 2007; *Billen*, 2008; *Ribe*, 2010). The ability of slabs to transmit buoyancy forces to the subducting plate depends on the rheology of the slab and mantle, as well as on the evolution of slab dip with time.

Significant slab dip variability can be found between different subduction zones, or even along the same subduction zone (Figure 1.2). According to variations in slab dip, four different styles of subduction have been described: flat subduction, in which the slab reverses its curvature and subducts almost horizontally for hundreds of kilometers, (e.g., Peru); low-angle subduction with slab dips lower than 30º (e.g., Cascades); intermediate-angle subduction, with slab dip between 30º and 60º (e.g., Ryukyu); and high-angle subduction with slab dip greater than 60º (e.g., Marianas). Around 10% of slabs subduct with very low angle, as for example the Nazca plate dipping about 15º under southern Peru (*Barazangi and Isacks*, 1979; *Jarrard*, 1986). Flat subduction can also be found in northern Chile (e.g., *Gutscher et al.*, 2000b) and Central Mexico (e.g., *Suárez et al.*, 1990; *Pérez-Campos et al.*, 2008), where the flat segment is connected to a much steeper portion of the slab at depth. In some regions flat slab subduction is known to be caused by subduction of thick, buoyant crust (e.g., the Yakutat Block beneath southern Alaska; *Christeson et al.*, 2010), while in other regions, such as Central Mexico, the causes are still debated. In addition, different geological observations indicate that the Farallon plate subducted underneath North America plate with a flat (or very low) angle about 65 Ma ago and may be responsible for tectonism far from the plate boundary (*Bird*, 1988; *Schmid et al.*, 2002; *Sigloch et al.*, 2008).

Variations on the slab dip are also important, as they are associated with other geophysical and geochemical features. Lower slab dips have the effect of pushing back the volcanic arc inland and for very low-angle and flat slabs volcanism can be absent due to the absence of asthenospheric wedge between the slab and the overriding plate (*Gutscher et al.*, 2000a). Low-angle subduction can also alter the lithospheric structure and morphology and topography of the overriding plate, leading to shortening and uplifts, especially above flat slabs (*Espurt et al.*, 2008; *Pérez-Gussinyé et al.*, 2008; *Sigloch et al.*, 2008). Great variations along a single slab have been related to increased seismicity due to the high deformation (*Anderson et al.*, 2007) or can even lead to slab tearing, as might be the case of the already subducted Farallon slab (*Sigloch et al.*, 2008). Finally, for low-angle slabs, the seismic energy released due to the high contact area and the high coupling between the overriding plate and the slab is larger than for steep subduction zones.

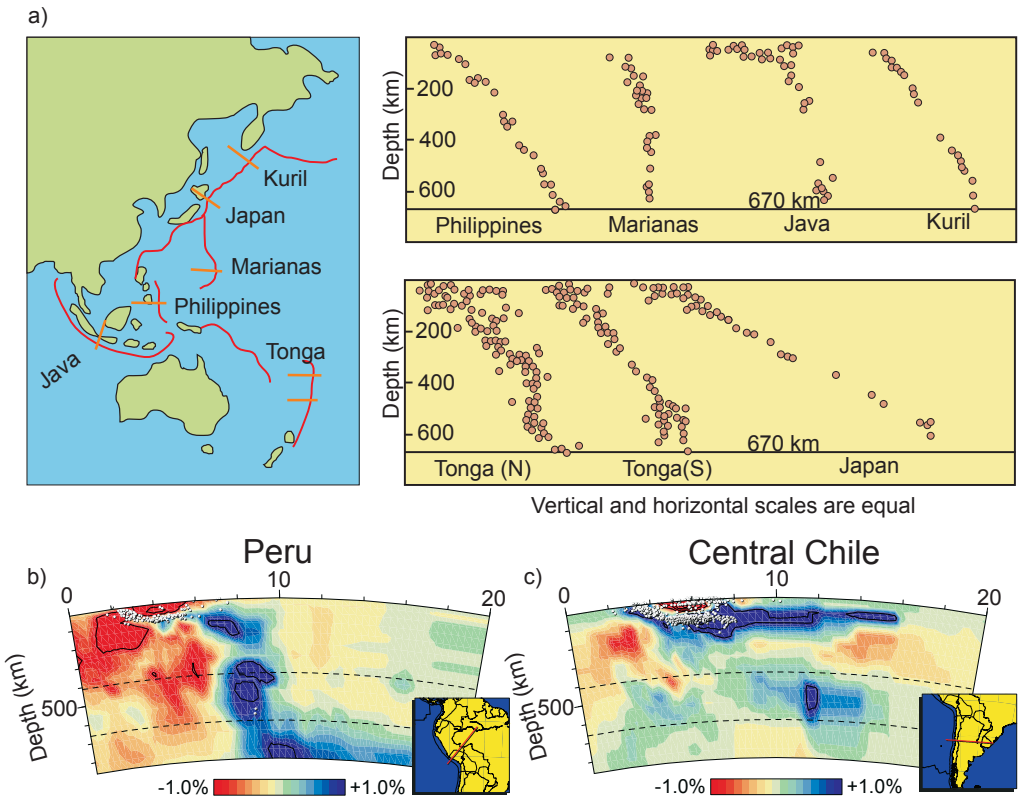

Figure 1.2: Slab dip variability found in nature. a) Wadati-Benioff planes at different subduction zones (*Butler*, 2001). b) and c) Tomographic images from Villaseñor et al., (2003) based on a global P wave propagation model. White points are the projection of earthquakes taking place in a 50 km wide band centered on the tomographic section. b) Subduction beneath Peru (c) Subduction in Chile. Insets show location of tomographic vertical cross-sections.

The causes of slab dip variability remain unclear, although several explanations have been proposed and investigated with analytical (e.g., *Stevenson and Turner*, 1977; *Tovish et al.*, 1978; *Royden and Husson*, 2006; *Ribe*, 2010), numerical (e.g., *Billen*, 2008 and references therein; *di Giuseppe et al.*, 2008; *Tetzlaff and Schmeling*, 2009; *Capitanio et al.*, 2010; *Roda et al.*, 2011) and laboratory models (*Kincaid and Olson*, 1987; *Griffiths et al.*, 1995; *Guillou-Frottier et al.*, 1995; *Funiciello et al.*, 2003; *Schellart*, 2004; *Funiciello et al.*, 2006; *Heuret et al.*, 2007; *Boutelier and Cruden*, 2008; *Funiciello et al.*, 2008; *Butterworth et al.*, 2012). First, it has been proposed that slab dip is affected by the balance between the torque related to slab buoyancy and the torque exerted by hydrodynamic pressure caused by the flow generated under the slab and in the mantle wedge located between the slab and the base of the upper plate (*Stevenson and Turner*, 1977; *Tovish et al.*, 1978).

Second, a number of studies show that slab geometry is significantly influenced by trench migration. In this sense, trench motion with respect to the upper plate is shown to be correlated with slab dip (*Uyeda and Kanamori*, 1979; *Jarrard*, 1986; *Lallemand et al.*, 2005), with advancing trenches generally corresponding to steeper slabs. Trench motion has been investigated either with models including a subducting and overriding plate (e.g., *Kincaid and Olson*, 1987; *Griffiths et al.*, 1995; *Zhong and Gurnis*, 1995; *Yamato et al.*, 2009; *van Dinther et al.*, 2010; *Quinquis et al.*, 2011) or considering only a subducting plate (e.g., *Christensen*, 1996; *Enns et al.*, 2005; *Stegman et al.*, 2006; *Faccenna et al.*, 2007; *Schellart et al.*, 2007).

Third, the interaction between the subducting slab and a hypothetical large scale mantle flow has been proposed as responsible for the difference between eastward and westward dipping slabs (e.g., *Ricard et al.*, 1991; *Doglioni et al.*, 1999). Although this slab-mantle flow interaction should significantly affect slab dip (*Olbertz and Wortel*, 1997; *Boutelier and Cruden*, 2008), no agreement about the relationship between slab polarity and dip has been reached in statistical analyses (*Cruciani et al.*, 2005; *Lallemand et al.*, 2005; *Schellart*, 2007; *Riguzzi et al.*, 2009).

Fourth, slab dip can be affected by the rheology of the slabs and the surrounding mantle (*Cizkova et al.*, 2002; *Bellahsen et al.*, 2005; *Billen and Hirth*, 2005, 2007; *Manea and Gurnis*, 2007). For example, lower viscosity slabs tend to evolve to steep dips, while high viscosity slabs tend to shallow once they enter a higher viscosity lower mantle. Finally, the effects of phase transition on the buoyancy of slabs can also affect evolution of slab dip with time (*Schmeling et al.*, 1999; *Tetzlaff and Schmeling*, 2000; *van Hunen et al.*, 2001; *Tetzlaff and Schmeling*, 2009).

Provided that slap-pull is the main driving force in subduction processes it is expected to find older (and consequently colder) slabs subducting at higher angles than younger slabs (see section 3.1 for more details). However, statistical analyses of slab dip data from a number of transects across different subduction zones (*Jarrard*, 1986; *Cruciani et al.*, 2005; *Lallemand et al.*, 2005) show a poor correlation between slab dip and the age of the subducting lithosphere A_{sub} (Figure 1.3.a and b), indicating that there may be significant influence of other factors, described above, masking the dependence of slab buoyancy on dip.

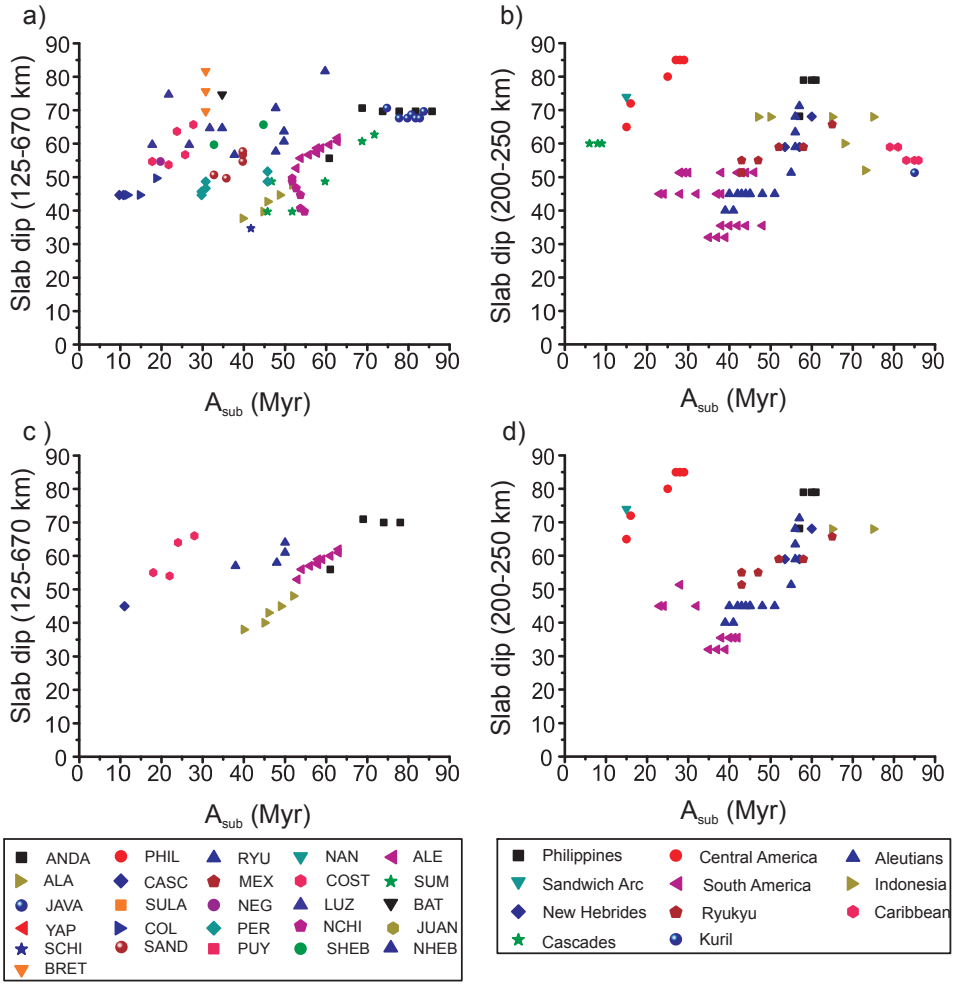

Figure 1.3: Slab dip as function of the age of the subducting plate. Original data from: a) Lallemand et al. (2005) (89 transects) and b) from Cruciani et al. (2005) (94 transects) show only a weak correlation. Panels c) and d) show a strong correlation for the same data as in a) and b) after removing 56 and 45 points, respectively, representing data from near-edge transects and from slabs that sink into the lower mantle. Subducting plate age is measured at the trench and slab dips are measured along transects perpendicular to the trench.

In order to attempt to unmask the slab buoyancy dependence of slab dip, we present data from the statistical analyses by Lallemand et al., (2005) in Figure 1.3.a and by Cruciani et al., (2005) in Figure 1.3.b and have removed data from transects where slab dip is likely affected by other factors (Figure 1.3.c and d; where 56 and 45 transects were removed from Figure 1.3.a and b, respectively). We have removed slab dip data from near-edge transects as they may be affected by the toroidal flow around the slab edges (*Piromallo et al.*, 2006; *Royden and Husson*, 2006; *Schellart et al.*, 2007; *di Giuseppe et al.*, 2008) and data from slabs that

have reached the lower mantle, because the angle of subduction can change due to the viscosity increase in the lower mantle (e.g., *Billen and Hirth*, 2007). As shown in Figure 1.3.c and d, the correlation between slab dip and subducting plate age clearly improves when removing these data, but we can still find "anomalous" data that do not match the expected trend, such as high slab dips in transects across the Central America subduction zone, where the young Cocos plate subducts steeply. Thus it is important to identify, analyze and isolate the other potential factors that might affect slab dip in order to evaluate their relative roles. In particular, variations in the viscosity in the mantle wedge cause variations on the hydrodynamic torque exerted on the slab (*Stevenson and Turner*, 1977; *Tovish et al.*, 1978; see section 3.1) and are therefore expected to play a major role on slab dip. Actually, the different viscosity structure under continental and oceanic overriding plates has been proposed to be responsible for observed steeper subduction under oceanic overriding plates than under continental plates (*Uyeda and Kanamori*, 1979; *Jarrard*, 1986; *Lallemand et al.*, 2005). Lallemand et al. (2005) found that the mean slab dip at depths greater than 125 km is of 70º±11º for oceanic overriding plates but only 53º±12º for continental upper plates. Similarly, Pérez-Gussinyé et al. (2008) found that slabs close to areas of high elastic thickness in the overriding plate have shallower dips, and suggested that the viscosity structure under the overriding plate has a significant influence on the occurrence of flat subduction.

In this context, we argue that the influence of the thermal state of the overriding plate needs to be explored, as it is expected to influence the viscosity structure in the mantle wedge (see section 3.1). While the effects of overriding plate thickness on slab dip and on trench motion have been recently studied (*Capitanio et al.*, 2010; *Capitanio et al.*, 2011; *Roda et al.*, 2011), a systematic analysis of the effect of thermal state of the overriding plate state has not been performed before this thesis. In the present study we develop 2D and 3D numerical thermo-mechanical modeling of subduction processes to test this effect. Overriding plate thermal state will be varied from a model to another in 2D models. We will also explore the influence of lateral variations in the trench-perpendicular direction in 2D models, and in trench-parallel directions in 3D models.

1.2. Objectives

The main objective of this thesis is to obtain a better understanding of the dynamics of subduction, and to explore different factors that might play an important role in controlling the geometry of the slab and associated mantle flow. To do so, we will try to fulfill four specific objectives.

First, in Chapter 3 we will develop simple 2D numerical models using the commercial software Comsol Multiphysics. With these kinematically-driven models we will test the influence of the thermal state of the overriding and subducting plates on the geometry of the slab. Variations on the thermal state of the subducting plate produce variations of the gravitational torque, whereas variations of the thermal state of the overriding plate will change the hydrodynamic suction in the mantle wedge. We will aim to study how the competition between gravitational and suction torques determines the resulting slab dip.

Second, in Chapter 4, also using 2D models and Comsol Multiphysics, we will test how the slab geometry is affected by a relative mantle flow. The relative motion of the mantle and the subducting plate can modify the slab dip depending on whether it opposes or accompanies the motion of the subducting plate.

Third, in Chapter 5, we will develop more realistic 3D dynamically-driven models with a more complex rheology using the open source code CitcomS. First we will try to generalize results from Chapter 3 and test the effect of the thermal state of the overriding plate in a 3D geometry with lateral (along trench) variations. We will study if slab dip variations can be maintained or even generated when there is an increased suction only in a particular region of the model. Second, we will study the effect of lateral variations of the thermal state of the overriding plate on mantle flow pattern, paying special attention to the appearance of trench-parallel flow. Finally, we will study how slab geometry and trench-parallel flow are modified when the material can flow around the edges of the slab.

Finally, through all the chapters, we will compare the results obtained in the models with natural examples. We will try to explain slab dip variations found in some subduction zones (e.g., Central and South America) in terms of the studied factors.

2

METHODOLOGY

2.1. Basic Equations

There are three main mechanisms in which Earth materials can be deformed (Figure 2.1): elastic, viscous and plastic. Elasticity can be described in a simplified way by the behavior of a spring: the deformation is proportional to the applied stress and returns to its original shape when the stress ceases acting. Viscous deformation can be represented by a dashpot: the rate of deformation is related to the applied stress, and the deformation is not recovered once the stress ceases. The third basic mechanism is plasticity, which states that rocks have a finite strength and they will fail or yield if applied stresses are larger than a given value, the so called yield-stress.

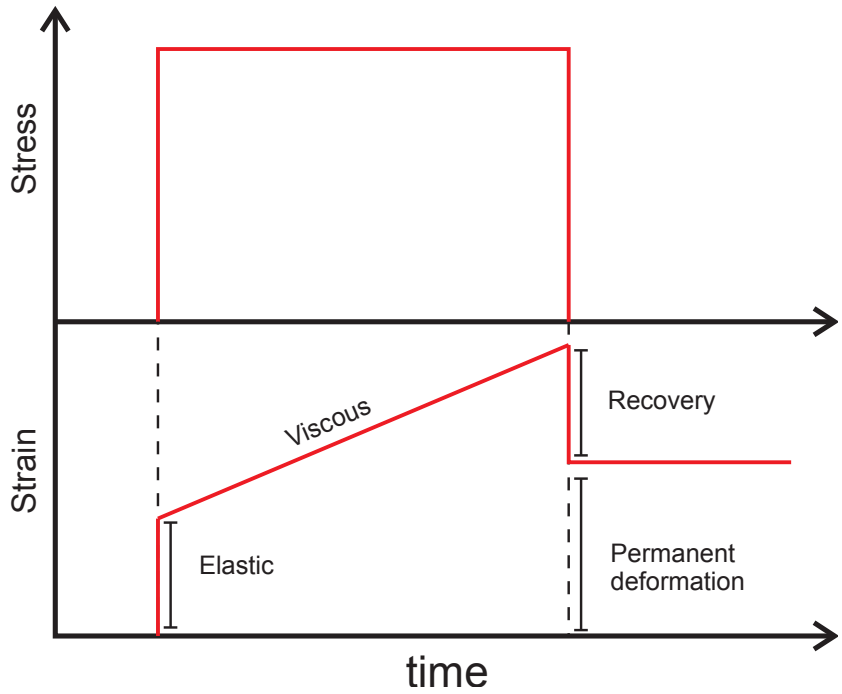

Figure 2.1: Diagram of the strain caused by a constant stress applied during finite period of time. The elastic deformation is recovered after stress removal, and a permanent viscous deformation remains.

Most of the solid materials of the Earth have an elastic behavior at low temperatures and low pressures when the applied stresses are not too large. At high stress levels or high temperatures and pressures rocks deform viscously. At last, for even higher stresses and low temperatures, materials behave in a plastic way and the rocks fracture losing its continuity.

In geodynamics the elastic approach is used to describe many processes, such as the propagation of seismic waves, isostatic adjustment or postglacial rebound. In most cases, long-term subduction dynamics is modeled using the viscous approximation, that is, over long times (greater than approximately one million years) the elastic response of the lithosphere and mantle can be ignored and only the viscous behavior is considered. Visco-elastic behavior (Figure 2.1) combines both viscous and elastic deformation and can be represented by mechanical analogs with different combinations of springs and dashpots. The Maxwell visco-elastic model is represented by a spring and a dashpot connected in series, and is the simplest way to combine both the elastic behavior of the lithosphere on relatively short timescales (e.g. postglacial rebound) and viscous creeping deformation at longer timescale.

In subduction dynamics, a visco-elastic approach is used to study the influence of the slab bending on the overlying topography (e.g., *Melosh and Rafesky*, 1980; *Gurnis et al.*, 1996) or when focusing the study on the dynamics of subduction initiation (e.g., *Toth and Gurnis*, 1998; *Regenauer-Lieb et al.*, 2001; *Hall et al.*, 2003). In contrast, we focus on the dynamics and deformation of the deeper portion of the slab and therefore, elasticity is not included in this modeling. Moreover, previous models (*Billen and Hirth*, 2007; *Faccenda et al.*, 2009) have shown that the slab yields throughout its thickness as it enters the trench: once the material has yielded, it no longer has any elastic strength. In two-dimensional models (Chapter 3) a maximum viscosity cutoff is included to limit the strength of the plates at the surface, whereas in three-dimensional models (Chapter 4) we also include a pseudo-plastic mechanism in the uppermost region of the plates, which leads to a reduced viscosity for high stresses (see section 2.1.4 for more details about how pseudo-plastic viscosity is implemented). Therefore a viscous approach is appropriate to address the study of the dynamics of subduction at least for mantle scale subduction processes (*Schmeling et al.*, 2007). In order to do this and study dynamics of the plates and mantle as very dense and very viscous fluids it is necessary to solve the coupled equations of conservation of mass, momentum and energy. In the following sections I give an overview of how these equations are obtained, how these equations are coupled through the viscosity and the density, and which approximations are assumed to simplify the numerical model.

2.1.1 Conservation of mass.

Conservation of mass requires that the change of mass with time inside an elemental volume is equal to the net flow of mass into or out of the volume. This is:

$$\frac{\partial \rho}{\partial t} + \frac{\partial}{\partial x_i}(\rho u_i) = 0 \tag{2.1}$$

where i stands for the spatial coordinate (with i=1,2 for horizontal directions and i=3 for vertical), x_i is the position vector, t is time, ρ is the density and u_i is the fluid velocity. In this notation if two subscripts are repeated, the summation over the three coordinates is assumed.

In fluid dynamics it is common to use the total o material derivative, the time derivative following an element of fluid in motion, and is defined as:

$$\frac{D}{Dt} = \frac{\partial}{\partial t} + u_i \frac{\partial}{\partial x_i} \tag{2.2}$$

Using the definition of the total derivative, equation (2.1) can be rewritten as:

$$\frac{D\rho}{Dt} + \rho \frac{\partial u_i}{\partial x_i} = 0 \tag{2.3}$$

2.1.2 Conservation of momentum

In order to study fluid's motion, we should start from Newton's second's law[1]:

$$\sum_k F_k = \frac{D(mu)}{Dt} \tag{2.4}$$

We can separate all the forces in two groups: internal and external forces. Internal forces cause the fluid to deform, and are calculated as the spatial

1 Note that instead of the usual d/dt we have used the total derivative D/Dt as we are dealing with a moving fluid.

variation of the stress tensor. Therefore, Newton's second law for a fluid can be rewritten as:

$$\frac{\partial \sigma_{ij}}{\partial x_j} + f_i = \frac{D(\rho u_i)}{Dt} \tag{2.5}$$

where σ is the stress tensor and f are all the external forces per unit volume.

The only external force we consider is the gravitational force, acting only in the vertical direction. Therefore f would be the weight per unit volume exerted over a fluid element, and has the same direction as the gravity acceleration.

$$f_i = \rho g \delta_{i3} \tag{2.6}$$

where δ_{ij} is the Kronecker's delta, defined as 1 if i=j and 0 if i≠j.

Combining equations (2.5) and (2.6):

$$\frac{\partial \sigma_{ij}}{\partial x_j} + \rho g \delta_{i3} = u_i \frac{D\rho}{Dt} + \rho \frac{Du_i}{Dt} \tag{2.7}$$

The term containing the internal forces is responsible for the deformation of the fluid. In order to completely describe the stresses acting at a point in a viscous medium, we must consider the stresses acting on the infinitesimally small cube of fluid (Figure 2.2). The component σ_{ij} acting perpendicular to each of the faces contributes to compress or dilate the fluid and the components acting parallel to each surface contribute to shear it. The stress tensor σ can be separated into two contributions.

$$\sigma_{ij} = -P\delta_{ij} + \tau_{ij} \tag{2.8}$$

where the first term represents the isotropic stress, given by the pressure P and the second term corresponds to the deviatoric stress[2] τ. Using this equation together with eq. (2.7) we obtain:

$$-\frac{\partial P}{\partial x_i} + \frac{\partial \tau_{ij}}{\partial x_j} + \rho g \delta_{i3} = u_i \frac{D\rho}{Dt} + \rho \frac{Du_i}{Dt} \tag{2.9}$$

[2] Here the tensile stress is considered to be negative.

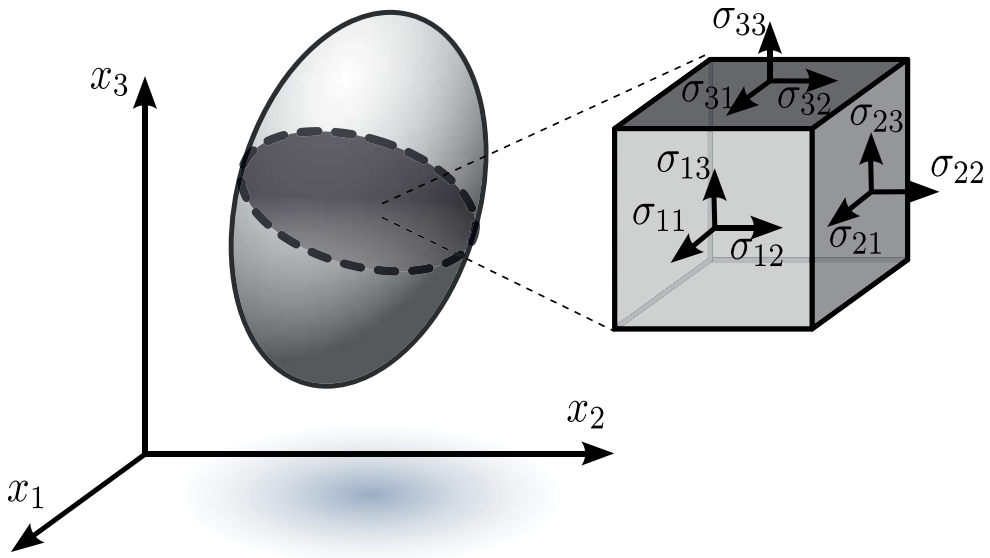

Figure 2.2: Stress in a loaded deformable material body assumed as a continuum.

We further develop equation (2.9) to obtain the relationship between driving forces and the deformation of the fluid. We do so using the *constitutive law* that relates the deviatoric stress to strain rate as follows:

$$\tau_{ij} = C_{ijkl}\dot{\varepsilon}_{kl} \tag{2.10}$$

where $\dot{\varepsilon}_{ij}$ is the strain rate tensor, which measures the velocity at which the fluid deforms.

$$\dot{\varepsilon}_{ij} = \frac{1}{2}\left(\frac{\partial u_i}{\partial x_j} + \frac{\partial u_j}{\partial x_i}\right) \tag{2.11}$$

The trace of the strain rate tensor relates to the changes in volume of the fluid (dilatation or compression) whereas the non-diagonal elements are related to the shear deformation. The tensor C_{ijkl} is a fourth order consisting of 81 elements but can be simplified if we consider that forces are conservative and if we apply symmetry and isotropy assumptions. In this case the 81 elements are reduced to two elements and the constitutive law is:

$$\tau_{ij} = \lambda\dot{\varepsilon}_{ij}\delta_{ij} + 2\eta\dot{\varepsilon}_{ij} \tag{2.12}$$

where η is the *dynamic viscosity* and λ is the *second viscosity*. The average of the normal deviatoric stresses on three mutually perpendicular planes at a point in the fluid is $\tau_{ii}/3$, and from (2.12) we have:

$$\frac{\tau_{ii}}{3} = \dot{\varepsilon}_{ii}\left(\lambda + \frac{2}{3}\eta\right) \equiv k_B \dot{\varepsilon}_{ii} \tag{2.13}$$

where k_{ii} is the bulk viscosity, a measure of the dissipation under compression or expansion. Combining equations (2.12) and (2.13) we have:

$$\tau_{ij} = 2\eta\dot{\varepsilon}_{ij} + \left(k_B - \frac{2}{3}\eta\right)\dot{\varepsilon}_{kk}\delta_{ij} \tag{2.14}$$

For many fluids k_{ii} is very small and is often taken to be zero, an assumption known as the *Stokes assumption*[3]. I that case, and combining equations (2.9), (2.11) and (2.14) we obtain Navier-Stokes equation in terms of the relationship between pressure gradient and gravity and the deformation of the fluid:

$$\frac{\partial}{\partial x_j}\left[\eta\left(\frac{\partial u_i}{\partial x_j} + \frac{\partial u_j}{\partial x_i} - \frac{2}{3}\frac{\partial u_k}{\partial x_k}\delta_{ij}\right)\right] - \frac{\partial P}{\partial x_i} + \rho g \delta_{i3} = u_i \frac{D\rho}{Dt} + \rho \frac{Du_i}{Dt} \tag{2.15}$$

This general form of the Navier-Stokes equation represents a balance between inertial forces (right-hand side of the equation) and viscous forces, pressure forces and body force due to gravity. This equation can be further simplified in order to reduce the computational cost of the simulations and these simplifications are explained in section 2.1.5.

2.1.3 Conservation of energy.

One of the most important features that need to be addressed when studying the Earth using the viscous approximation is the heat transfer. To do so we must start form the second law of thermodynamics:

$$dq = Tds \tag{2.16}$$

[3] The Stokes assumption states that in a Newtonian -Stokesian fluid, the average of the total normal stresses on three mutually perpendicular planes at a point in the fluid equals the negative of the hydrostatic pressure.

where q stands for the heat, T is the absolute temperature and s is the entropy.

Applying equation (2.16) to an elemental parcel of fluid with density ρ and taking into account all possible heat sources, we can derive an equation for the conservation of:

$$\rho T \frac{Ds}{Dt} = \Phi - \frac{\partial q_i}{\partial x_i} + \rho H - Q_L \tag{2.17}$$

This equation relates the rate of change of the entropy of the system (left hand side of the equation) to the volumetric heat production rates per unit mass of the other heat sources (right hand side of the equation). These are, respectively, the viscous dissipation (or shear heating) Φ, the thermal conduction, the internal heat generation H due to radiogenic sources and the latent heat Q_L produced during phase transitions that may occur in the fluid.

The viscous dissipation is related to the stress as:

$$\Phi = \tau_{ij} \frac{\partial u_i}{\partial x_j} \tag{2.18}$$

The thermal conduction is calculated using *Fourier's law* of conduction for an isotropic medium:

$$q_i = -k \frac{\partial T}{\partial x_i} \tag{2.19}$$

where k is the thermal conductivity.

The left hand side of equation (2.17) can be developed in terms of the variations of the temperature and the pressure using:

$$ds = \left(\frac{\partial s}{\partial T} \right)_{p,\beta} dT + \left(\frac{\partial s}{\partial p} \right)_{T,\beta} dp \tag{2.20}$$

where β is the phase change fraction and the subscripts stand for the magnitude that remains constant. The partial derivatives appearing in this equation cam be written in terms of thermodynamic quantities using:

$$\left(\frac{\partial s}{\partial T}\right)_{p,\beta} = \frac{c_p}{T} \tag{2.21}$$

$$\left(\frac{\partial s}{\partial p}\right)_{T,\beta} = -\left(\frac{\partial v}{\partial T}\right)_{p,\beta} = -\frac{\alpha}{\rho} \tag{2.22}$$

where c_p is the specific heat at constant pressure, v is the volume and α is the thermal expansion coefficient. Therefore equation (2.20) is:

$$ds = \frac{c_p}{T} dT - \frac{\alpha}{\rho} dp \tag{2.23}$$

and the total derivative with time is:

$$\frac{Ds}{Dt} = \frac{c_p}{T}\frac{DT}{Dt} - \frac{\alpha}{\rho}\frac{Dp}{Dt} \tag{2.24}$$

Combining equations (2.17) and (2.24), we obtain:

$$\rho c_p \frac{DT}{Dt} - \alpha T \frac{Dp}{Dt} = \Phi - \frac{\partial q_i}{\partial x_i} + \rho H - Q_L \tag{2.25}$$

And finally, developing the total derivatives we obtain:

$$\rho c_p \left(\frac{\partial T}{\partial t} + v_i \frac{\partial T}{\partial x_i}\right) - \alpha T \left(\frac{\partial p}{\partial t} + v_i \frac{\partial p}{\partial x_i}\right) = \Phi - \frac{\partial q_i}{\partial x_i} + \rho H - Q_L \tag{2.26}$$

2.1.4 Thermo-Mechanical coupling: density and viscosity.

So far, equations (2.3), (2.15) and (2.26) share some variables and therefore should be solved together. For example, the velocity field obtained by solving the momentum equation (2.15) needs to be used explicitly on energy (or thermal) equation (2.26). For density and viscosity, the relationship between energy and momentum equation is not explicit, but both variables need to be included to solve equation (2.15) and both depend in turn on the temperature obtained by solving equation (2.26). Velocity, viscosity and density are known as *coupling variables* and their study is crucial to assess this problem of coupled equations.

The density is a thermodynamic variable whose value for each material depends on the pressure and the temperature. The equation that states this relationship is the *equation of state*. It can be written as a Taylor's expansion of ρ about the reference density ρ_0 (density at T_0 = 273 K and P_0 = 101325 Pa):

$$\rho(T,P) = \rho_0 \left[1 - \alpha \left(T - T_0\right) + \chi \left(P - P_0\right)\right] \tag{2.27}$$

where χ is the *adiabatic compressibility coefficient*. This equation can be expressed in a more complex way as, for example, the thermal expansion coefficient can be both pressure and temperature dependent. For the Earth there are also significant density variations due to phase changes (e.g., olivine-spinel and spinel-perovskite) and important changes in the mantle density due to variations in chemical compositions. Nevertheless, for simplicity, from now on we consider that the density is only temperature and pressure dependent and that the coefficients α and χ are constant.

For the simplest fluids the relationship between stress and strain rate can be considered linear and the viscosity only depends on the temperature and the pressure, but not on the strain rate. When this happens the viscosity is called *Newtonian* or *linear viscosity*. If on the other hand the relationship between stress and strain rate is non-linear, the constitutive law given by equation (2.12) is still valid if we consider that the viscosity also depends on the strain rate. In this case, the rheology is considered to be *Non-Newtonian* or *non-linear viscosity*. When the viscosity depends on the temperature, the pressure and the strain rate all together, solving the problem numerically and interpreting the results becomes more challenging.

Olivine is the dominant material in the upper mantle and its rheology has been studied in great detail (see *Karato and Wu*, 1993; *Hirth*, 2003; *Korenaga and Karato*, 2008 and references therein). There are two main mechanisms in which olivine can deform under the influence of an applied stress: *diffusion creep* and *dislocation creep*. Creep deformation occurs under an applied stress due to thermally activated motion of atoms and ions associated with crystalline defects, such as dislocations and atomic vacancies. Both mechanisms are strongly temperature and pressure dependent, which leads to great viscosity contrasts for the Earth ($\Delta\eta = 10^5$ □□ ·□).

In the diffusion creep mechanism vacancies (empty sites in the crystalline lattice) move through the lattice and the adjacent atoms migrate (Figure 2.3). To understand how a diffusion process works, we focus on the diffusion coefficient D of a solid crystal that gives the fraction of atoms that have sufficient energy to diffuse on the lattice:

$$D = D_0 \exp\left[-\frac{E^* + PV^*}{RT} \right] \tag{2.28}$$

where D_0 is the frequency factor, R is the universal gas constant, V^* is the activation volume and E^* is the total activation energy. The activation energy is related to the total energy that an atom needs to diffuse, i.e., the energy of formation of a vacancy plus the energy required for an atom to migrate from its current location to the generated empty vacancy. The term PV^* accounts for the effect of pressure, which reduces the number of vacancies and increases the energy barrier.

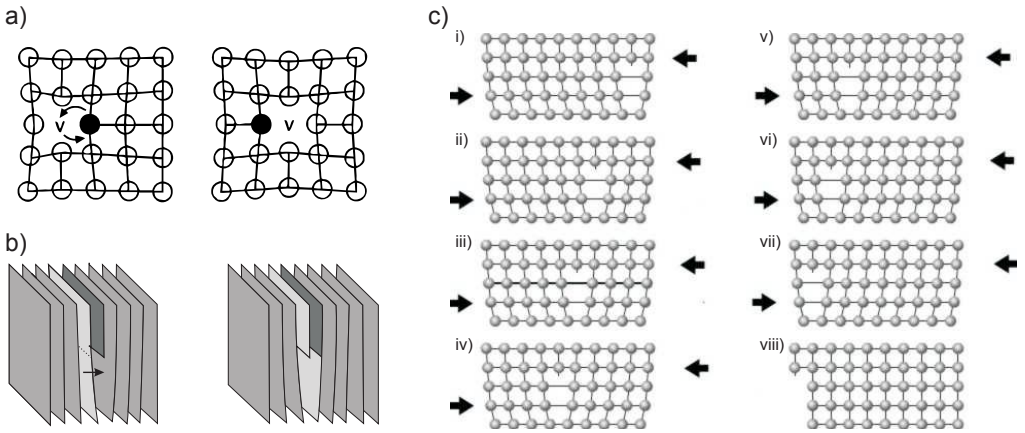

Figure 2.3: Deformation mechanisms. a) Motion of a vacancy from one lattice site to an adjacent one by the opposite motion of an atom in the diffusion creep mechanism (Modified from *Schubert et al.*, 2001). b) and c) dislocation sheet moving through the lattice in the deformation through the dislocation creep mechanism.

When a solid deforms through the dislocation mechanism a line of imperfection is created in the lattice (Figure 2.3 b and c). This line of imperfections is known as *dislocation* and it deforms the lattice as it migrates through the fluid.

The diffusion creep mechanism leads to a linear rheology, whereas the dislocation creep leads to a nonlinear rheology (strain rate dependent viscosity), but both can be expressed using the same power law (*Hirth and Kohlstedt*, 1996):

$$\eta_{df,ds} = \left(\frac{d^p}{AC_{OH}^r} \right)^{\frac{1}{n}} \dot{\varepsilon}_E^{\frac{1-n}{n}} \exp\left[\frac{E^* + PV^*}{nRT} \right] \tag{2.29}$$

where d is the grain size, p is the grain size exponent, A is the pre-exponential factor, C_{OH} is OH concentration, n is the stress exponent and $\dot{\varepsilon}_E = 1/2\, \dot{\varepsilon}_{ij} \dot{\varepsilon}_{ij}^{\,1/2}$ is the *effective strain rate*. Depending on whether the rheology is linear or nonlinear, the values of these rheological parameters vary (Table 3.1 and Table 5.2). When a linear material deforms through a diffusion mechanism, n=1 and the viscosity dependence on the strain rate is lost, whereas for a material that deforms through a dislocation mechanism, n>1 and the material is nonlinear. It is important to note that the power-law relationship between viscosity and strain rate for dislocation creep is responsible for strong decrease of viscosity in areas of high strain rate, resulting in viscosities one to three orders of magnitude lower than the background viscosity.

Another difference between these two mechanisms is that the diffusion creep viscosity strongly decreases with decreasing grain size (p=3), while dislocation creep is insensitive to changes in grain size (p=0).

There are other factors that can affect the viscosity, such as the water content, as rheological parameters differ if olivine is dry or wet. Also partial melting of the rocks can affect the rheology (*Hirth and Kohlstedt*, 1995a, 1995b; *Kohlstedt and Zimmerman*, 1996), as laboratory experiments show that 1-3% melt can reduce the viscosity by a factor of 2-5. Phase changes also affect the viscosity and for example, studies of the radial viscosity structure using geoid data, show that in the upper-lower mantle boundary the viscosity increases one to two orders of magnitude (e.g., *Hager and O'Connell*, 1981; *Hager and Richards*, 1989; *Forte and Mitrovica*, 2001; *Lee et al.*, 2011).

The three main sources to obtain data that allow constraining these rheological parameters are *postglacial rebound modeling*, the study of the geoid and laboratory measurements of rock deformation reproducing mantle conditions.

For example, postglacial rebound studies show that the mean viscosity for the upper mantle is around 10^{21} Pa·s (e.g., *Ranalli*, 1995; *Schubert et al.*, 2001). The studies of the viscosity based on the geoid focus on the radial viscosity structure of the Earth (e.g., *Hager and O'Connell*, 1981; *Hager and Richards*, 1989) and constrain the lower mantle viscosity to be less than 10^{22} Pa·s (*Steinberger*, 2000; *Yoshida*, 2004).

Laboratory experiments allow to obtain information about each parameter independently (*Hirth and Kohlstedt*, 2003; *Korenaga and Karato*, 2008) but this approach has serious difficulties. There are three main caveats to extrapolating experimentally determined flow laws to deformation in the upper mantle: temperature, pressure and strain-rate regimes are limited in the laboratory. In order to develop the experiments at a reasonable time scale, the measurements must be carried out at much higher temperature and strain rate than those associated with mantle processes. The mantle is assumed to convect at speeds similar to observed plate motion, which implies strain-rates on the order of $\dot{\varepsilon} = 10^{-15} s^{-1}$. Laboratory strain rates, e.g., 10^{-5} s^{-1}, must be extrapolated over several orders of magnitude to reach mantle conditions. Also, the experiments are carried out at much lower pressure. These limitations can be partially overcome combining laboratory experiments with other sources of information.

Moreover, olivine does not deform only through one mechanism. The materials deform in such a way that the mechanism that offers a lower resistance is the preferred one. Assuming a constant stress and that the total strain-rate is the sum of the strain-rate accommodated by both mechanisms ($\dot{\varepsilon} = \dot{\varepsilon}_{df} + \dot{\varepsilon}_{ds}$), this can be expressed through a composite rheology or viscosity:

$$\eta_{comp} = \frac{\eta_{df}\eta_{ds}}{\eta_{df} + \eta_{ds}} \tag{2.30}$$

The behavior of the materials in the lower mantle is different and the deformation is accommodated only through diffusion creep and the viscosity is considered to be relatively constant with a value around 10^{22} *Pa·s*. This modification can be thought of as varying the grain size or water concentration. We note that there are rather large uncertainties in the grain size and water

content at depths of the transition zone and below as there are no natural samples of these rocks.

As was mentioned before, viscous deformation is not the only mechanism in which the stress can be accommodated. For example, during a subduction process, the cold interior of the slab has a high viscosity compared with the surrounding mantle. For typical strain rate of 10^{-15} s^{-1}, the viscous force would exceed the strength of the rock and it would yield. Once the rock has yielded the deformation is accommodated in a brittle way and the viscosity upper bound does not depend on the viscous deformation but on the yield strength, which is estimated to be 300-1000 MPa (*Goetze and Evans*, 1979; *Evans et al.*, 1990). This is roughly equivalent to a mechanism in which the effective viscosity is:

$$\eta_{ef} = \min\left(\eta_{comp}, \frac{\sigma_y}{\dot{\varepsilon}_E}\right) \tag{2.31}$$

where σ_y is the yield strength, that can be uniform or depth dependent.

2.1.5 Simplified equations.

First of all, we assume that equations (2.3), (2.15), (2.26) and (2.27) are solved for the oceanic lithosphere. Provided that the radiogenic heating is only significant in continental crust, we drop the term containing the internal heating in equation (2.26). Also, from now on we neglect the contribution of the phase transitions to equation (2.26).

When applied to mantle convection, the previous equations can be simplified using different approximations. It is important to understand when each of these approximations can be applied and at what cost, to do so we study equations of conservation of mass (2.3), momentum (2.15), energy (2.26) and state (2.27) in their non-dimensional form (for a more detailed explanation of the non-dimensionalization procedure, refer to Schubert et al., 2001).

The non-dimensional variables used are:

$$\eta' = \frac{\eta}{\eta_r} \tag{2.32}$$

$$T' = \frac{T}{\Delta T_r} \tag{2.33}$$

$$\rho' = \frac{\rho}{\rho_r} \tag{2.34}$$

$$p' = p\frac{b^2 \rho_r c_P}{\eta_r k} \tag{2.35}$$

$$u'_i = u_i \frac{b\rho_r c_p}{k} \tag{2.36}$$

$$x'_i = \frac{x_i}{b} \tag{2.37}$$

$$t' = t\frac{k}{b^2 \rho_r c_p} \tag{2.38}$$

where b is the depth of the convective region, primed variables are the non-dimensional variables and the variables with subscripted r are the reference value of those variables, characteristic of each problem. Using these relationships the non-dimensional versions of equations (2.3), (2.15), (2.26) and (2.27) are respectively:

$$\rho'_0 M^2 \,\mathrm{Pr}\frac{\partial p'}{\partial t} - \rho_0 ' \in \frac{\partial T'}{\partial t} + \frac{\partial\ \rho' u'_i}{\partial x'_i} = 0 \tag{2.39}$$

$$\begin{aligned}\frac{\rho'}{\mathrm{Pr}}\frac{Du'_i}{Dt} &= -\frac{\partial p'}{\partial x'_i} + \rho'_0\, g\delta_{i3} + \rho'_0 \frac{Di}{\gamma_r}\frac{c_p}{c_v} P'\delta_{i3} - \rho'_0 T' Ra\delta_{i3} + \\ &+ \frac{\partial}{\partial x'_i}\left[\eta'\left(\frac{\partial u'_i}{\partial x'_j} + \frac{\partial u'_j}{\partial x'_i} - \frac{2}{3}\delta_{ij}\frac{\partial u'_k}{\partial x'_k}\right)\right]\end{aligned} \tag{2.40}$$

$$c_p \rho' \frac{DT'}{Dt} - T' \frac{\in Di}{Ra}\frac{\partial p'}{\partial t} - T' u'_i \rho'_0 Di = \frac{\partial}{\partial x'_i}\left(k\frac{\partial T'}{\partial x'_i}\right) + \Phi\frac{Di}{Ra} \tag{2.41}$$

$$\rho'(T,P) = \rho_0 '\ 1 - \in\ T' - T_0 '\ + M^2\,\mathrm{Pr}\ \ P' - P_0 ' \tag{2.42}$$

where some non-dimensional numbers have been introduced:

$$M^2 = \frac{k^2 \chi}{\rho_r c_p b^2} \tag{2.43}$$

The dimensionless parameter M^2 measures the influence of the compressibility and for the mantle its value is about 10^{-33}.

$$\mathrm{Pr} = \frac{\eta_r c_p}{k} \tag{2.44}$$

The parameter *Pr* is the *Prandtl number* and measures the ratio between the momentum diffusivity (or the viscosity) and the heat diffusivity (or the conductivity). The mantle is a very viscous medium, so the momentum diffusivity is high and Pr is about $2.5 \cdot 10^{23}$.

$$\in = \alpha \Delta T_r \tag{2.45}$$

This parameter is the density change of the mantle due to temperature variations that is responsible of most of the convection. Its value for the mantle is about $3 \cdot 10^{-2}$.

$$Di = \frac{\alpha g b}{c_p} \tag{2.46}$$

The d*issipation number Di* determines the importance of the density variations due to temperature changers against the viscous dissipation in thermal convection. For the Earth's mantle, its value is about 0.5.

$$\gamma_r = \frac{\alpha}{\rho_r c_v \chi} \tag{2.47}$$

The *Grüneisen parameter* γ_r is a measure of the effect of temperature on the vibrational properties of the fluid, and for the mantle is around 1.

$$Ra = \frac{\alpha \Delta T_r \rho_r^{\,2} g b^3 c_p}{\eta_r k} \tag{2.48}$$

The parameter *Ra* is the *Rayleigh number* and measures the two main mechanisms for heat transfer: convection and conduction. For the mantle, Ra is of the order of 10^9.

For the Earth, $M^2Pr<<1$ and $\in$ is also small, so all terms multiplied by these non-dimensional parameters can be dropped. In the limit $M^2\,\mathrm{Pr}\to 0$ and $\in\to 0$, equation (2.39) reduces to:

$$\frac{\partial\ \rho' u'_i}{\partial x'_i} = 0 \tag{2.49}$$

Also, for very viscous fluids, which is the case of the Earth where the viscosity varies from 10^{18} to 10^{25} Pa·s, Pr is very high. Therefore, the left hand side of equation (2.40) can be dropped, and we obtain:

$$\begin{aligned} 0 = &-\frac{\partial p'}{\partial x'_i} + \rho'_0\, g\delta_{i3} + \rho'_0\,\frac{Di}{\gamma_r}\frac{c_p}{c_v}P'\delta_{i3} - \rho'_0\,T'Ra\delta_{i3} + \\ &+\frac{\partial}{\partial x'_i}\left[\eta'\left(\frac{\partial u'_i}{\partial x'_j}+\frac{\partial u'_j}{\partial x'_i}-\frac{2}{3}\delta_{ij}\frac{\partial u'_k}{\partial x'_k}\right)\right] \end{aligned} \tag{2.50}$$

This means that inertial forces are considered to be small compared with the pressure, gravitational and stress related forces.

Also equation (2.41) is modified and the term corresponding to the temporal variation of the pressure is dropped:

$$c_p\rho'\frac{DT'}{Dt} - T'u'_i\,\rho'_0\,Di = \frac{\partial}{\partial x'_i}\left(k\frac{\partial T'}{\partial x'_i}\right) + \Phi\frac{Di}{Ra} \tag{2.51}$$

Equation (2.42) is also simplified, as the pressure dependence of the density can be neglected. The resulting equation is:

$$\rho'(T,P) = \rho_0'\ 1-\in\ T'-T_0' \tag{2.52}$$

The set of equations (2.49), (2.50), (2.51) and (2.52) is known as the *Liquid Anelastic Approximation* (ALA) and its dimensional form is:

$$\frac{\partial\ \rho u_i}{\partial x_i} = 0 \tag{2.53}$$

$$\frac{\partial}{\partial x_j}\left[\lambda \frac{\partial u_k}{\partial x_k}\delta_{ij} + \eta\left(\frac{\partial u_i}{\partial x_j} + \frac{\partial u_j}{\partial x_i}\right)\right] - \frac{\partial P}{\partial x_i} + \rho g \delta_{i3} = 0 \tag{2.54}$$

$$\rho c_p\left(\frac{\partial T}{\partial t} + v_i \frac{\partial T}{\partial x_i}\right) - \alpha T g v_3 \rho = \Phi - \frac{\partial q_i}{\partial x_i} \tag{2.55}$$

$$\rho(T,P) = \rho_0\ \ 1 - \alpha\ \ T - T_0 \tag{2.56}$$

we assume that the pressure is lithostatic and $\partial P/\partial x_i = \rho g \delta_{i3}$. The explicit dependence on time has disappeared, so the equations can be considered quasi-static, but stress and density might still be time dependent.

A further simplification is known as the *Extended Boussinesq Approximation (EBA; e.g. Schmeling, 1989)*. Here the density is considered uniform except for buoyancy implications. In the equation (2.49), this implies assuming that the fluid is incompressible. Compressibility of the materials in the lithosphere and mantle are very low, therefore, the following approximation can be made:

$$\frac{\partial u'_i}{\partial x'_i} = 0 \tag{2.57}$$

In equation (2.50) we assume the limit $\mathrm{Di}/\gamma_r \to 0$, and using equation (2.57) the stress term is simplified:

$$\tau_{ij} = \eta\left(\frac{\partial u_i}{\partial x_j} + \frac{\partial u_j}{\partial x_i}\right) \tag{2.58}$$

and therefore, equation (2.50) becomes:

$$0 = -\frac{\partial p'}{\partial x'_i} + \rho'_0\, g - \rho'_0\, T' Ra + \frac{\partial}{\partial x'_i}\left[\eta'\left(\frac{\partial u'_i}{\partial x'_j} + \frac{\partial u'_j}{\partial x'_i}\right)\right] \tag{2.59}$$

For equation (2.51) we still consider $\mathrm{Di} \neq 0$, but we neglect Di / Ra:

$$c_p \rho' \frac{DT'}{Dt} - T' u'_i \rho'_0 Di = \frac{\partial}{\partial x'_i}\left(k \frac{\partial T'}{\partial x'_i} \right) \tag{2.60}$$

Where we neglect shear heating. This assumption is based on the fact that heat released due to the deformation of the fluid (i.e., shear heating) is important mostly in the plate boundary, where a great amount of shearing is taking place. In this region, we impose a low viscosity channel to simulate the weakening produced by shear heating (see section 2.1.4 for more detailed explanation).

The dimensional form of the equations when assuming EBA is:

$$\frac{\partial u_i}{\partial x_i} = 0 \tag{2.61}$$

$$\frac{\partial}{\partial x_j}\left[\eta \left(\frac{\partial u_i}{\partial x_j} + \frac{\partial u_j}{\partial x_i} \right) \right] - \frac{\partial P}{\partial x_i} + \rho g \delta_{i3} = 0 \tag{2.62}$$

$$\rho c_p \left(\frac{\partial T}{\partial t} + v_i \frac{\partial T}{\partial x_i} \right) = k \frac{\partial}{\partial x_i}\left(\frac{\partial T}{\partial x_i} \right) + \rho \alpha g v_3 T \tag{2.63}$$

Where we have assumed that k is constant and we have used equation (2.56).

The EBA, i.e., equations (2.56), (2.61), (2.62) and (2.63) were used for models explained in Chapters 3 and 4, so it is interesting to take a careful look at these equations term by term.

Equation (2.61) is the equation of conservation of mass for an incompressible fluid, for which the divergence of the velocity is zero.

Equation (2.62) is the equation of conservation of momentum or *Navier-Stokes Equation*. The firs term corresponds to the viscous forces and is intimately related to the deformation and the viscosity. The second term corresponds to the pressure gradient related force. And the third and final term corresponds to the gravitational force, which is considered to act only in the vertical direction and depends on the density.

Equation (2.63) is the equation of conservation of energy. The second term in the left hand side of the equation corresponds to the heat transfer due to

advection, whereas the first term on the right hand side is the heat transfer due to conduction. The second term on the right hand side of the equation is the heat released (or absorbed) when a parcel or fluid goes down (or up) due to the changes of pressure. This last contribution is also known as the *adiabatic heating*.

The simplest form of the equations is known as the *Boussinesq Approximation* (BA) where also effect of pressure in equation (2.63), this is, the adiabatic heating, is neglected. Therefore, the term containing the dissipation number (*Di*) in equation (2.60) is dropped.

$$c_p \rho' \frac{DT'}{Dt} = \frac{\partial}{\partial x'_i}\left(k \frac{\partial T'}{\partial x'_i} \right) \tag{2.64}$$

and in its dimensional form:

$$\left(\frac{\partial T}{\partial t} + v_i \frac{\partial T}{\partial x_i} \right) = \kappa \frac{\partial}{\partial x_i}\left(\frac{\partial T}{\partial x_i} \right) \tag{2.65}$$

Applying the BA implies neglecting the variations of any thermodynamic variable, including the density. Only density variations affecting the buoyancy of the fluid are taken into account, i.e., when density is coupled to the gravity acceleration (*Boussinesq*, 1903; *Spiegel and Veronis*, 1960; *Ita and King*, 1994).

The BA, i.e., equations (2.56), (2.61), (2.62) and (2.65) are used for models explained in Chapter 5.

2.2 Numerical methods

There are two steps that need to be taken in order to solve the Partial Differential Equations (PDEs) presented in the previous section using the Finite Elements Method (FEM).

- First it is necessary to use Finite Element Analysis to transform the PDE into a system of simple linear equations that allows us to represent the problem as:

$$\mathbf{A}\mathbf{u} = \mathbf{b} \tag{2.66}$$

where **u** contains the values of the variables we need to know (i.e., the three components of the velocity, the pressure and the temperature). How this is accomplished is explained in section 2.2.1.

- Second we need to solve equation (2.66) to obtain **u**. Solving an equation system like this can be really challenging provided the size and the complexity of the problem. Therefore, great effort has been invested to develop different methods to solve equation (2.66) in an efficient way. Numerous different methods are available and choosing the one that best suits the problem requires some knowledge about how each of the problems is implemented. A brief explanation of how the used methods work is developed in sections 2.2.

2.2.1 Finite Element Methods

The partial differential equations presented in the previous chapters have been solved using several *Finite Elements Methods* (FEM's). FEM's are a good approach to solve the equations of conservation of mass, momentum and energy, but the same problem can be addressed using a *Finite Difference Method* (FDM) (*Gerya*, 2009). We choose FEM as it is more suitable for complex geometries or problems that require local mesh refinement.

While the FDM consists in finding a discrete approximation of the PDE, the FEM approximates the solution of the PDE. The FEM consists on dividing a continuum object in a discrete assemble of finite elements. This way, complicated objects are divided in geometrically simple pieces. The points at which the elements are connected or assembled are called *nodes*, and the compound of elements and nodes is the *mesh*. The number of degrees of freedom is directly related to the number of nodes and depends on the PDE´s to be solved. When solving equations of conservation of momentum and energy in three dimensions, there are 5 degrees of freedom per node (the three components of the velocity, the pressure and the temperature).

The FE analysis consists of two steps:

- Convert the PDE from its original (strong) form to its integral (weak) form.

- Discretize the domain into elements on which an approximate solution of **u** is obtained as a sum of polynomial functions or shape functions.

A brief explanation of the way to proceed when applying the FEM is given on the following sections. For a more detailed explanation reader is referred to Hughes (2000).

2.1.1.1. Weak form of the PDE

In order to explain how to obtain the weak form of a PDE we will focus on a simple example and we start with the stationary heat conduction equation in 1D solved in the interval [0,1]:

$$\partial_x q_x = H \tag{2.67}$$

where H are internal heating sources and q_i the heat flow, defined as:

$$q_x = -\kappa \partial_x T \tag{2.68}$$

where κ [4] is the thermal conductivity. Therefore:

$$-\kappa \partial_{xx} T = H \tag{2.69}$$

Boundary conditions can be of two different kinds: Dirichlet or Neumann boundary conditions. The first kind fixes a certain value for the temperature and the second establishes a fixed value for its derivative. In order to understand how to deal with both types of boundary conditions is useful to use each one of them at each of the boundaries:

$$T(0) = T_0 \tag{2.70}$$

$$-\kappa \partial_x T(1) = q_x(1) = q_1 \tag{2.71}$$

It is important to notice that, provided that the Dirichlet boundary condition fixes the value of the solution at a certain point the number of degrees of freedom is reduced by one. On the other hand, we still need to find the solution at the boundary where the Neumann boundary condition is specified.

[4] Usually the symbol k is used for the thermal conductivity, but only during this section we will use κ to avoid confusion with the summation index used from equation (2.81)

To obtain the weak form of the PDE we need to define a set of functions w called *weighting functions* that satisfy the condition of being zero at the point where a Dirichlet boundary condition is imposed. In this particular case $w(0)=0$. Now, multiplying equation (2.69) from the left and integrating on the whole domain, we obtain:

$$-\int_0^1 w\kappa\partial_{xx}T dx = \int_0^1 wH dx \tag{2.72}$$

Now, integrating by parts we obtain:

$$-\left[w\kappa\partial_x T \Big|_0^1 - \int_0^1 \partial_x w\kappa\partial_x T dx \right] = \int_0^1 wH dx \tag{2.73}$$

And now, using equations (2.70) and (2.71) we have:

$$\int_0^1 \partial_x w\kappa\partial_x T dx = \int_0^1 wH dx - w(1)q_1 \tag{2.74}$$

This is the weak form of equation (2.69) and is valid for any internal heating source, not necessarily uniform. For simplicity it is useful to define the operator

$$\langle a, b \rangle = \int_0^1 a \cdot b dx \tag{2.75}$$

and equation (2.74) is now:

$$\langle \partial_x w, \kappa\partial_x T \rangle = \langle w, H \rangle - w(1)q_1 \tag{2.76}$$

A common approach to obtain the approximate solution to PDE problems based upon weak formulations is the *Galerkin Method,* which is explained here. First, T^h and w^h are the approximations of T and w, and satisfy the same boundary conditions. Now we define:

$$T^h = \tau^h + \tau_0^h \tag{2.77}$$

where

$$\tau^h(0) = 0 \tag{2.78}$$

$$\tau_0^h(0) = T_0 \tag{2.79}$$

Decomposing T^h this way, τ_0^h describes the behavior of the function at the boundary where the Dirichlet boundary condition has been imposed and we can focus on solving τ^h, which describes the temperature in the rest of the domain. If we had imposed a Dirichlet boundary condition on both sides, we would have defined two different functions τ_0^h and τ_1^h.

Now, writing equation (2.76) in terms of T^h and w^h and using equation (2.77) we obtain:

$$\partial_x w^h, \kappa \partial_x \tau^h = w^h, H - w^h(1) q_1 - \partial_x w^h, \kappa \partial_x \tau_0^h \tag{2.80}$$

2.1.1.2. Discretization

Once we have obtained equation (2.80) through the Galerkin method we can start the discretization process. First we divide the domain in *n* elements obtaining *n+1* nodes. Now that the domain is divided in elements, the next step is to describe the behavior of the physical quantities involved in the PDE on each of those elements. In this case, the temperature is described through a set of simple functions (usually polynomials) known as *shape functions*. Using these shape functions φ_k we can redefine w^h, τ_0^h and τ^h as:

$$w^h = \sum_{k=1}^{n} c_k \varphi_k \tag{2.81}$$

$$\tau^h = \sum_{k=1}^{n} t_k \varphi_k \tag{2.82}$$

$$\tau_0^h = T_0 \varphi_0 \tag{2.83}$$

If each shape function satisfies:

$$\varphi_k(x) = \begin{cases} 0 & for \quad k \neq 0 \\ 1 & for \quad k = 0 \end{cases} \tag{2.84}$$

automatically the boundary condition (2.70) is satisfied and we now need to know the values of t_k in order to describe *T*. Note that we only need to know n different t_k as we already know the value of the function at the *0th* node, determined by the first boundary condition. Note also that no condition has been imposed for the *nth* node and we need to find the value of t_n. Therefore, if we had

imposed a Dirichlet boundary condition at both nodes, we would have had to find n-1 different t_k and if we had imposed a Neumann boundary condition at both nodes we would have had to find n+1 different t_k.

Usually the shape functions are piecewise functions that are different from zero only at the elements *k* and *k+1*. Also, these functions are one for the *kth* node and zero in the rest. The most simple shape function is a linear function in the form:

$$\varphi_k(x) = \begin{cases} \dfrac{x - x_{k-1}}{h_{k-1}}, & x_{k-1} \le x \le x_k \\ \dfrac{x_{k+1} - x}{h_k}, & x_k \le x \le x_{k+1} \\ 0 \quad , & \text{elsewhere} \end{cases} \tag{2.85}$$

where x_k is the position of the *kth* node and h_k is the width of the *kth* element.

To obtain a better accuracy one option is to increase the number of elements by refining the mesh, but another option is to increase the order of the polynomial function used to define *T* inside each element. If we use a quadratic function, in order to characterize the polynomial we need to introduce new nodes inside each element. This increases the number of degrees of freedom, and we must also introduce new unknowns t_k. The two kind of elements described here are the two different elements we have used in this study and are known as *Lagrange Elements* of orders one and two or *linear* and *quadratic Lagrange Elements*.

Going back to equation (2.80), now we can combine it with equations (2.81), (2.82) and (2.83) to obtain:

$$\left(\sum_{k=1}^{n} c_k \partial_x \varphi_k, \kappa \sum_{l=1}^{n} t_l \partial_x \varphi_l\right) = \left(\sum_{k=1}^{n} c_k \varphi_k, H\right) - \left[\sum_{k=1}^{n} c_k \varphi_k(1)\right] q_1 - \left(\sum_{k=1}^{n} c_k \partial_x \varphi_k, \kappa T_0 \partial_x \varphi_0\right) \tag{2.86}$$

or

$$\sum_{k=1}^{n} c_k \left[\left(\partial_x \varphi_k, \kappa \sum_{l=1}^{n} t_l \partial_x \varphi_l\right) - \varphi_k, H + \varphi_k(1) q_1 + \partial_x \varphi_k, \kappa T_0 \partial_x \varphi_0\right] = 0 \tag{2.87}$$

These equations have to be fulfilled for any value of c_k as their values are arbitrary. This is equivalent to say that:

$$\sum_{l=1}^{n} \left\langle \partial_x \varphi_k , \kappa \partial_x \varphi_l \right\rangle t_l = \left\langle \varphi_k , H \right\rangle - \varphi_k(1) q_l - \left\langle \partial_x \varphi_k , \kappa \partial_x \varphi_0 \right\rangle T_0 \tag{2.88}$$

We can now define the matrices and vectors:

$$\mathbf{K} = \left[\left\langle \partial_x \varphi_k , \kappa \partial_x \varphi_l \right\rangle \right]_{nxn} \tag{2.89}$$

$$\mathbf{t}_l = \left[t_l \right]_{nx1} \tag{2.90}$$

$$\mathbf{F} = \left[\left\langle \varphi_k , H \right\rangle - \varphi_k(1) q_1 - \left\langle \partial_x \varphi_k , \kappa \partial_x \varphi_0 \right\rangle T_0 \right]_{nx1} \tag{2.91}$$

where **K** is often referred as the *stiffness matrix*, **t** as the *solution* or *displacement vector* and **F** as the *force vector*.

And finally we can reduce the PDE to a linear system in the form:

$$\mathbf{Kt} = \mathbf{F} \tag{2.92}$$

equivalent to equation (2.66) for which the only unknowns are the n elements of vector **t**. The stiffness matrix is both symmetrical and sparse (most of its elements are zero) due to the choice of the shape functions. These two properties have many advantages when solving equation (2.92) numerically.

2.1.1.3. Heat conduction in 1D in a three element mesh.

In order to better understand how the FEM works we will dedicate some time to explicitly solving a simple example. Continuing with the previous example of the conduction equation, we will study the particular case of a constant and uniform internal heating, thermal conductivity and boundary conditions:

$$H = 3 \; W \cdot m^{-3} \tag{2.93}$$

$$\kappa = 1 \; W \cdot m^{-1} \cdot K^{-1} \tag{2.94}$$

$$T(0) = 1 \; K \tag{2.95}$$

$$q(1) = 1 \; W \cdot m^{-2} \tag{2.96}$$

Before facing the problem of finding the discretized form of equation (2.67) we determine its analytical (exact) solution for these conditions. By integration and applying the boundary conditions:

$$T\ x\ = -\frac{3}{2}x^2 + 2x + 1 \tag{2.97}$$

Now we generate the simple mesh consisting of three elements (and therefore 4 nodes) of the same length (1/3). Assuming this, and using linear Lagrange elements as in equation (2.85) we have:

$$\varphi_0(x) = \begin{cases} 1-3x, & 0 \le x \le \frac{1}{3} \\ 0 \quad , & \text{elsewhere} \end{cases}$$

$$\varphi_1(x) = \begin{cases} 3x \quad , & 0 \le x \le \frac{1}{3} \\ 2-3x, & \frac{1}{3} \le x \le \frac{2}{3} \\ 0 \quad , & \text{elsewhere} \end{cases} \tag{2.98}$$

$$\varphi_2(x) = \begin{cases} 3x-1, & \frac{1}{3} \le x \le \frac{2}{3} \\ 3-3x, & \frac{2}{3} \le x \le 1 \\ 0 \quad , & \text{elsewhere} \end{cases}$$

$$\varphi_3(x) = \begin{cases} 3x-2, & \frac{2}{3} \le x \le 1 \\ 0 \quad , & \text{elsewhere} \end{cases}$$

Note how all these shape functions fulfill the condition we imposed at first: all of them (except φ_0) are zero at the node where the boundary condition is imposed, all have non-zero values only for the *kth* and the *k+1th* elements and are one at the *kth* node and zero at the rest (Figure 2.4.a).

2.1.1.4. Discretization in two and three dimensions

There are a few differences when using the FEM in two and three dimensions, and a few definitions should be clarified. First let x_i be the *ith* spatial

component and ∂_i the derivative with respect to the *ith* spatial component. W now consider the anisotropic conductivity $\kappa = [\kappa_{ij}]$, the heat flow is:

$$q_i = -\kappa_{ij}\partial_j T \tag{2.99}$$

and the heat conduction equation:

$$-\partial_i \kappa_{ij} \partial_j T = H \tag{2.100}$$

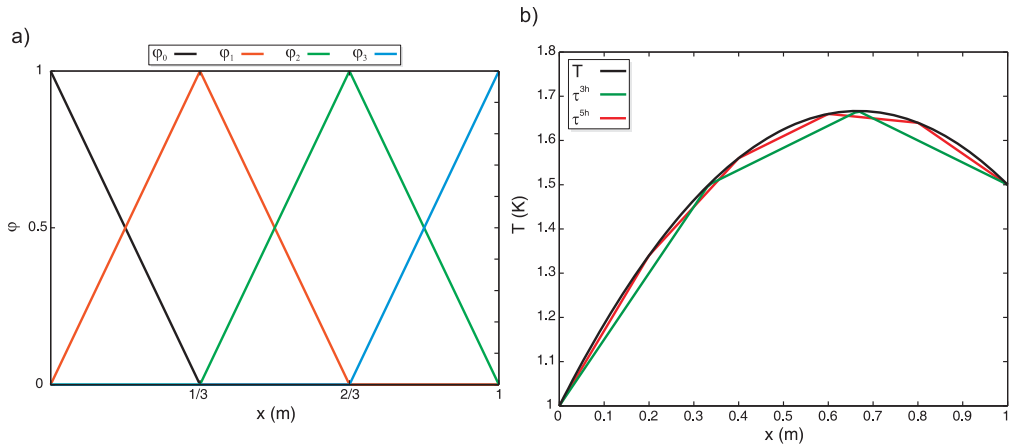

Figure 2.4: A simple example of the FEM in 1D. a) Galerkin shape functions for a mesh consisting of three elements. b) Exact and approximate solutions of a heat conduction problem obtained using finite element analysis.

Now the domain for which we want to solve the conduction is Ω and its boundary is $\partial\Omega$. We can also divide de boundary in two groups: those regions that satisfy a Dirichlet boundary condition $(\partial\Omega_D)$ and those that satisfy a Neumann boundary condition $(\partial\Omega_N)$:

$$T = T_0 \qquad \text{on } \partial\Omega_D \tag{2.101}$$

$$\partial_i w^h, \kappa_{ij}\partial_j \tau^h = w^h, H - w^h, H_{\partial\Omega} - \partial_i w^h, \tau_0^h \tag{2.102}$$

where n_i is the vector normal to $\partial\Omega$.

Finally, before obtaining the weak form of equation (2.100) the integration by parts is now defined as:

$$\int_\Omega \partial_i f \cdot g \cdot d\Omega = \int_{\partial\Omega} f \cdot g \cdot n_i \cdot d\partial\Omega - \int_\Omega f \cdot \partial_i g \cdot d\Omega \tag{2.103}$$

Taking all this into account, the weak form of the equation is:

$$(\partial_i w, \kappa_{ij} \partial_j T) = (w, H) - (w, q_1)_{\partial\Omega} \tag{2.104}$$

where:

$$(a,b) = \int_{\Omega} a \cdot b d\Omega \tag{2.105}$$

$$(a,b)_{\partial\Omega} = \int_{\partial\Omega} a \cdot b d\partial\Omega \tag{2.106}$$

As before we use the Galerkin formulation and define the approximate solution T^h as in (2.77) but now:

$$\tau^h = 0 \quad \text{in } \partial\Omega_D \tag{2.107}$$

$$\tau_0^h = T_0 \quad \text{in } \partial\Omega_D \tag{2.108}$$

This leads to:

$$\partial_i w^h, \kappa_{ij} \partial_j \tau^h = w^h, H - w^h, H_{\partial\Omega} - \partial_i w^h, \tau_0^h \tag{2.109}$$

where repeated index summation convention is applied for the coordinated indices *i* and *j*.

As before we define a set of shape functions that we use to rewrite w^h, τ^h and τ_0^h. In this case the shape functions $\varphi_k(\mathbf{x})$ depend on the two (or three) coordinates and have non-zero values only for their neighboring elements (Figure 2.5). As before, to build w^h and τ^h we need as many shape functions as degrees of freedom, i.e., the total number of nodes minus the number of nodes with a Dirichlet boundary condition. Equally, to build τ_0^h we need as many shape functions as nodes have a Dirichlet boundary condition. If η are all the nodes and η_D the nodes with a Dirichlet boundary condition we have:

$$w^h(\mathbf{x}) = \sum_{k \in \eta - \eta_D} \varphi_k(\mathbf{x}) c_k \tag{2.110}$$

$$\tau^h(\mathbf{x}) = \sum_{k \in \eta - \eta_D} \varphi_k(\mathbf{x}) t_k \tag{2.111}$$

$$\tau_0^h(\mathbf{x}) = \sum_{k\in\eta_D} \varphi_k(\mathbf{x}) T_{0\,k} \qquad T_{0\,k} = T_0(\mathbf{x}_k) \tag{2.112}$$

where **x** is the space coordinate in two (or three dimensions) and $\mathbf{x_k}$ is the position of the *kth* node. Now, for each node *k* in $\eta - \eta_D$ we can write:

$$\sum_{l\in\eta-\eta_D} \partial_i\varphi_k, \kappa_{ij}\partial_j\varphi_l \;\; t_l = \; \varphi_K, H \; - \; \varphi_K, q_1 \;_{\partial\Omega} - \sum_{l\in\eta_D} \partial_i\varphi_k, \kappa_{ij}\partial_j\varphi_l \;\; T_{0\,l} \tag{2.113}$$

where again the repeated index summation convention is applied for the coordinated indices *i* and *j*.

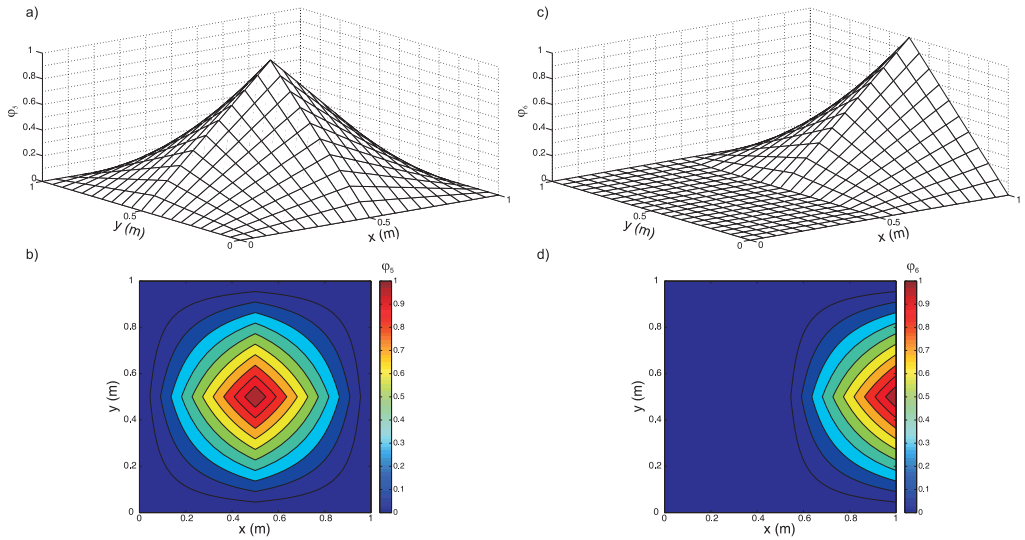

Figure 2.5: Galerkin shape functions for a 2D problem with a 2 by 2 elements mesh for φ_5 (a and b) and φ_6 (c and d).

Finally, we can write equation (2.113) in a matrix form like (2.92) if we define:

$$\mathbf{K} = \left[\left(\partial_i\varphi_k, \kappa_{ij}\,\partial_j\varphi_l\right)\right]_{(\eta-\eta_D)\mathrm{x}(\eta-\eta_D)} \tag{2.114}$$

$$\mathbf{F} = \left[\; \varphi_k, H \; - \; \varphi_k, q_1 \;_{\partial\Omega} - \sum_{l\in\eta_D} \partial_i\varphi_k, \kappa_{ij}\partial_j\varphi_l \;\; T_{0\,l} \right]_{(\eta-\eta_D)\,\mathrm{x1}} \tag{2.115}$$

$$\mathbf{t} = \; t_l \;_{\eta-\eta_D\;\mathrm{x1}} \tag{2.116}$$

2.1.1.5. Time dependent equations.

In the previous sections the discrete form of the stationary heat equation has been obtained, but it is also interesting to study how this is done for a time dependent equation. To do so, lets use the generalized heat conduction equation:

$$\rho c \partial_t T - \partial_i \kappa_{ij} \partial_j T = H \tag{2.117}$$

where ρ is the density, c is the specific heat and ∂_t is the temporal derivative. The boundary conditions are similar to (2.101) and (2.102) but, to have a unique solution we need to have also an initial temperature T_{in}.

Now, proceeding as in section 2.1.1.3 we obtain:

$$w^h, \rho c \dot{\tau}^h + \partial_i w^h, \kappa_{ij} \partial_j \tau^h = w^h, H - w^h, H_{\partial\Omega} - w^h, \rho c \dot{\tau}_0^h - \partial_i w^h, \tau_0^h \tag{2.118}$$

$$w^h, \rho c \tau^h(0) = w^h, \rho c T_{in} - w^h, \rho c \tau_0^h(0) \tag{2.119}$$

where $\dot{\tau}$ stands for $\partial_t \tau$ and the terms with *0* subscript are evaluated at the initial time-step. In equation (2.118) we have two new terms corresponding to the temporal derivative of *T*. Equation (2.119) is the equation corresponding to the initial temperature. As before we need to expand w^h, τ^h and τ_0^h in terms of the shape functions, but in this case:

$$\tau^h(\mathbf{x}, t) = \sum_{k \in \eta - \eta_D} \varphi_k(\mathbf{x}) t_k(t) \tag{2.120}$$

$$\tau_0^h(\mathbf{x}, t) = \sum_{k \in \eta_D} \varphi_k(\mathbf{x}) T_{0\,k}(t) \qquad T_{0\,k} = T_0(\mathbf{x}_k, t) \tag{2.121}$$

The shape functions are identical to the ones in section 2.1.1.3, and all the time dependency is held in the nodal values t_k. Substituting (2.120) and (2.121) in (2.118) we obtain the next matrix equation:

$$\mathbf{M}\dot{\mathbf{t}} + \mathbf{K}\mathbf{t} = \mathbf{F} \tag{2.122}$$

$$\mathbf{M} = \left[\varphi_k, \rho c \varphi_l \right]_{(\eta - \eta_D) \times (\eta - \eta_D)} \tag{2.123}$$

$$\mathbf{K} = \left[\partial_i \varphi_k, \kappa_{ij} \partial_j \varphi_l \right]_{(\eta - \eta_D) \times (\eta - \eta_D)} \tag{2.124}$$

$$\mathbf{F} = \left[\varphi_k, H \;-\; \varphi_k, q_1 \;_{\partial\Omega} - \sum_{l \in \eta_D} \mathbf{M}_{kl} \dot{T}_{0\,l} + \mathbf{K}_{kl} T_{0\,l} \right]_{(\eta - \eta_D)\mathrm{x}1} \tag{2.125}$$

Now the problem is reduced to solve equation (2.122) in order to obtain $\dot{\mathbf{t}}$ and $\mathbf{t}$. There are several approaches to do it, but the most common ones are members of the *generalized trapezoidal family of methods*. For simplicity, only one example of these methods is presented here, for more details refer to Hughens (2000).

To solve the problem, we use the equations:

$$\mathbf{M}\,\dot{\tau}_{n+1} + \mathbf{K}\,\tau_{n+1} = \mathbf{F}_{n+1} \tag{2.126}$$

$$\tau_{n+1} = \tau_n + \Delta t \dot{\tau}_{n+\alpha} \tag{2.127}$$

$$\dot{\tau}_{n+\alpha} = (1-\alpha)\dot{\tau}_n + \alpha \dot{\tau}_{n+1} \tag{2.128}$$

where the subscripts refer to the time-step, Δt is the length of each time-step and α is a parameter with values between one and zero. The problem is solved if we can obtain τ_{n+1} and $\dot{\tau}_{n+1}$ known τ_n and $\dot{\tau}_n$. A way to proceed is to use a prediction of τ_{n+1}:

$$\tilde{\tau}_{n+1} = \tau_n + (1-\alpha)\Delta t \dot{\tau}_n \tag{2.129}$$

Combining equations (2.126) to (2.129) we obtain:

$$\mathbf{M} + \alpha \Delta t \mathbf{K} \;\; \dot{\tau}_{n+1} = \mathbf{F}_{n+1} - \mathbf{K}\,\tilde{\tau}_{n+1} \tag{2.130}$$

where the only unknown is $\dot{\tau}_{n+1}$. Once $\dot{\tau}_{n+1}$ is obtained, we can use equations (2.127) and (2.128) to obtain τ_{n+1}.

2.1.1.6. Conservation of momentum and energy.

The weak and discretized forms of the equation of conservation of momentum and energy are found in a similar way as has been presented in the previous sections. However, provided that several different approximations can be adopted, showing here their final discretized forms would be repetitive, so it is omitted.

Anyhow, it should be taken into account that after applying the anelastic liquid approximation, equations (2.49)-(2.51), the time dependency disappears from the equation of motion. The fundamental basis for the numerical solution of any time-dependent convection problem is the sequential solution of all the equations in three steps:

- First, the equations of Navier-Stokes are solved for the velocity and pressure using the density and viscosity from the previous time-step.
- Second, using that velocity field, τ_n and $\dot{\tau}_n$ in the energy equation, we obtain the temperature field for the next time-step, obtaining τ_{n+1} and $\dot{\tau}_{n+1}$, where the subscript *n* denotes the time-step.
- Third, with the new velocities (which lead to a new strain rate) and temperature, the new viscosity and density structures are computed using equations (2.30) or (2.31) depending on whether plastic yielding is considered or not.

To obtain the discrete form of the equations and solve the corresponding linear system we have used two different codes. In Chapters 3 and 4 we have used the commercial software Comsol Multiphysics and the direct solver PARDISO (*Schenk and Gärtner*, 2004, 2006) and in Chapter 5 we use the code CitcomS (*Zhong et al.*, 2000; *Tan et al.*, 2006) and the iterative solver Geometric Multi-grid.

2.2.2 Comsol Multiphysics and PARDISO solver.

COMSOL Multiphysics® is an interactive environment for modeling and solving problems based on partial differential equations by adopting a FEM together with error control using a variety of numerical solvers. The software includes a set of built in equations, amongst these, equation of conservation of momentum and energy are included. The equations set by the software can be modified in order to better adapt them to the problem. For example, the equation of conservation of momentum included in Comsol Multiphysics corresponds to equation (2.15), but we modify it to adopt the ALA, equation (2.50).

Comsol Multiphysics also offers the possibility of coupling different PDE (in this case the equations of conservation of momentum and energy), defining material property laws (as the density, or the viscosity), define different initial states (the initial temperature or velocity), modifying the boundary conditions,

choose different meshes (one of the most important advantages of Comsol is the flexibility of the mesher), elements types and solvers. Finally, the software can be coupled to Matlab in order to implement new iterative processes or create functions to help the post-processing of the data.

In 2D problems, direct solvers are very efficient for sparse matrix as the number of degrees of freedom is not too large. The aim of a direct solver is to solve a linear system using finite number of operations. The simplest approach to solve a linear system using a direct algorithm is the Gauss elimination. This algorithm has two steps: the forward elimination in which the system matrix is transformed into a triangular matrix through elementary row operations (multiplying rows, switching rows, and adding multiples of rows to other rows), second, the back substitution to turn the matrix into a diagonal matrix and find the solution of the system.

Gaussian elimination is the basis for LU factorization in which the system matrix is decomposed as:

$$\mathbf{LU} = \mathbf{M} = \mathbf{PA} \tag{2.131}$$

where **L** is a lower triangular matrix, **U** an upper triangular matrix **P** is the pivoting matrix (pivoting is used to improve the numerical stability and is very important for sparse matrices) and **A** is the original matrix. Using this decomposition, the problem is reduced to first solve $\mathbf{Ly}=\mathbf{b}$ and then $\mathbf{Ux}=\mathbf{y}$. Being **U** and **L** two triangular matrices, solving these two systems is easier**.**

In Comsol Multiphysics the most memory-efficient direct solver is PARDISO. It is used for solving large sparse symmetric and unsymmetric linear systems of equations on shared-memory and distributed-memory multiprocessors. As explained above, this kind of problems, involving sparse linear systems, are generally addressed by using parallel sparse direct Gaussian elimination, which requires a lot of pivoting to maintain numerical stability in direct methods. Partial pivoting is the key to ensure robustness of a sparse matrix, but it is computationally demanding. PARDISO preprocesses the coefficient matrix **A** to improve the efficiency with the minimum loss of robustness. To do so, complete block supernode diagonal pivoting is used. A super node is a group of consecutive rows and columns that have the same structure in the factors L and U. An interchange among the rows and columns of a supernode (referred to

as complete block diagonal supernode pivoting) has no effect on the overall fill-in and this is the mechanism for finding a suitable pivot in PARDISO. Also, the code is parallelized, so it can run on several shared memory multi-processors.

Once the solver has found a solution, Comsol checks its validity by comparing the relative residual with a given tolerance.

$$residual = \frac{\left| M^{-1} \mathbf{b} - A\mathbf{x} \right|}{\left| M^{-1}\mathbf{b} \right|} \leq tol \tag{2.132}$$

where **M**=**LU** (**L** and **U** are the LU factors computed by the solver) and $|\text{-}|$ is the Euclidean norm of a matrix, defined as:

$$|A| = \sqrt{\sum_{ij} a_{ij}} \tag{2.133}$$

If this convergence criterion is not fulfilled, Comsol yields an error message and the solver stops.

Due to the high non-linearity of the equations it is usual that after several time-steps, the convergence criterion (2.132) is no longer fulfilled. When this happens is necessary to take a step backwards and restart the time dependent process from a previous convergent solution. We couple Comsol and Matlab to use an iterative procedure (Figure 2.6) to deal with problems of non-convergence associated with non-linear rheology.

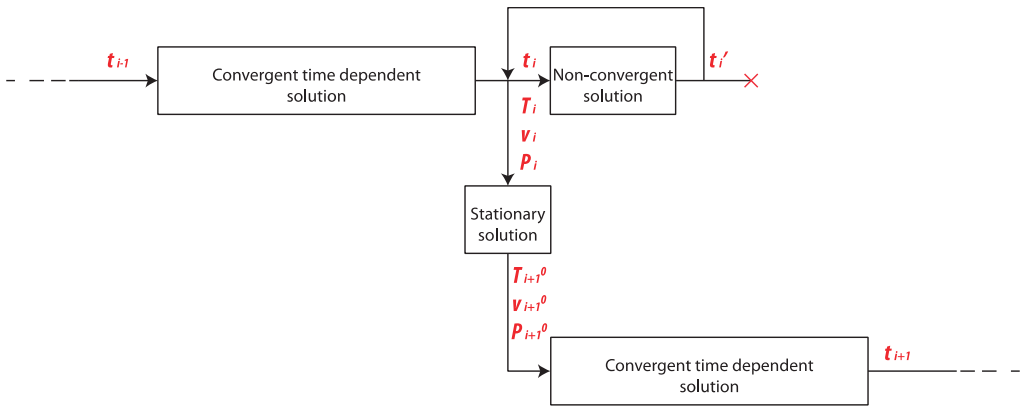

Figure 2.6: Diagram of the iterative process used to deal with a non-convergent time dependent problem in Comsol.

- When at time t_i' the solution does not fulfill the convergence criterion, the solver stops.

- At that point we take the last convergent solution, obtained at time $t_i<t_i$', and use v_i, P_i and T_i to calculate η_i.

- To achieve a more stable process we compute the stationary solution of the momentum equation for T_i and η_i and we obtain $v_{i+1}{}^0$ and $P_{i+1}{}^0$.

- We now restart the time dependent process and solve the momentum and energy equations using $v_{i+1}{}^0$ and $P_{i+1}{}^0$ and the temperature from the previous time-step T_i.

2.2.3 CitcomS and the Geometric Multi-grid Solver.

In order to solve three-dimensional problems at a high resolution, including complex rheologies, we need to use a code that runs in several processors simultaneously (parallelized environment). CitcomS, an open source code distributed and maintained at Computational Infrastructure for Geodynamics (http://www.geodynamics.org/cig/software/citcoms), fulfills these requirements. Also, a wide community uses this code and therefore, it has been widely benchmarked.

CitcomS is a finite element code written in C that solves for 3D thermo-chemical convection within either a full or a restricted spherical domain. The software has been reengineered from previous versions of CitcomS to work within a Python-based framework (Pyre). This new version of the code allows for launching numerical simulations in parallelized environments.

The first version was called Citcom (for California Institute of Technology Convection in the Mantle), was written in the early 1990s and its fundamental finite element infrastructure is still in place and forms the basis for much of the code contained in the present release. In the mid-1990s a version of the code that solved the equations within three-dimensional cartesian domains was written and the code was successfully parallelized. Also, a new version in spherical coordinates, both for the whole Earth and regional caps, was created and was named CitcomS. An important improvement was the creation of the first Beowulf implementations of the code using the Message Passing Interface (MPI)

library. In order to increase the functionality of CitcomS, the developers began to reengineer the code in 2004 into an object-oriented environment specifically, so it could work with Pyre. The current release of the software is essentially the result of those reengineering efforts.

The second major release of CitcomS (2.0) incorporated the software framework Pyre, free surface modeling methods, and stress boundary conditions on the top and bottom surfaces. The release of CitcomS 2.1 incorporated geoid calculations that had been left out of earlier releases. The release of CitcomS 2.2 incorporated the ability of tracing particles in the flow developed by Allen McNamara and Shijie Zhong in 2004. The tracer code can be used for tracing the trajectory of passive particles, in delineating the top boundary of subducted slabs to define the low viscosity wedges, or in tracking the evolution of the chemical composition field.

The release of CitcomS 3.0 contains many new features, including two implementations of compressible convection, one by Wei Leng and Shijie Zhong and the other by Eh Tan; a rheology option for pseudoplasiticity, composition dependent viscosity and heat generation.

The version currently used in this work also includes some modification made by Magali I. Billen that include the possibility to incorporate an initial temperature distribution from a file and the localization of weak zones from files and enable the possibility to use a composite viscosity.

A wide variety of initial states and boundary conditions can be implemented, what makes CitcomS a versatile code that can be applied to many scenarios. A variable viscosity, defined as a function of temperature, pressure and strain-rate, is an optional input parameter in CitcomS. The code also allows for the generation of refined mesh that can be adapted to the needs of the problem. The code is capable of solving mantle convection problems that include tectonic plates, which makes it a very powerful tool to model subduction processes.

CitcomS allows to set may different models by modifying a wide variety of options. For this work six features have been modified to set up the different models and tests: the mesh, the solver, the velocity boundary conditions, the initial temperature, the weak regions and rheology. Details of how these options can be modified can be found in Appendix A.

As Comsol Multiphysics, CitcomS also solves the governing equations using FEM. The energy equation is solved with a Steamline-Upwind Petrov-Galerkin method (*Brooks*, 1981; *Brooks and Hughes*, 1982). This method modifies the Galerkin shape functions studied in section 2.1.1.3 and creates a new discontinuous function in the form:

$$\tilde{\varphi}_i = \varphi_i + p \tag{2.134}$$

This is applied only in the direction of the flow and the shape functions are modified to weight the element upwind of the node more heavily than the downwind element through the parameter p (Figure 2.7). This method helps improving the stability of convection dominated flows by removing node-to-node oscillations.

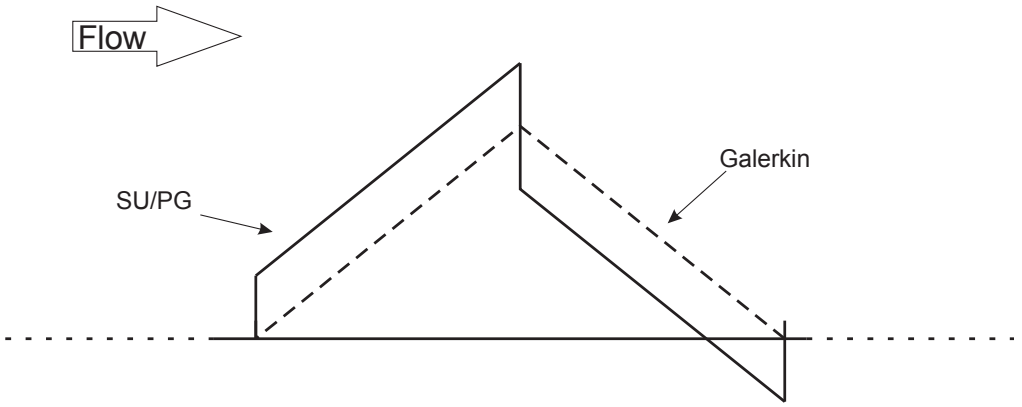

Figure 2.7: Comparison between Galerkin shape functions and Stream Upwind/Petrov-Galerkin (SU/PG) shape functions. Modified from Brooks and Hughes (1982)

It employs an Uzawa algorithm to solve the momentum equation coupled with the incompressibility constraints (*Ramage and Wathen*, 1994; *Moresi and Gurnis*, 1996). Uzawa algorithm simultaneously yields the pressure and the velocity field through two-loop iterations, where the outer loop corresponds to the pressure and the inner loop to the velocity. To solve the pressure, a preconditioned conjugate gradient method is used (see *Shewchuk*, 1994 and references therein), while the velocity is solved using a multi-grid solver (see *Briggs et al.*, 2000 and references therein).

These iterative solvers are chosen for 3D problems as direct solvers are limited to small or low resolution problems because the solution time rapidly scales with the number of unknowns (as N^3-N^2 depending on the solver, where N is the number of degrees of freedom). Iterative methods can achieve much better performance reducing the computing time. For example, preconditioned conjugate-gradient methods scale as $N \cdot \log(N)$. Or better, the geometric multi-grid solver, when properly formulated can find a solution in a time proportional to N.

CitcomS offers a great control over the multi-grid solver parameters, and the success in making models converge relies on understanding how this method and its parameters work. The multi-grid method works by formulating the finite-element problem on several different scales, usually a set of grids that are nested one within the other, sharing common nodes. The solution progresses on all of the grids at the same time, with each grid eliminating errors at a different scale. The multi-grid effect relies on using an iterative solver on each of the grid resolutions. Therefore, is important to understand what an iterative solver is and how it works.

An *iterative* or *relaxation* process can be applied to an equation system in the form $\mathbf{Au}=\mathbf{b}$. If $\mathbf{u}$ is the exact solution and $\mathbf{v}$ is an approximate solution, the error is the difference between the exact and the approximate solutions:

$$\mathbf{e} = \mathbf{u} - \mathbf{v} \tag{2.135}$$

But the exact solution is rarely known, so we define the *residual,* which is given by:

$$\mathbf{r} = \mathbf{b} - \mathrm{A}\mathbf{v} \tag{2.136}$$

The residual is simply the amount by which the approximation $\mathbf{v}$ fails to satisfy the original problem $\mathrm{A}\mathbf{u} = \mathbf{b}$. The error and the residual also satisfy the equation $\mathrm{A}\mathbf{e} = \mathbf{r}$, known as the residual equation. This implies that we once we obtain an approximate solution $\mathbf{v}$ we can compute the residual $\mathbf{r}$ and use the residual equation to obtain a corrected approximation of the solution as $\mathbf{v'}=\mathbf{v}+\mathbf{e}$.

An iterative process generates a sequence of improved approximate solutions. Therefore, if $\mathbf{v}^i$ is the approximate solution in the *ith* step or the

iterative process, it can be obtained from the previous solution $\mathbf{v}^{i-1}$. An example of iterative method is the *Jacobi Method*, where if:

$$A = L + D + U \tag{2.137}$$

where **L**, **D** and **U** are the lower triangular, diagonal and upper triangular matrices, the $\mathbf{v}^i$ can be calculated as:

$$\mathbf{v}^i = D^{-1}(L + U)\mathbf{v}^{i-1} + D^{-1}\mathbf{b} \tag{2.138}$$

A similar method is the *Gauss-Seidel Method*, for which:

$$\mathbf{v}^i = \left(D-L\right)^{-1} U\mathbf{v}^{i-1} + \mathbf{b} \tag{2.139}$$

The main advantage of this method is that the components of the new approximation are used as soon as they are computed, which allows to overwrite the vector each time the new approximation is computed, making the method more memory efficient.

An important observation is that in these methods the standard iterations converge very quickly as long as the error has high-frequency components. However, the slower elimination of the low-frequency components degrades the performance of these methods. These schemes work very well for the first iterations, but inevitably, convergence slows down and the entire scheme tends to stall. The rapid decrease in error during the early iterations is due to the efficient elimination of the oscillatory modes of that error; but once the oscillatory modes have been removed, the iteration is much less efficient in reducing the remaining smooth components. Any attempt to improve the accuracy of the solution (by decreasing the grid spacing) only worsens the convergence of the smooth components of the error.

One way to improve a relaxation scheme, at least in its early stages, is to use a good initial guess. A well-known technique for obtaining an improved initial guess is to perform some preliminary iterations on a coarse grid (relaxation on a coarse grid is less expensive). Also, in a coarse grid, the smooth components of the error seem more oscillatory (Figure 2.8), which makes them decrease faster after each relaxation. This is the basis of a geometric multi-grid method.

Taking this into account, geometric multi-grid methods aim to solve the problem by, starting from an initial guess **v**, compute the error **e** and correct **v** using **v'**=**v**+**e**. The multi-grid solver uses an iterative solver to relax on equations of the type A**u** = **b** in the different grids. When relaxation begins to stall, indicating the predominance of smooth error modes, it is advisable to move to a coarser grid; there, the smooth error modes appear more oscillatory and relaxation is more efficient. Every mesh is considered a level, and the number of levels can be modified depending on the demands of the problems.

Now we assume a process in which there are *N* levels and let the superscript stand for the level in which the linear system is solved, where 1 corresponds to the finest mesh and N to the coarsest one. We can use this procedure:

- Relax on $A^1\boldsymbol{u^1} = \boldsymbol{b^1}$, ℓ' times using the initial guess $\mathbf{v}^1$.
- Compute the residual $\mathbf{r}^1 = \mathbf{b}^1 - A^1\mathbf{v}^1$
- Project $\mathbf{r}^1$ on the next level to obtain $\mathbf{r}^2$
  - Relax on $A^2\boldsymbol{e^2} = \boldsymbol{r^2}$ ℓ' times using the initial guess $\mathbf{e}_0^{\,2}$
  - Compute the residual $\mathbf{r}^{2\prime} = \mathbf{b}^2 - A^2\mathbf{e}_0^{\,2}$
  - Project $\mathbf{r}^{2\prime}$ on the next level to obtain $\mathbf{r}^3$
    - Relax on $A^3\boldsymbol{e^3} = \boldsymbol{r^3}$ ℓ' times using the initial guess $\mathbf{e}_0^{\,3}$
    - Compute the residual $\mathbf{r}^{3\prime} = \mathbf{b}^3 - A^3\mathbf{e}_0^{\,3}$
    - Project $\mathbf{r}^{3\prime}$ on the next level to obtain $\mathbf{r}^4$

    .

    .

      - Solve $A^N\boldsymbol{e^N} = \boldsymbol{r^N}$
      - Project $\boldsymbol{e^N}$ in the previous level to obtain $\boldsymbol{e^{N-1}}$

    .

    .

    - Correct $\mathbf{e}^{3\prime} = \mathbf{e}_0^{\,3} + \mathbf{e}^3$
    - Relax on $A^3\boldsymbol{e^3} = \boldsymbol{r^3}$ ℓ' times using the initial guess $\mathbf{e}^{3\prime}$
    - Project $\boldsymbol{e^{3\prime}}$ in the previous level to obtain $\boldsymbol{e^2}$
  - Correct $\mathbf{e}^{2\prime} = \mathbf{e}_0^{\,2} + \mathbf{e}^2$

- Relax on $A^2 e^2 = r^2$ l^2 times using the initial guess $\mathbf{e^{2,}}$
- Project $e^{2,}$ in the previous level to obtain e^1

- Correct $\mathbf{v^{1,}} = \mathbf{v^1} + \mathbf{e^1}$
- Relax on $A^1 e^1 = r^1$ l^1 times using the initial guess $\mathbf{e^{1,}}$

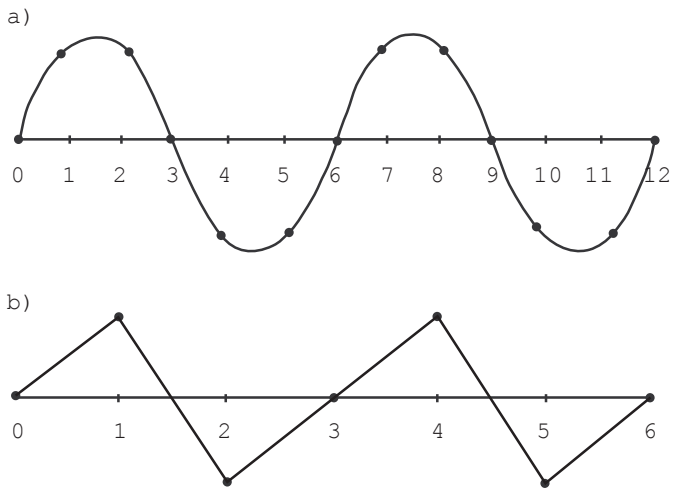

Figure 2.8: Wave with wave number k = 4 on a mesh of (a) n = 12 points and (b) projected onto a mesh of n = 6 points. The coarse grid "sees" a wave that is more oscillatory on the coarse grid than on the fine grid. Modified from Briggs et al. (2000).

This algorithm is known as the *V cycle* provided that it goes down to the coarsest grid and then works its way back to the finest grid. There are other algorithms depending on the path they follow through the levels, as the W cycle and Full Multi-Grid (Figure 2.9). To solve the velocity, we use a V cycle, combined with Gauss-Seidel and Jacobi methods to do the relaxations on each of the levels.

CitcomS also includes an outer iterative process. Once a Geometric Multi-grid process has been completed, the solution is used as the initial guess for a new cycle. This process is repeated until a convergence criterion is achieved twice in a row. There are two different convergence criteria in CitcomS:

$$\frac{\langle \nabla \cdot \rho \mathbf{v} \rangle}{\langle \mathbf{v} \rangle} \leq tol \tag{2.140}$$

$$\frac{\left\langle \mathbf{v}^i - \mathbf{v}^{i-1} \right\rangle}{\left\langle \mathbf{v}^i \right\rangle} \leq tol \qquad \text{and} \qquad \frac{\left\langle \mathbf{p}^i - \mathbf{p}^{i-1} \right\rangle}{\left\langle \mathbf{p}^i \right\rangle} \leq tol \tag{2.141}$$

where $\langle \bullet \rangle$ stands for the volume averaged norm.

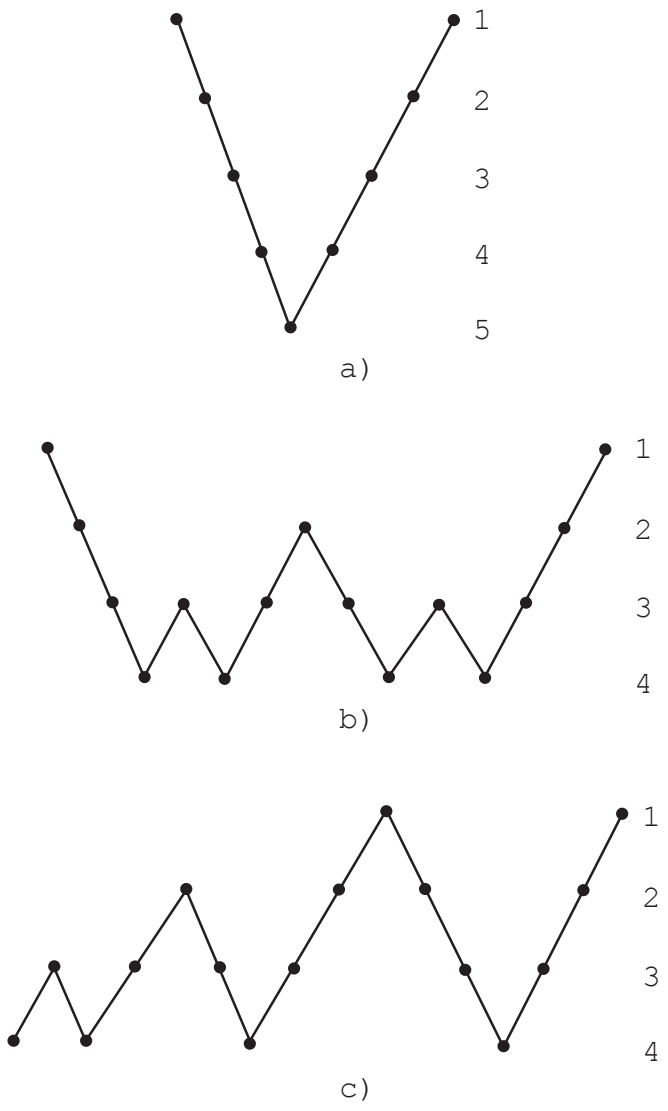

Figure 2.9: Multi-grid algorithm scheme for (a) V-cycle, (b) W-cycle, and (c) Full Multi-grid scheme, all on four levels.

3

INFLUENCE OF THE PLATES THERMAL STATE

3.1. Introduction

As was already mentioned on Chapter 1, significant slab dip variability can be found between different subduction zones, or even along the same subduction zone (*Isacks and Barazangi*, 1977; *Jarrard*, 1986; *Cruciani et al.*, 2005; *Lallemand et al.*, 2005) and different subduction styles can be described (i.e., high-angle, normal, low-angle and flat subduction; Figure 1.2). Owning that one of the main forces driving subduction is the slab-pull, it is expected to find a correlation between older, and therefore colder, subducting slabs and high-angle subduction. However, statistical analysis (*Cruciani et al.*, 2005; *Lallemand et al.*, 2005) show no direct relation between the age of the subducting plate and slab dip (Figure 1.3).

Despite all the possible processes that can perturb or even dominate slab dip, to first order, slab dynamics can be understood as resulting from a balance of driving forces (slab buoyancy) and resisting forces (rheologically-induced). For the evolving dip of the slab, this balance of forces can be discussed in terms of the expected influence of hydrodynamic (viscous) and buoyancy forces on slab dip, while keeping the trench fixed. The gravitational torque per unit slab width t_G resulting from the slab buoyancy of a rigid slab sinking at an angle α is:

$$t_G = \frac{T_G}{D} = \int_0^l \Delta\rho(r,\alpha) g h r \cos\alpha \, dr \tag{3.1}$$

where D is the slab width, $\Delta\rho$ is the density contrast between the slab and the mantle, l is the length of the slab, h is the thickness of the plate and r is the radial coordinate with the origin placed at the base of the lithosphere in the plate boundary. This torque is mainly controlled by the buoyancy of the slab, and thus, it is expected that older (therefore, colder and denser) lithosphere will subduct more steeply than younger lithosphere. It is useful to rewrite equation (3.1) in terms of the mean relative buoyancy per unit slab area b:

$$t_g = \frac{1}{2} b l^2 \cos\alpha \tag{3.2}$$

$$b = gh \int_0^l \Delta\rho(x) dx \tag{3.3}$$

where $x = r^2/l^2$. Equation (3.2) shows that the gravitational torque depends on the slab length, the relative buoyancy and the slab dip (Figure 3.1).

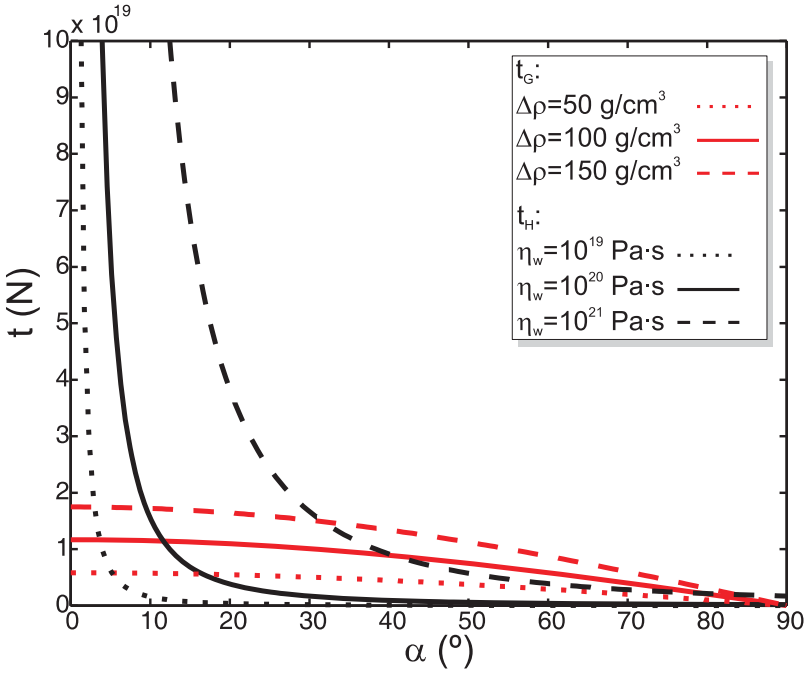

Figure 3.1: Theoretical torques calculated using expressions from Stevenson and Turner (1977). Gravitational torque (red) calculated using equation (3.1) for three different density contrasts $\Delta\rho$ (but uniform for each model), and l = 500 km. Hydrodynamic torque (black) calculated using equation (3.7) for three different mantle viscosities η_w (but uniform) and $u_s = 5\ cm{\cdot}yr^{-1}$.

The gravitational torque is balanced by the hydrodynamic torque per unit slab width t_H, which exerts a suction force on the slab,

$$t_H = \frac{T_H}{D} = \int_0^l P_A(\theta, r) - P_B(\theta, r)\, r dr \tag{3.4}$$

where P_A and P_B are the pressures beneath and above the slab, respectively. McKenzie (1969) obtained the following expression for P_A and P_B assuming constant mantle viscosity and a linear geometry of the slab (Figure 3.1):

$$\mathrm{P_A}(\alpha) = \frac{2\eta_\mathrm{W} \mathrm{u_s} \sin(\alpha)}{\mathrm{r}(\pi - \alpha) + \sin(\alpha)} \tag{3.5}$$

$$P_B(\alpha) = -\frac{2\eta_W u_s \sin^2\alpha}{r\ \alpha^2 - \sin^2\alpha} \tag{3.6}$$

where η is the viscosity in the mantle wedge, α is the slab dip and u_s the subduction velocity. This leads to the following analytical solution for the suction torque (*Stevenson and Turner*, 1977):

$$t_H = 2\eta_W u_s l\left[\frac{\sin\alpha}{\pi - \alpha\ + \sin\alpha} + \frac{\sin^2\alpha}{\alpha^2 - \sin^2\alpha}\right] \tag{3.7}$$

As can be seen in equation (3.7) and Figure 3.1, this torque strongly depends on the viscosity of the mantle wedge and the slab dip (*Stevenson and Turner*, 1977; *Tovish et al.*, 1978). For higher viscosity or smaller dip angles, the hydrodynamic torque causes increased upward suction of the slab.

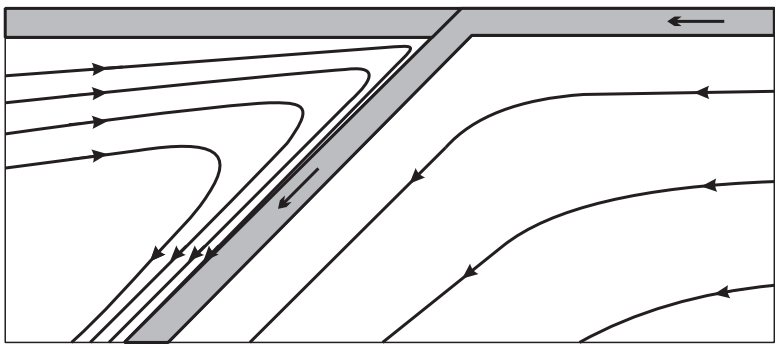

Figure 3.2. Streamlines illustrating the corner flow generated by a subducting slab, from McKenzie (1967).

A number of studies have explored the influence of the viscosity structure of the slab and surrounding mantle on the dynamics of subduction (see King (2007) and Billen (2008) for extensive reviews). For example, van Hunen et al. (2002a, b; 2004, and references therein) explored the influence of the relative velocity of the overriding plate, slab buoyancy and rheological parameters. Cizkova et al., (2002) showed that the slab strength modulated the effects of trench retreat on deep slab dip. Billen and Hirth (2005, 2007) carried out a systematic study of the influence of rheology, slab strength, mantle viscosity and the age of the subducting plate on subduction dynamics. The effect of the structure of the overriding lithosphere and the mantle wedge has been studied in terms of the presence of hydrous materials in the mantle wedge (e.g., *Manea and Gurnis*, 2007;

Arcay et al., 2008) or the presence of continental roots (*O'Driscoll et al.*, 2009). Eberle et al. (2002) investigated the effect of the boundary condition on the upper plate (fixed vs. free slip) on the thermal and viscosity structure in the mantle wedge. Roda et al. (2011) investigated the influence of the thickness of an overriding continental plate on slab dip, and found that it decreases with the increase in the upper plate thickness.

In this study we hypothesize that some of the observed variability in slab dynamics and geometry may be controlled by the variation in the thermal state of the overriding plate. To quantitatively test this hypothesis, we investigate the influence of the thermal state of both overriding and subducting plates on slab dip using 2D thermo-mechanical models for an ocean-ocean subduction. We note that while the modeling setup and rheology used in this study is similar to the study by Billen and Hirth (2007), in contrast with their models, which did not consider the effect of the overriding plate and obtained significant slab dip variations only after the slab was partially supported by the high lower-mantle viscosity, we focus here on shallow mantle processes controlling slab dip and subduction style.

3.2. Modeling strategy

3.2.1. Governing equations and numerical method.

The model domain represents a vertical section running parallel to the subduction direction, in which equations of conservation of mass, momentum and energy are solved. We assume that the fluid is incompressible and has a high Prandtl number, which allows us to neglect inertial forces on the momentum equation. We also assume the extended Boussinesq approximation (EBA), neglect shear heating and consider only density variations due to temperature changes and solve equations (2.61)-(2.63).

These coupled equations are solved using the finite-element code included in the software COMSOL Multiphysics 3.5a (section 2.2.2). We use the direct solver PARDISO included in the software, because it is faster and requires less memory than other solvers. The modeled section is discretized through a mesh of triangular elements whose density varies from one element every 2 km in the area

of the plate boundary to one every 150 km in the lower mantle (Figure 3.3.a). For the momentum equation we use Lagrange P2-P1 elements, which are quadratic in velocity and linear in pressure. Lagrange Quadratic elements are used to model the temperature field.

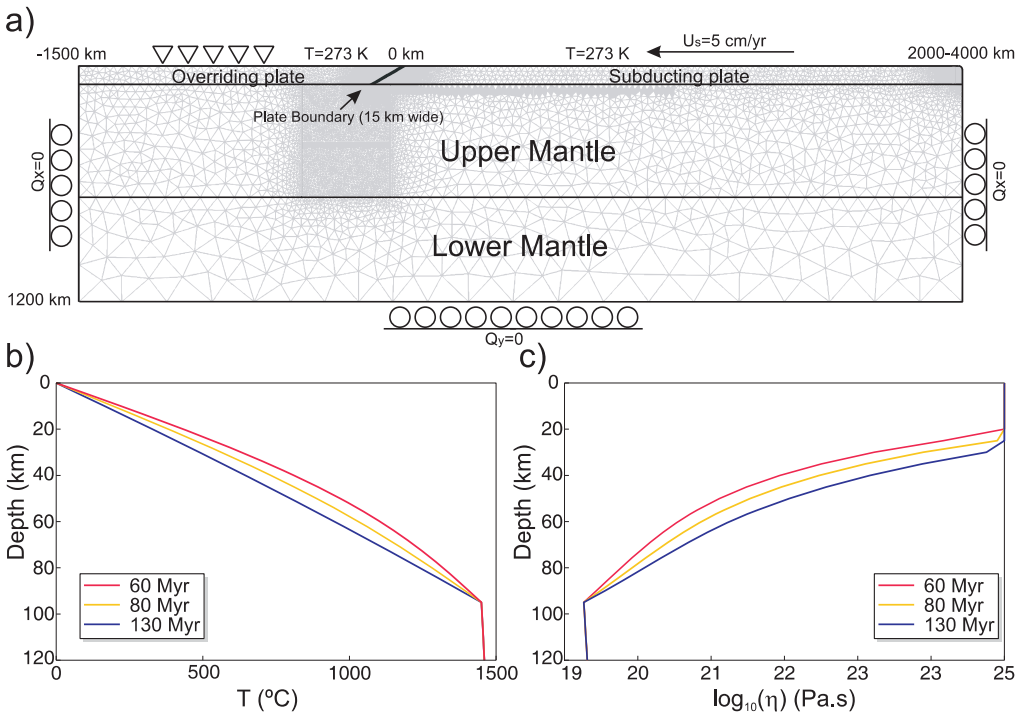

Figure 3.3: Model setup. a) Schematic representation of the modeled 2D vertical cross section showing the finite element mesh and boundary conditions. Note the modeled domain width is varied from 3500 to 5500 km to allow for models with different (but constant through time) subducting plate age at the plate boundary. b) Initial temperature and c) viscosity profiles for three different plate ages. A reference effective strain rate of 10^{-15} s^{-1} and a maximum viscosity cut-off of $\eta_{max}=10^{25}$ $Pa{\cdot}s$ are assumed.

3.2.2. Model setup

The modeled vertical section is 1200 km deep and it includes the lithosphere, sublithospheric upper mantle and a portion of the lower mantle (Figure 3.3.a). The width of the modeled section changes from 3500 to 5500 km to control the age of the subducting plate (see section 3.2.3). In order to reproduce subduction, we impose a constant velocity u_s = 5 cm·yr^{-1} at the upper boundary of the subducting plate, whereas the upper boundary of the overriding plate is fixed. This condition of a fixed overriding plate has been shown to be in better agreement than a

free-slip condition with geophysical observations, as it leads to tectonic erosion of the lower lithosphere of the overriding plate causing high-temperatures, low seismic velocities, high attenuation and high heat flow beneath volcanic arc (*Eberle et al.*, 2002). The plates are separated by a plate boundary modeled as a narrow low viscosity zone. A free slip boundary condition is applied to the bottom and side boundaries of the model domain. The modeling is not able to properly simulate the dynamics of plate bending at the trench because vertical motion on the top surface is not allowed. While the surface boundary conditions may affect bending of an elastic slab at very shallow depths, because the slab is viscous it has no memory of how it deforms going into the trench nor is it able to transmit "bending" stresses down dip. Therefore, we consider that the surface boundary conditions can not affect the deeper deformation of the slab.

The imposed velocity condition on the top of the subducting plate is necessary to initiate subduction and facilitates controlling both the subduction velocity and the subducting plate age. However, it is a modeling constrain and it is therefore important to be clear about what it represents and what influence it is expected to have on the subduction results.

First, this boundary condition is used to account for convergence caused by the combination of forces driving subduction, but not included in the 2D cross section modeled here, without making any hypothesis about the relative importance of these forces. For example, Conrad and Lithgow-Bertelloni (2002; 2004) found that the velocities of the plates were best predicted when about half of the driving force came from net slab pull (balance between slab pull and subduction resistance) and half came from slab suction and distributed basal tractions due to the convection which the slabs (even detached) induce in the lower mantle. Moreover, even if subduction was entirely driven by the negative buoyancy of the full (3D) slab, locally the slab dynamics may be affected by regional features such as the presence of buoyant oceanic plateaus (e.g., *van Hunen et al.*, 2002b, 2004) or changes in the thermal state of the overriding plate. Therefore, the negative buoyancy of the full slab could continue to pull the slab down even if locally other forces resist subduction and the 2D section of the slab is unable to fully drive subduction.

Second, previous studies show that for weak to moderately strong slabs, the evolution of the slab in the mantle is not controlled by the kinematic boundary

condition (*Han and Gurnis*, 1999). Similarly, Billen and Hirth (2007) showed that with the type of rheology being used, most of the work done by the boundary condition is dissipated within the subducting plate and bending region and therefore the slab dynamics in the mantle is free to evolve in response to the local forces.

Therefore, while the kinematic boundary condition on the subducting plate is not ideal, nor realistic, it facilitates incorporating the net effect of large-scale mantle flow and out-of-cross-section (3D) plate driving forces with confidence that the boundary condition does not itself control the evolution of the subducting slab.

3.2.3. Initial Thermal Structure

The temperature distribution in the lithosphere is defined by the plate cooling model (first described by *McKenzie*, 1967). This thermal model for the oceanic lithosphere assumes that the temperature is kept constant at the surface and at a given depth L, which defines the plate thickness. This 'plate thickness' is often referred to as the asymptotic (in the limit of very old lithosphere) lithospheric thickness. The plate cools down from an initial temperature (at the ridge) that is uniform across the plate thickness, and therefore its thermal state is controlled by its age. We use the solution for the temperature distribution (assuming a surface temperature of 0 ºC) given by Carslaw and Jaeger (1984).

$$T_{lit}(y,t') = T_L\left[\frac{y}{L} + \sum_{n=1}^{\infty}\frac{2}{n\pi}\sin\left(\frac{n\pi y}{L}\right)\exp\left(-\frac{n^2\pi^2 kt'}{\rho C_p L}\right)\right] \qquad (3.8)$$

where T_L is the temperature at the base of the plate (y=L) and at the ridge, L is the plate thickness and t' is the age of the lithosphere (parameters listed in Table 3.1). We adopt the values T_L=1450 ºC and L=95 km, from plate model GDH1(*Stein and Stein*, 1992). In contrast with Roda el al. (2011), who modified the thermal state of both plates only by changing their thicknesses, our choice of the plate cooling model requires that the plate thickness is kept constant while the thermal state is modified by varying the lithospheric age (Figure 3.3.b). Therefore, an advantage of using a plate model is that it allows us to isolate the temperature effects, as the plate thickness is held constant. The age of the subducting plate increases with the distance from the right boundary, which

represents an oceanic ridge. Models are designed to keep a constant subducting plate age in order to analyze the effects of plate age without other complications. The age of the subducting lithosphere at the plate boundary is computed as $t'=D_r/u_s$, where D_r is the distance from the plate boundary to the right model boundary. Therefore, as the subduction, u_s=5 cm·yr^{-1}, is maintained constant in all the models, D_r is changed from one model to another to modify the age of the subducting lithosphere at the plate boundary. Accordingly, the width of the modeled section is varied between 3500 and 5500 km to change the age of the subducting plate at the plate boundary from 40 to 80 Myr, respectively. For simplicity, the crust is not included in either plate and a uniform age is used for overriding plate (except for Models F and G, see Table 3.2).

Beneath the lithospheric plate**,** we impose an adiabatic distribution for the mantle temperature:

$$T_m(y) = T_L \exp\left(\frac{g\alpha}{C_p}(y-L)\right) \tag{3.9}$$

The bottom and side boundaries are thermally insulated and the upper boundary is set to a fixed temperature of 273 K for both plates.

3.2.4. Rheology

We use a composite rheology, equations (2.29) and (2.30) for which the total strain-rate is given by the sum of the strain-rate accommodated by diffusion creep and the strain-rate accommodated by dislocation creep at the same stress. In addition, we impose a maximum viscosity cut-off, η_{max}=10^{25} Pa·s, for cold temperatures in which the viscosity laws given here are no longer applicable, but we do not impose a minimum viscosity cut-off. Figure 3.3.c shows initial viscosity profiles over the range of ages used and assuming a strain rate of 10^{-15} s^{-1}. Rheological parameters for these models are listed in Table 3.1.

While these models do not include plastic yielding (but strength is limited by a maximum viscosity cut-off), previous models (*Billen and Hirth*, 2007; *Faccenda et al.*, 2009) have shown that the slab yields throughout its thickness as it enters the trench: once the material has yielded it no longer has any elastic strength.

Therefore elasticity is neglected in this study, as we focus on deeper plate deformation processes.

Table 3.1:Model parameters

Symbol	Meaning	Value	
u_s	Subduction velocity	5 cm yr^{-1}	
W	Domain horizontal extent	3500 to 5500 km	
H	Domain vertical extent	1200 km	
L	Lithospheric thickness	95 km	
T_L	Temperature at the base of the lithosphere	1723 K	
k	Thermal conductivity[b]	3.2 W m^{-1} K^{-1}	
α	Thermal expansion coefficient[a]	3.7×10^{-5} K^{-1}	
C_p	Specific heat[b]	1.3×10^{3} J K^{-1} kg^{-1}	
ρ_0	Reference density (at 273 K)[a]	3400 kg m^{-3}	
	Shear zone width/dip	15 km/30°	
η_b	Maximum viscosity at the shear zone	10^{21} - 3×10^{22} Pa s	
η_{max}	Maximum viscosity	10^{24} - 10^{25} Pa s	
	Rheological Parameters [c]	**Diffusion**	**Dislocation**
n	Stress exponent	1	3.5
A	Preexponential factor (Pa)	1	$90\cdot10^{-21}$
E	Activation energy (J/mol·mol^{-1})	335000	480000
V	Activation volume (m^3·mol^{-1})	$4.0\cdot10^{-6}$	$11.0\cdot10^{-6}$
d	Grain size (m)	10^{-2}	
p	Grain size exponent	3.0	
C_{OH}	OH concentration (ppm-H/Si)	1000/1	1000/1
r	C_{OH} exponent	1.0	1.2

[a] Schmeling et al. (1999)

[b] Schubert et al. (2001)

[c] Hirth and Kohlstedt (2003)

We also impose a narrow low viscosity region at the plate boundary. This low viscosity channel is intended to simulate a fault that decouples both plates without producing singularities on the stress distribution (*Kukaèka and Matyska*, 2004; *Billen and Hirth*, 2007). Viscosity, geometry, depth and width of this weak region have great influence on the dynamics of subduction (*Jischke*, 1975; *Kincaid and Sacks*, 1997; *Chen and King*, 1998; *de Franco et al.*, 2007; *Manea and Gurnis*, 2007; *Burkett and Billen*, 2009). In the reference model the low viscosity channel is 15 km wide and 95 km deep and with a maximum allowed viscosity of η_b=3·10^{22} Pa·s. This value is an upper bound of the viscosity in the shear zone and it can be lower than this upper bound as a result of the applied temperature and stress-dependent rheology. Results of tests with different values of this maximum viscosity cut-off of the weak zone are reported in section 3.3.4.4. The shear zone depth is chosen to reach the base of the overriding plate such that the subducting plate can slide uniformly along the boundary. A shorter shear zone leads to strong viscous coupling between the subducting and overriding plate, which prevents subduction. A constant dip of 30º is imposed, which is consistent with the mean value of slab dip at shallow depths (32º ± 11º) obtained by Lallemand et al. (2005).

Including a low strength crust on the subducting plate would eliminate the need to impose a fixed low viscosity zone as it would feed dynamically the low viscosity region at the plate boundary. This would allow the interplate contact to react dynamically and adjust its dip and position. However, we prefer to fix the trench with an imposed weak channel because it allows the effect of the overriding plate thermal structure and mantle wedge dynamics to be isolated from other effects.

3.3. Results

Here I present the results of a suite of models designed to determine the relative importance of the thermal state of the overriding and subducting plates in controlling the slab dip. We also test the effect of the viscosity at the plate boundary and of the maximum overall viscosity. Table 3.2 lists the parameters for the most representative models completed for this study. Time snap-shots of models with letters A–D are shown in Figure 3.4.

Table 3.2: Parameters for the most representative models completed for this study.

Model	A_{ov} (Myr)	A_{sub} (Myr)	η_{max} (Pa·s)	η_b (Pa·s)	u_s (cm·yr^{-1})	L (Km)	T_L (^oC)	Subduction style
A	60	50	10^{25}	$3\cdot10^{22}$	5.0	95	1450	Reference model
B	60	70	"	"	"	"	"	High angle subduction
C	130	70	"	"	"	"	"	Low angle subduction
D	80	50	"	"	"	"	"	Flat subduction
E	60	70	"	"	"	125	"	High angle subduction
F	130	70	"	"	"	125	"	Coupled
G	60	70	"	"	"	125	1350	Intermediate subduction
H	130	70	"	"	"	125	1350	Coupled
I	60	40	"	"	"	"	"	Coupled
J	150/80	50	"	"	"	"	"	Coupled
K	40/60	40	"	"	"	"	"	Flat subduction
L	80	40	10^{24}	10^{21}	"	95	1450	Coupled
M	30	40	10^{24}	10^{21}	"	"	"	High angle subduction
N	200	50	10^{24}	10^{21}	"	"	"	Flat subduction
O	80	50	10^{25}	$3\cdot10^{22}$	7.5	"	"	High angle subduction
P	60	40	"	"	7.5	"	"	Intermediate angle
Q	60	70	"	"	2.5	"	"	Low angle subduction
R	130	70	"	"	2.5	"	"	Coupled

In order to study the dynamics of the subduction process though the different models, we focus on the geometry of the slab, in particular on the angle of subduction. The angle of subduction that results in the models varies significantly with depth, so I present the results in two different depth ranges: α_s is the mean shallow angle, measured between 100 and 200 km, and α_d is the mean deep angle measured between 300 and 400 km**.** The mean angle in each depth interval is computed automatically using tracers located at the surface of the slab.

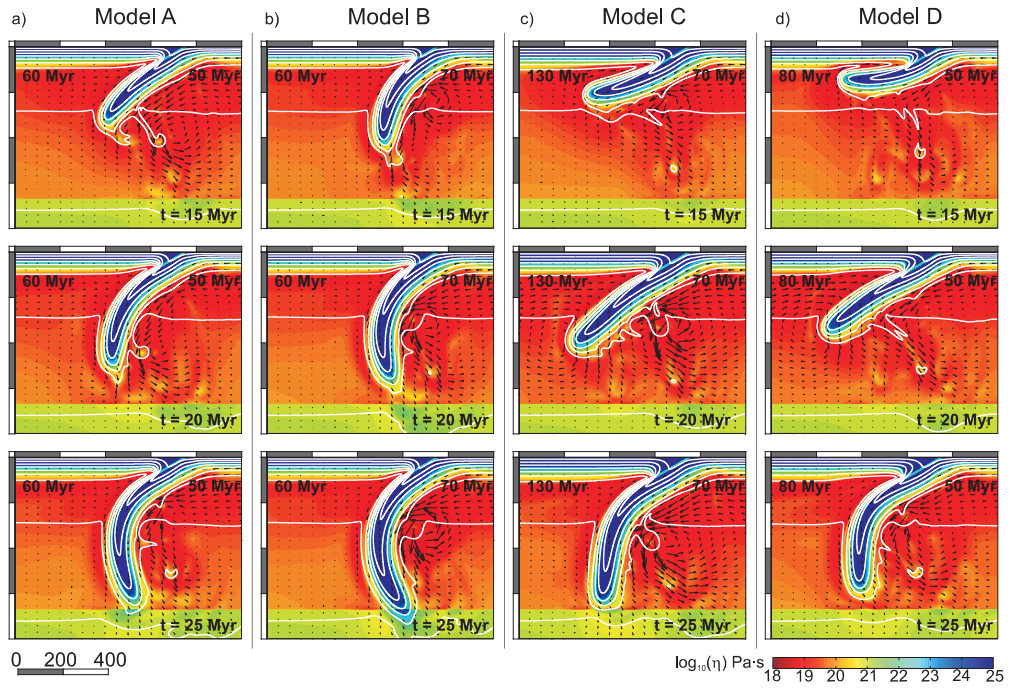

Figure 3.4: Model results at three different evolution times for different ages of the overriding and subducting plates (Table 3.2). The four different simulations are examples of different styles of subduction: a) Model A: reference model. b) Model B: high-angle subduction. c) Model C: low-angle subduction. d) Model D: flat subduction. Decimal logarithm of the viscosity (color), isotherms every 200 K (contour) and velocity field (arrows) are shown. Subducting plate moves at 5 cm·yr^{-1}.

In order to facilitate the interpretation of the results, we compute the gravitational and suction torques exerted by a rigid (but curved) slab with the geometry obtained at each time-step. We use equations (3.1) and (3.4), which require the calculation of the density contrast and the dynamic pressure. We compute the dynamic pressure (hereafter, referred to as the pressure) 10 km above the slab (defined by tracers), and neglect the contribution of the pressure beneath the slab as we obtain that it is much lower than the pressure above it. We also neglect the pressure contribution below 300 km deep as pressure is expected to tend to zero with depth for slab-induced corner flow. It is important to keep in mind that the modeled slab is viscous and bends in response to the local torque balance, therefore actual torques are not uniformly affecting the entire slab, and the gravitational torque has more effect in the deeper portion of the slab whilst the suction torque mainly affects the shallow portion, resulting in a variable dip along the slab.

It is important to note that the slab dip and both the suction and gravitational torques are correlated and variations on the slab dip modify both torques and viceversa. Therefore, one must be careful when interpreting the results as the relationship is not trivial.

3.3.1. Reference model

The reference model established for comparison purposes (Model A, in Figure 3.4.a, Figure 3.5.a and Video 3.A[5]) includes an overriding plate of 60 Myr and a subducting plate of 50 Myr. At the beginning of the simulation the subducting plate bends and penetrates into the mantle. As the slab reaches greater depths, the gravitational torque increases (Figure 3.5.a), and the subduction angle also increases. The gravitational torque tends to stabilize with time due to the competing effects of increasing slab length and dip (equation (3.2)) and after an evolution of around 25 Myr the slab reaches a steady state and the angle of subduction remains almost constant. No substantial variation of the slab dip occurs as the slab reaches the lower mantle, provided that the viscosity contrast between the upper and the lower mantle is of only one order of magnitude. At evolution times greater than 35 Myr, the slab approaches the base of the modeled domain and the results are no longer realistic.

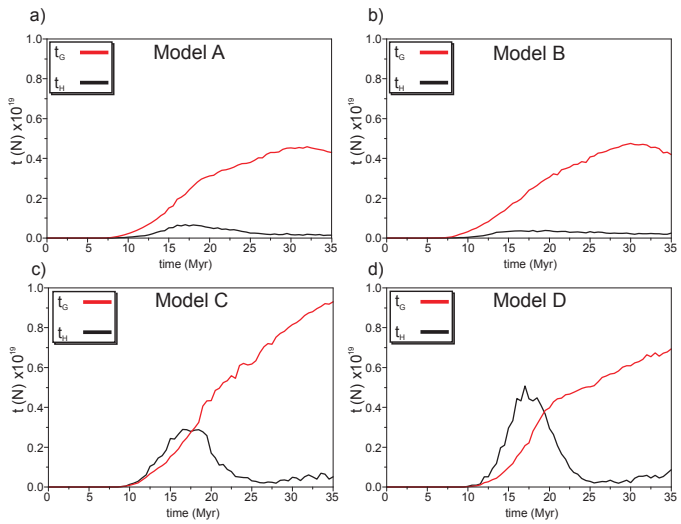

Figure 3.5: Time evolution of the gravitational (red) and hydrodynamic (black) torques per unit slab width for the four models shown in Figure 3.4.

[5] All videos can be found in http://tinyurl.com/thesis-JRG-videos

The viscosity on the surface of the slab is low due to the high strain rate. This reduced viscosity causes a decrease of the hydrodynamic torque and a higher angle of subduction compared to simulations with Newtonian rheology (*Billen and Hirth*, 2005).

3.3.2. Influence of thermal state of the subducting plate

We run several models in which we systematically vary the age of the subducting plate (by changing the distance from the plate boundary to the ridge) in order to control its thermal state. The results show that during the first 15 Myr of evolution, the influence of the thermal state of the subducting plate is significant (compare models A and B at this time in Figure 3.4.a and b). As expected, the gravitational torque is slightly higher for older subducting plates as a result of the increased negative buoyancy (Figure 3.6.a), which in turn causes older plates to subduct with higher angles (Figure 3.4.a and b and Figure 3.7.a).

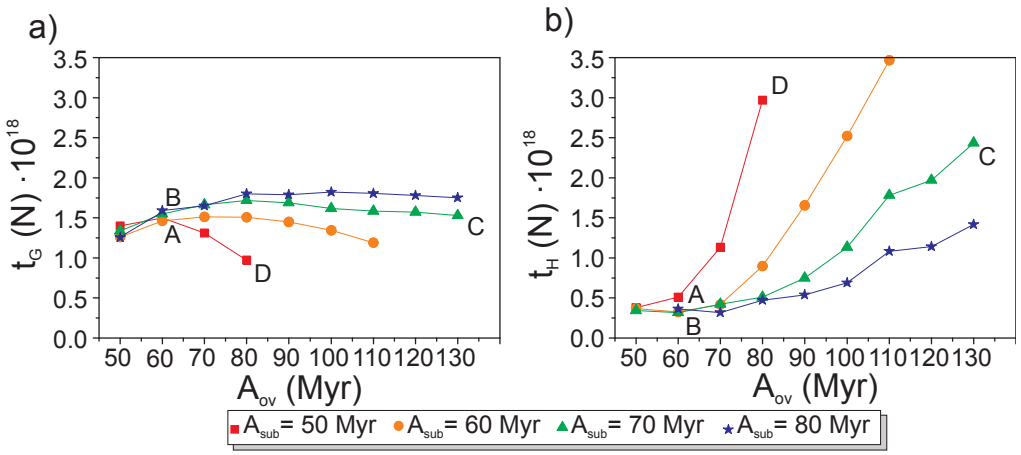

Figure 3.6: Influence of the overriding plate on the (a) gravitational and (b) hydrodynamic torques. Torques per unit slab width as a function of the age of the overriding plate for different ages of the subducting plate, after 15 Myr of evolution. Capital letters in the panels indicate models A-D shown in Figure 3.4 and Table 3.2.

This slab dip variability with the age of the subducting plate is more significant for older overriding plates. For example, at times less than 15 Myr, for an overriding plate of 80 Myr, simulations predict a shallow slab dip from ~5° (flat) for a 50 Myr subducting plate age, and the slab dip increases up to as ~45° for an subducting plate age of 80 Myr (Figure 3.7.a). In contrast, there is almost no variation in slab dip with subducting plate age for an overriding plate of 50 Myr

(Figure 3.7.a). This effect can be understood studying equation (3.2). This equation shows how the gravitational torque is more sensitive to changes in the slab buoyancy for smaller angles (Figure 3.1), which in turn are achieved when the subduction takes place under an older overriding plate, as is explained in detail in the next section.

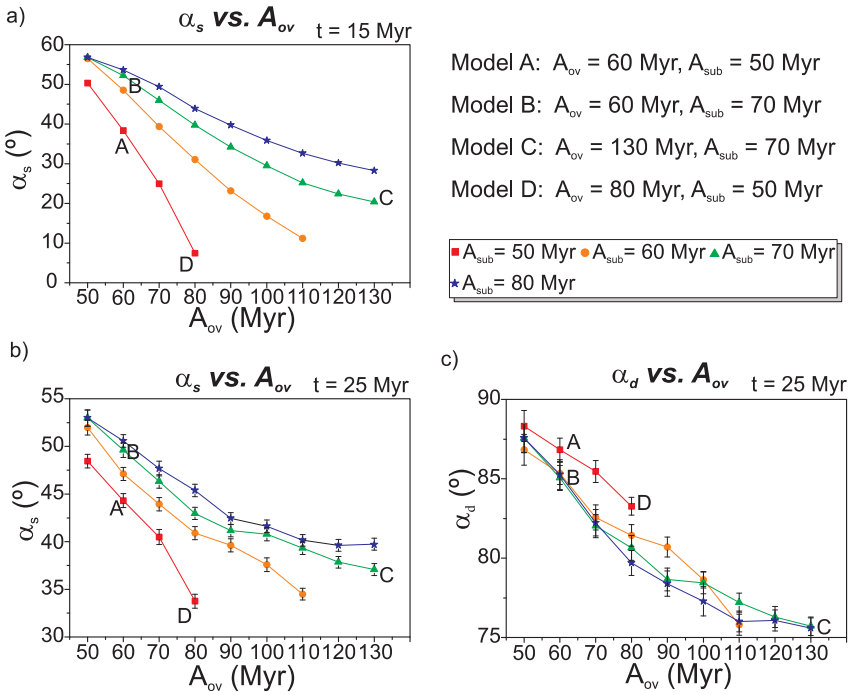

Figure 3.7: Influence of the overriding plate on slab dip. Mean slab dip as a function of the age of the overriding plate for different ages of the subducting plate measured (a) between 100 and 200 km deep (α_s) after 15 Myr of evolution, (b) slab dip α_s measured at depths between 100 and 200 km after 25 Myr and (c) slab dip α_d measured at depths between 300 an 400 km after 25 Myr. Capital letters in the panels indicate models A-D shown in Figure 3.4 and Table 3.2. Note variable scale in vertical axes.

For all the models tested, by 25 Myr, the slab dip increases and the initial differences in slab dip caused by variation in subducting plate age decrease dramatically (Figure 3.7.b and c). This evolution to a steep slab steady-state occurs because as the slab lengthens and the negative buoyancy of the slab increases, the gravitational torque becomes significantly larger than the hydrodynamic torque for all the models (Figure 3.5.b) dominating the dynamics. At this steady-state stage, the thermal state of the subducting plate has little influence on the dip angle at the shallowest portion of the slab (Figure 3.7.b). Moreover, the angle for the deeper portion of the slab does slightly decreases for increasing subducting

plate age (Figure 3.7.c). This can be explained in terms of the higher viscosity of the older subducting plates, as these plates resist bending. Therefore, a higher gravitational torque is required to steepen older subducting plates. These results show that the expected loss of sensitivity of slab dip to subducting plate age for long-term subduction should be taken into account when statistically analyzing slab dip data.

The hydrodynamic suction is greater for lower slab dips (equation (3.7) and Figure 3.1) and therefore young plates, subducting with shallow dips, cause suction torques that are higher than older plates (Figure 3.6.b).

3.3.3. Influence of thermal state of the overriding plate.

To test the influence of the thermal state of the overriding plate we vary the plate age to control its thermal state. Under an old overriding plate the viscosity of the mantle tends to increase due to a more effective cooling. Therefore, as expected from consideration of the hydrodynamic forces, subduction under an older plate results in a higher suction torque around 15-20 Myr (Figure 3.5.c and d and Figure 3.6.b), which leads to a lower slab dip than subduction under a younger plate (Figure 3.4 b vs. c and a vs. d). For young (or hot) overriding plates the viscosity in the deeper part of the lithosphere is relatively low, thus allowing for the thermal erosion of the base of the lithosphere close to the plate boundary. This thermal erosion allows the high strain rate mantle wedge flow to migrate into the shallower regions of the wedge corner, further reducing the viscosity. Through this mechanism the mantle wedge expands into the lithosphere, dramatically reducing the suction torque, leading to steeper subduction.

For a subducting plate age of 60 Myr, by 15 Myr of evolution we obtain a shallow slab dip decrease of about 50º and an increase of the suction torque per slab width of about $3 \cdot 10^{18}$ N, going from a model with an overriding plate age of 50 Myr to a model with an overriding plate age of 110 Myr (solid circles in Figure 3.6.a and in Figure 3.7.a). The influence of the thermal state of the overriding plate is more significant for young subducting plates, as they are less viscous and therefore easier to deform (both by bending and unbending) in response to the net torque. Moreover, as the resulting slab dip is lower for younger subducting plates, the hydrodynamic suction in the mantle wedge increases (equation (3.7) and Figure 3.1), leading to high variations of the suction torque with the age of

the overriding plate (Figure 3.6.b). This leads to a feedback process in which, high hydrodynamic suction leads to low angles, which in turn further increases the suction torque.

After 25 Myr, the influence of the thermal state of the overriding plate diminishes as the hydrodynamic torques from all models are similar (Figure 3.5), but the simulations still produce a maximum difference of almost 20º for the shallowest part of the slab, α_s (Figure 3.7.c) and 15º for the deepest region, α_d (Figure 3.7.d) as a function of overriding plate age. Between 300 and 400 km deep, the slab dip α_d is almost independent of its age. Not only are the differences in slab dip caused by different subducting plate ages negligible, but we also find that the amount that the slab dip decreases for a given increase in the age of the overriding plate is almost identical for all subducting plate ages, about 0.25º/Myr (Figure 3.7.d). Therefore, once again, it is important to take into account the different behavior between short and long-term subduction.

All the simulations presented here show that the influence of the age of the overriding plate is always comparable and even more important than the effect of the age of the subducting plate. After 15 Myr of evolution, increasing the subducting plate age from 50 Myr to 80 Myr leads to increases of αs ranging from 6º (for Aov=50 Myr in Figure 3.7.a) to 36º (for Aov=80 Myr in Figure 3.7.a), whereas if the age of the overriding plate varies from 50 Myr to 80 Myr, the decreases of α_s ranges from 13º (Asub=80 Myr in Figure 3.7.a) to 45º (Asub=50 Myr in Figure 3.7.a). After 25 Myr of evolution, this trend is maintained but with much smaller variations in slab dip. This result highlights the importance of discriminating between different overriding plate thermal states in statistical analysis of slab dip data, to prevent this effect masking that of the slab age. The gravitational torque is less sensitive to variations of either plate's age compared to the hydrodynamic torque (Figure 3.6.a vs. b), and for this reason there is less variability of α_d (mainly controlled by the gravitational torque) than of α_s with plate age.

Although we model an ocean-ocean subduction system, we consider that the qualitative results can be extrapolated for the case of an overriding continental plate. We therefore assume (also on the basis of sensitivity tests to variations in plate thickness) that a thick overriding plate can be approximated as a cold plate

with an older age, which creates a thicker region of high viscosity at the base of the lithosphere. We run some simulations in order to better understand the influence of an overriding plate from a different nature (e.g., an overthickened or a continental overriding plate). First we test the effect of a different plate thickness and we run a model with L=125 km (Figure 3.8). A thickened lithosphere implies having a more viscous mantle wedge, and therefore, a higher suction torque, in some models, this has not much effect (Model B in Figure 3.4.b vs. Model E in Figure 3.8.a), but in others, this can be a critical factor that can trigger the coupling of both plates (Model C in Figure 3.4.c vs. Model F in Figure 3.8.b). However, these models still show the same behavior as models with L=95 km, and older overriding plates lead to a lower slab dip (Model E in Figure 3.8.a vs. Model F in Figure 3.8.b).

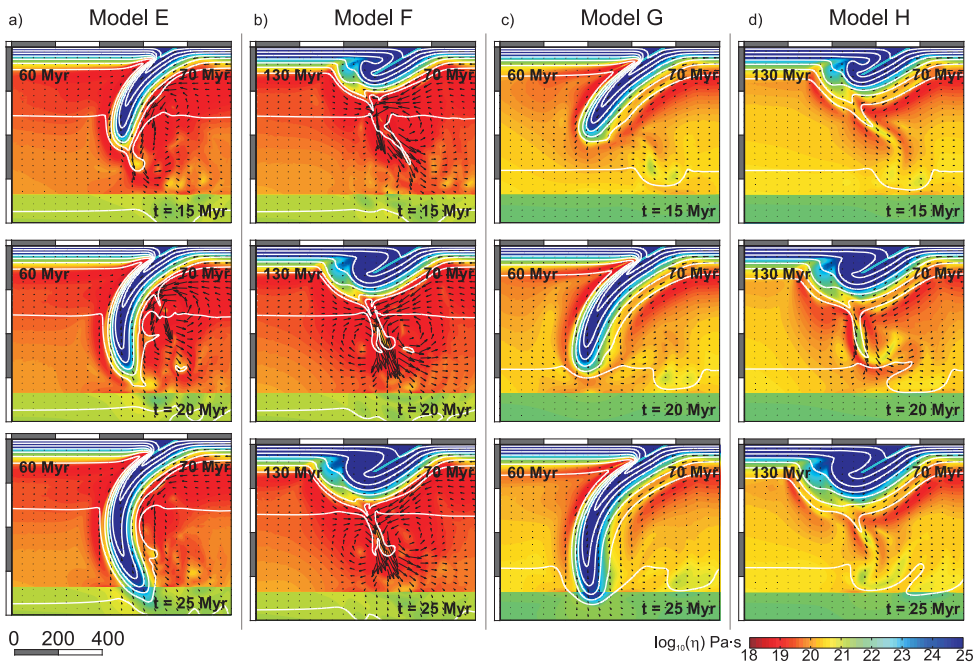

Figure 3.8: Model results at three different evolution times for different ages of the overriding and subducting plates, different plate thickness and different plate base temperature. a) Model E: similar to Model B but with plate thickness L=125 km. b) Model F: similar to Model C but with plate thickness L=125 km. c) Model G: similar to Model B but with plate thickness L=125 km and plate base temperature T_L=1350 ºC. d) Model H: similar to Model C but with plate thickness L=125 km and plate base temperature T_L=1350 ºC. Colors, contours and arrows are the same as in Figure 3.4.

We also run simulations in which both the thickness of the plate and the temperature at the base of the plate are varied. We assume values from the plate

model by Parsons and Sclater (1977) with L=125 km and base temperature of 1350 ºC, being these values often used as representative of the continental lithosphere. In this case, the plates are thicker and colder at the same time, and the resulting viscosity in the mantle wedge is much higher. Therefore, in this models, the resulting slab dip is even lower than for models with L=125 km and a base temperature of 1450º (Model B in Figure 3.4.b vs. Model G in Figure 3.8.c and Model C in Figure 3.4.c vs. Model H in Figure 3.8.d). However, comparing models with the same plate thickness and base temperature but different overriding plate age (Model G in Figure 3.8.c vs. Model H in Figure 3.8.d), once again, colder overriding plates lead to lower slab dips.

However, caution must be taken when extending these results to the case of continental overriding plate, as radiogenic heat production must be taken into account for continental lithosphere.

3.3.4. Subduction styles

Depending on the age of the overriding and subducting plates, the simulations performed in this study show different evolution of the slabs, resulting in different subduction styles (mapped in the diagram shown in Figure 3.9).

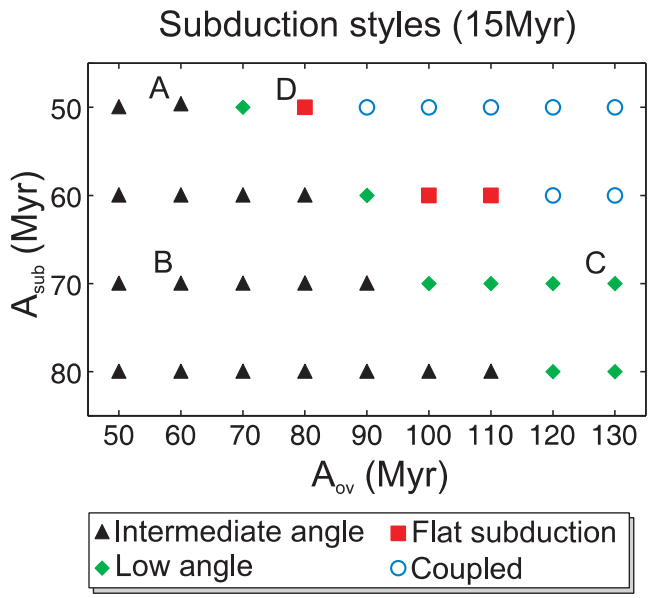

Figure 3.9: Distribution of subduction styles depending on the age of the overriding a subducting plates.

3.3.4.1. High angle subduction.

For old subducting plates (Model B, Figure 3.4.b, Figure 3.10.a and Video 3.B) and, or young overriding plates (red and orange lines in Figure 3.10.c and d) the gravitational torque is always higher than the suction torque (Figure 3.5.b) and therefore the initial slab dip is high. When the initial angle is high, the thermal erosion at the base of the lithosphere is increased causing the migration of the mantle wedge up into the lithosphere. This contributes to enhance the steepening of the subducting plate. For the youngest overriding plates and the oldest subducting plates (red lines in Figure 3.10.a and b) the slab dip decreases slightly with time, around 10º. The slab flattening is caused by the increase of the suction of the shallower portion of the slab due to the cooling of the material in the mantle wedge.

3.3.4.2. Low angle and flat subduction

Simulations with young subducting plates and, or old overriding plates tend to reproduce low slab dips (Model C, Figure 3.4.c and Video 3.C). However, these simulations (blue to green lines in Figure 3.10.c and d) show that this low angle subduction style is transient and slab dip (along both depth ranges) increases significantly from 15 to 25 Myr of evolution, while the slab is sinking and lengthening in the upper mantle and the subduction style evolves to intermediate angle (depths 100-200 km) and high angle (depths 300-400 km) subduction.

An explanation for this is found again studying the torque balance. In contrast with the models that present high angle subduction, at the beginning of the simulation the suction torque is higher than the gravitational torque (Figure 3.5.c and d), which leads to the initial low angle style. As the simulation evolves and the slab length increases, the gravitational torque also increases, which causes the slab dip to increase. A further consequence of the steepening of the slab is that the suction torque decreases (equation (3.7) and Figure 3.1) and the gravitational torque overcomes it. At about 25 Myr, the torque balance reaches steady state and the slab dip remains nearly constant during the rest of the modeled evolution.

For the youngest subducting plates and old overriding plates (Model D, Figure 3.4.d, Figure 3.5.d and Video 3.D) not only is the angle of subduction very low, but the slab reverses its curvature to flatten at ~100 km deep and advances

sub-horizontally for hundreds of kilometers, due to the fact that during the early stages of evolution the suction torque is much higher than the gravitational torque (Figure 3.5.d). A thin layer of low viscosity develops between the overriding and the subducting plates, which is maintained by the high strain rate between them and the non-linear rheology. This layer decouples the plates from one another allowing for the formation of long segments of flat subduction. It is worthwhile remarking that we are able to produce these long segments of flat subduction without imposing either a trenchward velocity of the overriding plate or density anomalies on the subducting plate. These results are in very good agreement with those found by Roda et al. (2011), who tested the effects of overriding plate thickness. Taking into account that the model set-up, thermal and rheological structures assumed in both studies are substantially different, the consistency in qualitative results strengthens the robustness of the conclusion about the important role played by the overriding plate on controlling slab dip.

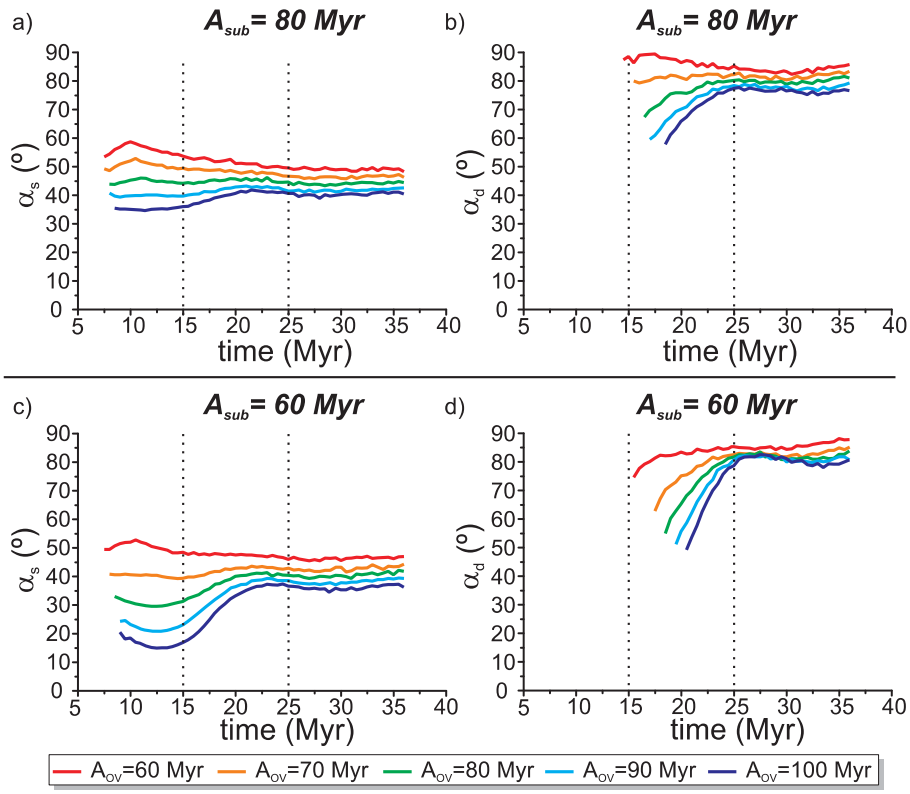

Figure 3.10: Time evolution of the mean slab dip for different models. (a, b) measured between 100 and 200 km (α_s) and (c, d) between 300 and 400 km deep (α_d). Comparison of the evolution for different overriding plate age at a constant subducting plate age of (a and b) 80 Myr and (c and d) 60 Myr. Colors indicate different ages of the overriding plates, as described in the legend.

After the formation of long flat segments, the evolution of slabs can follow two different paths. If the increase of the gravitational torque is high enough, the slab overcomes the suction torque and peels away from the overriding plate, increasing its angle, but it still remains relatively shallow-dipping for the shallowest portion of the slab (Model D, Figure 3.4.d and Video 3.D). The lower slab dip causes the suction torque to be higher than in other models with younger overriding plates, thus, the gravitational torque overcomes the suction torque in a later stage (Figure 3.5.d vs. Figure 3.5.c), slightly delaying the sudden increase of the subduction angle. On the other hand, if the hydrodynamic torque always overcomes the gravitational torque, the low viscosity channel of the plate boundary closes up, coupling both plates and hindering subduction (Model I in Figure 3.11.b and Video 3.I; A_{sub}=40 Myr and A_{ov}=60 Myr). This subduction style was named "coupled" by Billen and Hirth (2005) and occurred only in their models with Newtonian rheology and an old (80 Myr) overriding plate (although they did not consider variations in the overriding plate age).

Our results do not necessarily imply that long-living flat subduction is not possible but, with the particular setup used here (fixed trench, absence of anomalously buoyant subducting material), when the hydrodynamic suction is strong enough to produce a flat slab segment, it occurs that both plates end up being coupled. In time-dependent models, an imposed wet, and therefore weak, wedge corner counteracts the increase in viscosity owing to cooling of the wedge nose (*Kincaid and Sacks*, 1997) and maintains the separation of the subducting and overriding plate (*Cízcová et al.*, 2007). Therefore, with this model setup, an additional mechanism to maintain the plates decoupled even for strong hydrodynamic suction (e.g., dehydration, melting processes, a low viscosity layer representing oceanic crust) is required to obtain non coupled flat subduction over longer periods of time. Including a low viscosity crust in the subducting plate would avoid this coupling, but as discussed before it would introduce a complexity (overriding plate and trench motion) that prevents the effect of thermal state of both plates from being isolated.

3.3.4.3. Laterally Varying Overriding Plate Age

Another test case we consider is the effect of laterally-varying age of the overriding plate with distance from the trench (Figure 3.11). Model J (Figure 3.11.c) has a subducting plate 50 Myr old and an overriding plate 80 Myr (from 0 to 200

km to the trench) that increases its age to 150 Myr (>200 km from the trench). This model can be compared with Model D (A_{sub}=50 Myr and A_{ov}=80 Myr). While Model D presented a transient flat subduction period followed by the steepening of the slab (see section 3.3.4.1), in this case, when the slab reaches the older portion of the overriding plate, the hydrodynamic suction increases and both plates end up coupled (Figure 3.11.a and c).

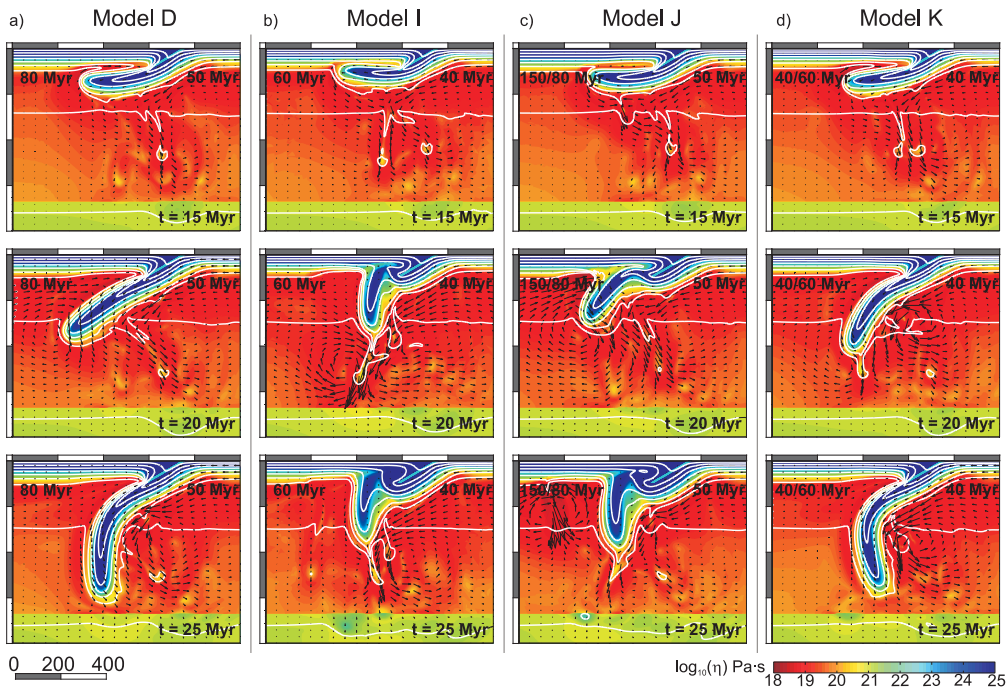

Figure 3.11: Model results at three different evolution times for different uniform and non uniform overriding plates (Table 3.2). a) Model D: subducting plate of 50 Myr and an overriding plate of 80 Myr (already shown in Figure 3.4.d). b) Model I: subducting plate age of 40 Myr and an overriding plate with uniform age of 60 Myr. c) Model J: subducting plate of 50 Myr and an overriding plate that changes age from 80 Myr (0–200 km from trench) to 150 Myr (> 200 km from trench), Model J. d) Model K: subducting plate age of 40 Myr and an overriding plate that changes age from 60 Myr (0–200 km from trench) to 40 Myr (> 200 km from trench). Colors, contours and arrows are the same as in Figure 3.4.

On the contrary, the overriding plate in Model K (Figure 3.11.d) becomes younger 200 km from the trench and its age decreases from 60 Myr (0–200 km from the trench) to 40 Myr (> 200 km from the trench). This model can be compared with Model I (A_{sub}=40 Myr and A_{ov} = 60 Myr). Whereas Model I is an example of coupled subduction (see section 3.3.4.1 and Figure 3.11.b), in Model K, when the slab reaches the portion of the overriding plate where the viscosity is lower, the suction torque starts decreasing, causing the gravitational torque to

become dominant and the slab to become steeper (Figure 3.11.d). In this situation the slab evolves to a profile with a long, low angle segment, followed by a steep segment. This simulation provides a possible explanation for the steep deepest portion of the slab in southern Mexico (see section 3.4)

The sudden changes of overriding plate age imposed in this section can also be considered as a modeling artifact intended to account for the first order effects of the proximity of cratons (cold lithosphere) or rift basins (hot lithosphere).

3.3.4.4. Role of plate coupling and slab strength

We perform a systematic analysis of the role of both plate ages. However, the characteristics of the modeled plate boundary and the rheology are also expected to have a significant role on the subduction style. In this section, we do not intend to systematically analyze the role of plate coupling or slab strength on subduction dynamics, which has been done elsewhere (e.g., *Billen and Hirth*, 2005, 2007; *de Franco et al.*, 2007), but to check whether the predicted influence of the upper plate thermal state is a general result, not restricted to a particular choice of parameters.

For this purpose we conduct an additional set of models where the coupling between both plates at the shear zone is decreased by reducing the maximum viscosity of the shear zone ($\eta_b=10^{21}$) and the maximum overall viscosity cut-off ($\eta_{max}=10^{24}$). In these weaker models (and with a weaker shear zone) the slab dip is steeper (for the same plate ages as in the models shown above) but there is still a strong influence of the thermal state of the overriding plate on the geometry of subduction (Models L-N, shown in Figure 3.12), especially for young subducting plates.

The previous models, in which the slab was stronger, showed a gradual variation of the slab dip with the age of the overriding and subducting plates. In, this case the variation of the slab dip with the overriding plate age is only gradual for the shallowest portion of the slab (between 100 and 200 km) and two distinct styles are reproduced. If the overriding plate is old (Model L in Figure 3.12.a), the hydrodynamic suction is so high that both plates become completely coupled and the plate cannot subduct. On the contrary, for younger overriding plates (Model M in Figure 3.12.b) the mean dip angle computed between 300 and 400 km is

almost vertical. In these simulations, flat slab segments are also reproduced (Model N in Figure 3.12.c), but have a shorter duration and are much shorter in length because the gravitational torque is more efficient in steepening weaker slabs, which are more susceptible to bend. Unlike a rigid slab (e.g., *Stevenson and Turner*, 1977) flattening of the slab occurs because it is weak enough to deform in response to the changes in hydrodynamic stresses, while at the same time strong enough to support a substantial portion of its own weight. If the slab is very weak, it will either sink vertically or couple to the upper plate (if the hydrodymanic torque is strong enough), whereas if it is very strong the hydrodynamic stresses will not be able to deform it.

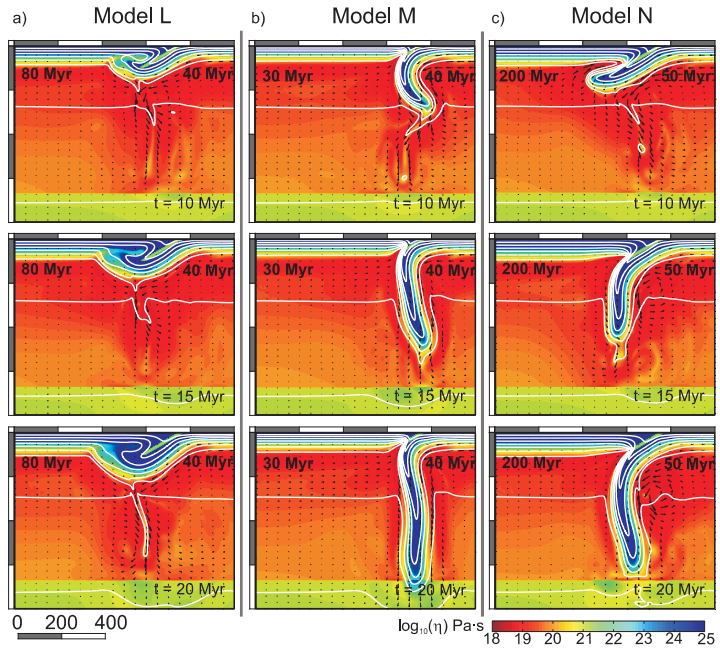

Figure 3.12: Models results considering a weaker rheology ($\eta_b = 10^{21}\ Pa{\cdot}s$ and $\eta_{max} = 10^{24} Pa{\cdot}s$) than in the reference Model A. Results at three different evolution times for different ages of the overriding and subducting plates (Table 3.2). a) Model L: coupled subduction. b) Model M: high-angle subduction. c) Model N: flat subduction. Colors, contours and arrows are the same as in Figure 3.4.

Another important factor influencing plate coupling is the angle imposed for the shear zone. We run several models in which we reduce the shear zone angle (θ_{sz}) to values of 25º, 20º and 15º, and obtain the same qualitative results, although these lower values of θ_{sz} promote the occurrence of shallow dip and flat subduction due to the increased suction torque.

We test the effect of subduction velocity. Equation (3.7) predicts a higher hydrodynamic suction for higher subduction velocities. However, having a high subduction velocity implies having a great deformation over the top of the slab and the effect of the viscosity reduction due to that the increased strain rate becomes predominant for sufficiently high subduction velocity values. For a velocity of 7.5 $cm \cdot yr^{-1}$ (models O and P, Figure 3.13), the induced corner flow is stronger and the viscosity is reduced, leading to steeper slabs (Model D vs. O) and preventing coupling (Model E vs. P). If on the contrary a slower subduction velocity (2.5 $cm \cdot yr^{-1}$) is used (models Q and R, Figure 3.13) the corner flow induced on the mantle wedge is decreased and therefore, the strain rate on that region is reduced. This leads to an increased viscosity that increases the coupling between the plates, resulting in decreased slab dips (Model B vs. Q) or even coupled subduction (Model C vs. R).

These tests show that, as expected, subduction style is also sensitive to the slab strength and to the amount of coupling at the plate boundary. We infer that flat subduction style is favored by moderate plate coupling and by a relatively stiff slab, however constraining the exact value of these parameters requires further study using fully-dynamic 3D models. The 2D approach used here necessarily requires a kinematic boundary condition to reproduce flat and low angle subduction styles.

3.4. Comparison to Cocos plate subduction

To illustrate the influence of the thermal state of the overriding plate on slab dip, we discuss the variations of slab dip under southwestern Mexico and northern Central America (Figure 3.14) and compare these variations to the modeling predictions. The subduction angle of the young (15–30 Myr old) Cocos plate under the Caribbean Plate deviates from the expected trend and is anomalously high for its age (Figure 1.3.a, COST and Figure 1.3.b, Central America). Moreover, the variability of the slab dip is very large, from 60 to 90 degrees in the deepest region, along this subduction zone, even for similar ages of the subducting plate (Figure 3.14.b; from *Álvarez-Gómez,* 2009). The slab profiles, from northwest to southeast, show flat subduction under southwestern Mexico (cross section A; see also e.g.,*Pardo and Suarez*, 1995) low angle subduction (cross sections B-D) and high angle subduction (cross sections E-K). It is worthwhile

noting the absence of a volcanic arc in cross-sections A-D. Several explanations can be given to explain this variability:

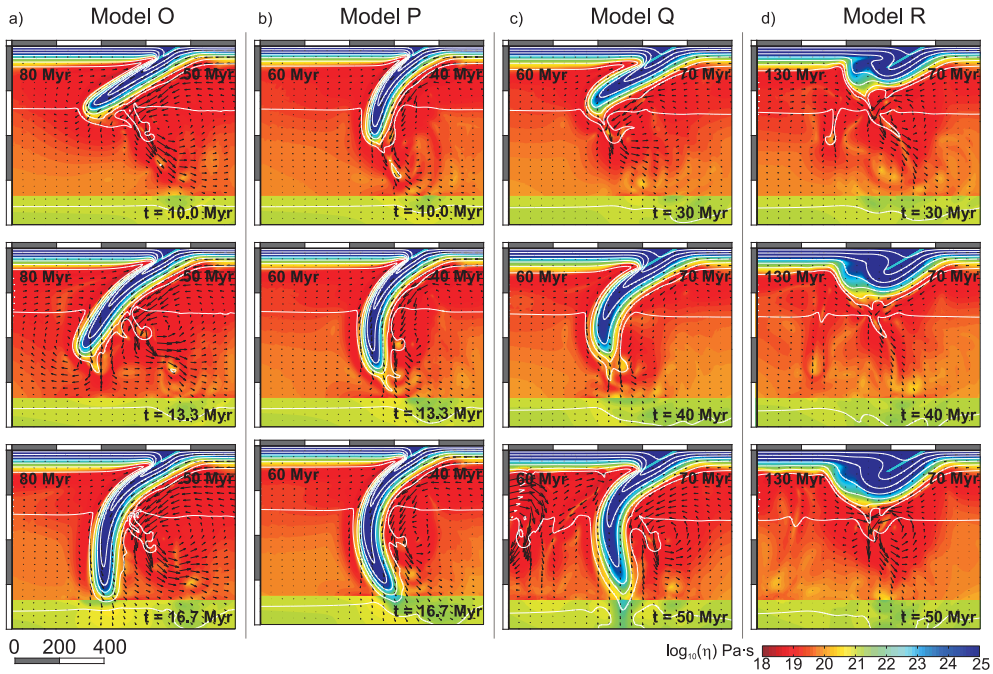

Figure 3.13: Model results at three different evolution times for different subduction velocities. a) Model O: similar to Model D but with subduction velocity u_s=7.5 cm·yr^{-1}. b) Model P: similar to Model I but with subduction velocity u_s=7.5 cm·yr^{-1}. c) Model Q: similar to Model B but with subduction velocity u_s=2.5 cm·yr^{-1}. d) Model R: similar to Model C but with subduction velocity u_s=2.5 cm·yr^{-1}. Colors, contours and arrows are the same as in Figure 3.4.

(1) High slab dips have been explained as a result of the retreating motion of the overriding plate. This explanation is not suitable for the subduction under the Caribbean plate as this plate moves trenchward (*Grip and Gordon*, 2002), which favors flat subduction (e.g., *van Hunen et al.*, 2004).

(2) Another factor favoring steep dip is the increased toroidal flow around the edges of the slab. However, on Figure 1.3.c and d, data from near-edge slabs from the studies by Lallemand et al. (2005) and Cruciani et al. (2005) have already been removed and this 'anomalous' steep dip is still found in both studies. Moreover cross sections E-I are far from edges and show high dip (Figure 3.14.a).

(3) Flat subduction has been explained in terms of the presence of anomalously buoyant material on the subducting plate (e.g., *Gutscher et al.*, 2000b; *van Hunen et al.*, 2004), but the only buoyant material in this area is the

Tehuantepec Ridge, and a single, small, ridge is not sufficient to produce flat subduction, therefore, this is not a plausible explanation (*Gerya et al.*, 2009).

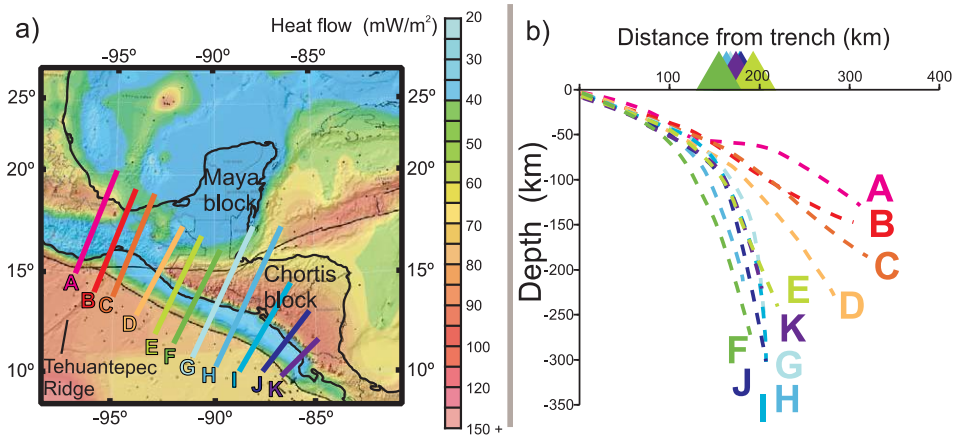

Figure 3.14: Heat flow and slab dip for the Cocos plate section of the Central American Trench. a) Surface heat flow in Central America (Blackwell and Richards, 2004) (*Blackwell and Richards*, 2004) and location of cross sections shown in b). b) Comparison between the slab dip profiles traced along the upper limits of the seismicity in the sections shown in a) (from Álvarez-Gómez (2009), using data from the NEIC [2007] seismic catalog). Triangles show the location of the volcanic arc for profiles E-K (volcanic arc is missing for profiles A-D).

Here we provide an alternative, plausible explanation for the slab dip variability of the Cocos plate in terms of the variation of the thermal structure of the overriding plates and its relation with the hydrodynamic suction torque.

The Maya (Yucatan) block of the North America plate is known to be of continental origin and was rotated to reach its current location after the opening of the Gulf of Mexico during the Late Jurassic (*Marton and Buffler*, 1994). The Chortis block (Honduras, Nicaragua and Guatemala) of the Caribbean plate has been traditionally regarded as a Precambrian–Paleozoic continental nucleus previously attached to South-western Mexico. This terrain was translated from west to east and rotated counter-clockwise during the Cenozoic (*Pindell and Barrett*, 1990). While the Maya block is homogeneous (*Dickinson and Lawton*, 2001), the Chortis block is divided into different tectonic terrains including normal continental terrains, attenuated continental crust and oceanic terrains (*Rogers*, 2003). Therefore, while the Maya block is part of a thick continental plate, the Chortis block is either formed of oceanic lithosphere or thinned continental lithosphere. This structural variation is reflected in the surface heat flow map of

the area, which exhibits much higher heat flow under the Chortis block compared to the Maya block (Figure 3.14.a) and in lithospheric thickness maps (e.g., *Artemieva*, 2006), which show thickness of 50-100 km beneath the Chortis block compared to 100-125 km beneath the Maya block. Moreover, this transition corresponds to the North America-Caribbean plate boundary.

The abrupt change in the surface heat flow between Maya block and the Chortis block reveals the contrast in thermal state between both plates, which involves a strong variation of the viscosity at the base of both plates close to the plate boundary interface at the mantle wedge. This variation in thermal state corresponds to a transition from shallow slab dip in sections A-C to more steeply-dipping profiles in sections D-K. On the basis of our modeling, we suggest that flat subduction of the Cocos plate under the colder Maya block is likely related to the higher viscosity close to the base of the overriding plate (similar to Model D in Figure 3.4.d and Figure 3.5.d), while subduction under the warmer Chortis block is much steeper due to reduced suction torque associated with a lower viscosity at the base of the upper plate (similar to Model A in Figure 3.4.a and Figure 3.5.a).

One may argue that this is a circular argument, as the observed variation in heat flow could simply reflect the current geometry of the slabs, with shallow-dipping slabs insulating the base of the lithosphere and steeply-dipping slabs allowing for active mantle-wedge flow and volcanism, leading to higher surface heat flow. First, the wavelength of the high surface heat flow in the Chortis block is too long to be related only to volcanism. More importantly, the differing tectonic history and terrane types of the Maya and Chortis blocks, and lithosphere thickness observations indicate that the present day heat flow reflects the pre-existing structure of the subduction zone, which may have been reinforced by the subsequent differing evolution of the slab segments under each region.

Finally, it is important to note that while subduction has been long-lived along the Central America Trench, there is evidence for recent detachment of the deeper portion of the slab (*Rogers et al.*, 2002), which would make the shallow portion of the slab more sensitive to variations of hydrodynamic forces. This observation is therefore also consistent with the model results, which show that

episodes of flat slab subduction occur early in subduction when the slab has not yet entered the lower mantle.

3.5. Conclusions

In order to test the influence of the thermal state of the overriding and subducting plates on the dynamics and geometry of subduction, we develop a systematic study in which we vary separately the age of both plates. Our results indicate that, as expected from consideration of the gravitational torque, old subducting plates start subducting with a higher angle than young plates, due to higher negative buoyancy. However, the influence of the thermal state of the subducting lithosphere is only significant for the first stages of subduction, while the slab sinks into the upper mantle, and diminishes with time as slab geometry tends to reach steady state.

In contrast, the influence of thermal state of the overriding plate on slab dip can have a noticeable effect on slab dip even for long evolution times, as colder overriding plates impart a higher viscosity at the base of the plate, and thus a higher hydrodynamic suction torque. Therefore, plates subducting underneath cold overriding plates are predicted to subduct with lower slab dip, and this effect is predicted to be more important than that of the subducting lithosphere age.

Finally, with this simple modeling, varying only the age of the subducting and overriding plates we are able to reproduce a wide range of slab geometries and different styles of subduction, including flat, low-angle and high-angle subduction.

We compare our modeling predictions, in qualitative terms, with the Cocos slab dip variability beneath Central America. We provide a plausible explanation for this variability in terms of the change of the thermal state of the overriding plates, with flat subduction occurring under the cold lithosphere of the Maya block of North America and steep subduction under the warmer lithosphere of the Chortis block of the Caribbean plate.

4

EFFECT OF THE HORIZONTAL MANTLE FLOW

4.1. Introduction

The simple scenario we have presented in the previous section is appropriate to explain slab dip variability in many cases, but for some subduction zones it is sometimes at odds with observations that provide noticeable exceptions, such as the steep subduction of a young slab along the Sandwich subduction zone or the shallow dip subduction of an old slab in the Indonesian subduction zone (Figure 1.3). Among other factors (e.g., trench motion, slab stagnation in the upper-lower mantle boundary), the relative motion between the plates and underlying mantle has been proposed to influence the subduction dynamics and its tectonic and magmatic consequences. Some authors (e.g., *Doglioni et al.*, 1999) propose that geological and geophysical observations indicate that the polarity of subduction zones and the relative motion of the subducting plate with respect to the mantle strongly control the characteristics of subduction-related orogens and slab dips. Riguzzi et al. (2009) compiled slab dips measured along cross-sections perpendicular to the trench of most subduction zones and found a clear asymmetry, with west dipping slabs being steeper than east dipping slabs (Figure 4.1).

Assuming that hotspots can be taken as a fixed reference frame, hotspot tracks indicate a relative motion between lithosphere and the underlying mantle, with the asthenosphere acting as a detachment layer due to its low viscosity. Several researchers proposed a global or net westward drift of the lithosphere relative to the mantle (e.g., *Bostrom*, 1971; *Gripp and Gordon*, 2002; *Cuffaro and Jurdy*, 2006). Variable average rates have been proposed in the literature for the westward drift, because the amplitudes of this value strongly depend on inversion choices (e.g., Euler poles for slow-moving plates, such as Africa, and hot spot selection, *Ricard et al.*, 1991; *O'Neil et al.*, 2005). A value of 2 $cm \cdot yr^{-1}$ was proposed by Ricard et al. (1991), whereas a value of 4.9 $cm \cdot yr^{-1}$ was suggested in the frame of Model HS3 by Gripp and Gordon (2002). However, according to Model SB04 (*Steinberger et al.*, 2004), if hotspots are allowed to move with respect to each other, the amount of net rotation is about 38% of that predicted by HS3. Amounts of net rotation of about 50% of HS3 are consistent with the observed azimuthal seismic anisotropy (*Becker*, 2008).

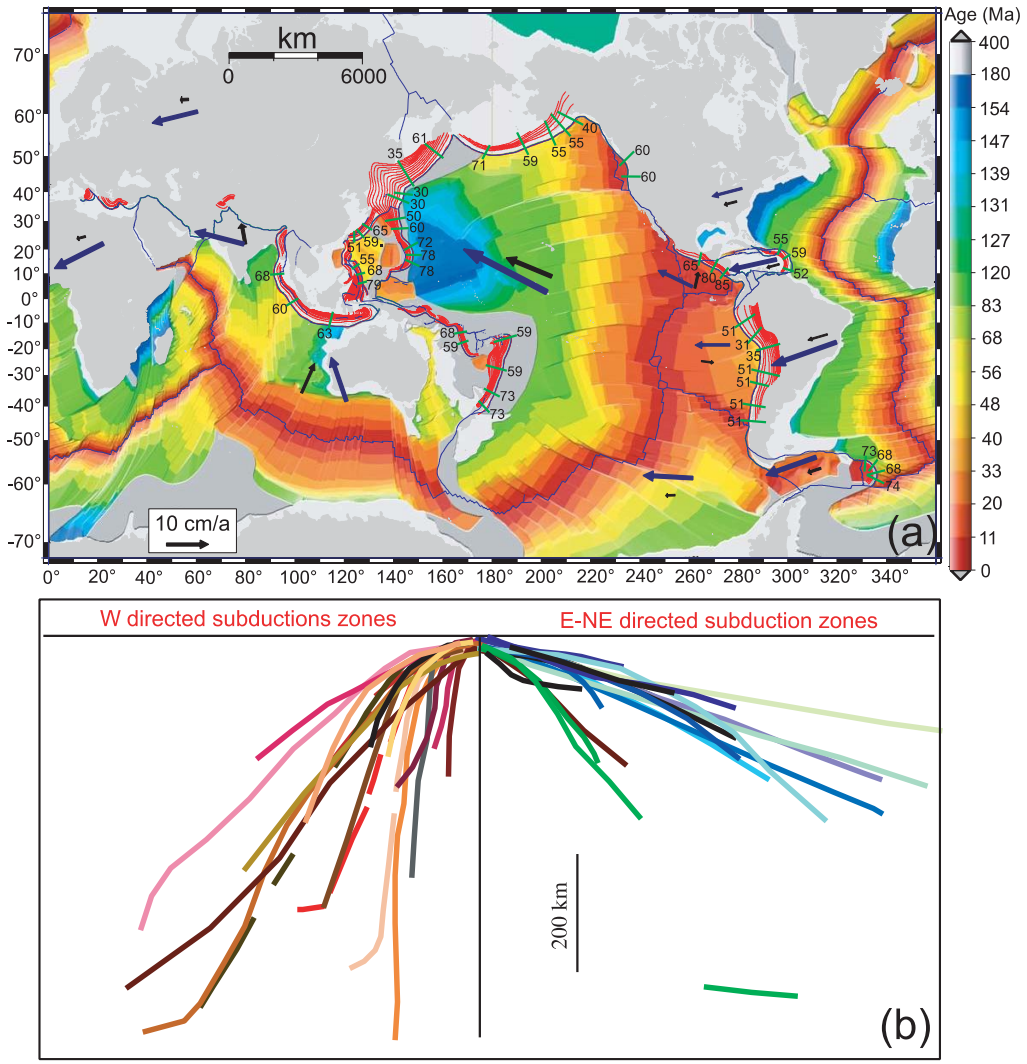

Figure 4.1: Plate velocities for different reference frames. a) Plate ages (*Müller et al.*, 1997), plate boundaries and the geometry (red isolines of the top of the slabs are drawn every 100 km) of slabs (*Gudmundsson and Sambridge*, 1998) are shown. The black numbers indicate the dip of slabs in the 200-250 km deep range measured by Cruciani et al. (2005) along the traces indicated by the green lines. The black and blue arrows show the absolute motions of the major plates referred to two hotspot reference frames (*Grip and Gordon*, 2002; *Cuffaro and Doglioni*, 2007, respectively). b) Compilation of slab geometries along trench-perpendicular traces. Notice that west dipping slabs are steeper than east and northeast dipping slabs. The geometries are taken from Riguzzi et al. (2009), to which the reader is referred for the localization of the section traces.

However, much larger values have been recently proposed, on the basis of a global kinematic model based both on geodetic and geological constraints, with westward drift rates as high as 13.4 cm·yr^{-1} (*Crespi et al.*, 2007). A debate recently

arose regarding whether hotspots are deep or shallow-seated features (*Foulger*, 2005). If hotspots are assumed to be of deep origin, some plates do move eastward with respect to the mantle (e.g., *Grip and Gordon*, 2002; black arrows in Figure 4.1). If they are shallow sourced, then all the plates move westward (e.g., *Cuffaro and Doglioni*, 2007; blue arrows in Figure 4.1). The definition of a proper reference frame and the consequent calculation of plate motions are beyond the scope of this work. However, it is clear that, owing to the dip direction of the slab with respect to the absolute plate motion, slabs may either oppose or accompany the relative mantle flow.

According to Doglioni et al. (1999), other features, often related with slab dip, also show this East-West asymmetry (Figure 4.2): (1) East-directed subduction zones (E-DSZs) show on average higher slab dips than West-directed subduction zones (W-DSZs) (Figure 4.1.b); (2) E-DSZs show on average high heat flow values whereas W-DSZs show a pattern that combines high surface it flow (at the back-arc basin) and low surface heat flow (at the trench); (3) Orogens in E-DSZs show a higher elevation than in W-DSZs; (4) E- and W-DSZs are associated with double and single vergence of the accretionary prism respectively; (5) EDSZs present two shallow foredeeps while W-DSZs zones show a single deep trench; (6) the crust in thrust belts is thicker in E-DSZs; (7) the different kinematic systems generate different metamorphic rocks due to the different pressure-temperature-time (PTt) paths; (8) a higher topography, higher rate of uplift and lower gravity anomalies are found at E-DSZs; (9) W-DSZs show a more developed back-arc basin due to the roll-back of the steeper slab; (10) E-DSZs and W-DSZs show important petrologic and geochemical differences in the subduction-related magmatism.

However, no consensus has been reached about the relationship between subduction polarity and slab dip (e.g., Cruciani et al., 2005 vs. Lallemand et al., 2005; Schellart 2007, 2009 vs. Doglioni 2009). The controversy is due to some major problems: (1) the data sets used to measure actual dips of slabs are not uniform; (2) the effects of absolute plate motions on slab dips are difficult to deconvolve from the other factors described above; (3) no agreement has been reached on the reference frame (and therefore on the resulting velocities). A further source of complication is the fact that the simple kinematic models discussed above, displaying the net-rotation of the lithosphere with respect to the

mantle could be complicated by other processes, e.g., net-rotation associated currents induced, for example, by continental keels, (*Zhong*, 2001; *Becker*, 2006); or general return flow, which is not necessarily connected to net rotations (*Hager and O'Connell*, 1981). In other words, regional flow could be significantly different from the above described global mantle flow.

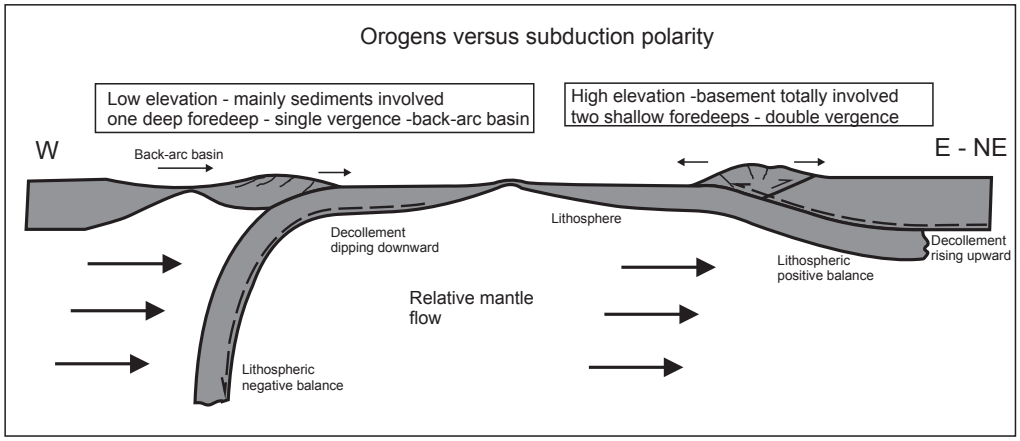

Figure 4.2: Differences between West- and East-directed subduction zones according to Doglioni et al. (1999)

The potential influence of the relative motion of the lithosphere with respect to the mantle has not been extensively studied, excluding some 2D numerical modeling and some laboratory experiments. Olbertz et al. (1997) used numerical modeling to impose a mantle flow and analyzed the influence of trench migration (with respect to the mantle) in the geometry of the slab using a linear viscosity (only temperature dependent). They showed that mantle flow in the sense of subduction decreases the slab dip and can even prevent penetration into the lower mantle. Winder and Peacock (2001) studied the forces exerted in a slab under the influence of an imposed mantle flow. These authors showed that a regional mantle flow produces very efficient torque force that mostly affects the lower surface of the slab, but does not affect the suction in the mantle wedge. Their models however, have several downsides as they do not evolve with time, assume the slab is rigid (infinite viscosity), with a fixed constant dip and the viscosity of the mantle is only depth dependent. Boutelier and Cruden (2008) developed pseudo 2D analog models (only 2D flow allowed within the model box) in which they showed that in presence of a horizontal mantle flow, the slab geometry, the subduction dynamics and the compression regime of the

overriding plate were greatly affected. Using 2D viscoçelastic plane strain models, Carminati and Petricca (2010) showed that, in an elastic slab, downdip compression in the subducting slab is enhanced by mantle flow in the opposite sense of subduction, whereas downdip extension is favored by mantle flow in the same sense as subduction.

The purpose of this chapter is to perform a systematic analysis of the effect of a hypothetical mantle flow (either global or regional) on slab dip and long term evolution of subduction. Compared to previous work, in particular evolutive numerical modeling by Olbertz et al. (1997), we use here a more realistic non-linear rheology, an improved grid resolution (allowing for much higher viscosity contrasts), a more realistic implementation of the plate boundary and explore different mantle flow velocities. In the next sections I show the results and conclusions derived from evolutive 2D models in which we impose a horizontal mantle flow either in the same or in the opposite sense of subduction. This imposed mantle flow can either be understood as a global relative motion of the mantle with respect to the lithosphere or as a regional mantle flow induced by different factors. Rather than addressing a specific region, we investigate the physics of the process varying calculation parameters (such as the sense and magnitude of mantle relative velocity and the slab strength) and show that indeed the mantle flow significantly influences the slab geometry and the long-term evolution of subduction.

4.2. Model Setup

These models are solved using Comsol Multiphysics and assuming the same governing equations and numerical methods explained in Chapter 3. The 2D approach, the geometry of the problem, the initial temperature distribution and the rheology are also similar to the model explained in the same chapter. The boundary conditions are slightly different from the ones explained in previous chapter. In order to reproduce mantle flow in the sublithospheric upper mantle, either in the same or the opposite sense of subduction, an inlet velocity (u_{MF}) is applied at one of the lateral boundaries, from 95 to 670 km deep, while the same outlet flow is imposed on the opposite boundary. These boundaries are far away from the subduction zone to avoid boundary effects. Different values of the mantle flow are used: 2 cm·yr^{-1} (as sugested by *Ricard et al.*, 1991), 4 cm·yr^{-1}

(compatible with the velocity suggested in the frame of Model HS3 by *Grip and Gordon*, 2002) and 8 cm·yr^{-1} (more similar to values from *Crespi et al.*, 2007). A *free slip* condition is applied to the bottom boundary (Figure 4.3). A velocity of subduction u_s=5 cm·yr^{-1} is applied on the top of subducting plate, whereas the overriding plate is fixed.

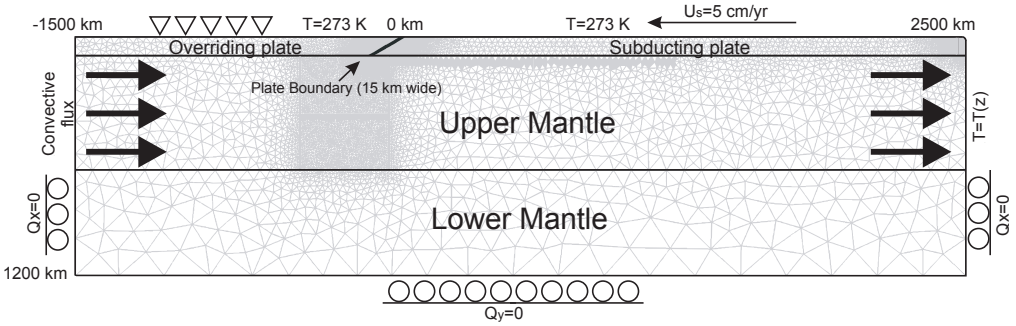

Figure 4.3: Schematic representation of the modeled 2D vertical cross section showing the finite element mesh and boundary conditions. Thick arrows represent the kinematic boundary condition to impose mantle flow.

As in Chapter 3 the assumptions of a fixed trench and 2D geometry make this modeling suitable for areas far away from slab edges in wide subduction zones, as these areas undergo little trench motion (*Schellart et al.*, 2007).

We have checked that the kinematic conditions applied to simulate mantle flow do not produce a pressure singularity in the corner of the mantle wedge. To avoid the known pressure singularity at the corner formed by the top of the slab and the base of the upper plate (*Batchelor*, 1967) some authors use a curved boundary there (*Richter and McKenzie*, 1978; *Winder and Peacock*, 2001). This singularity does not occur in this modeling because instead of introducing a prescribed rigid slab, the plates are not assumed here to be rigid, and the slab reacts dynamically in response to the force and momentum balance.

4.3. Results

Once again, we focus on the geometry of the slab, in particular on the angle of subduction. Assuming that slab dip will vary significantly with depth, I present the results in the same depth ranges as in previous chapters: α_s is the mean shallow angle, measured between 100 and 200 km, and α_d is the mean deep angle measured between 300 and 400 km.

4.3.1. Reference model

To compare the resulting slab dips with and without mantle flow, the reference model is Model A (overriding plate of 50 Myr and subduction plate of 60 Myr) described on section 3.3.1. To compare the variations of the slab geometry with the sense and intensity of the mantle flow we compute the difference between the slab dip for a given simulation, alpha, and the slab dip of the reference model α_A. Henceforth this difference will be referred to as *angular deviation* $\Delta\alpha=\alpha - \alpha_A$. The angular deviation changes with depth, therefore we compute it between 100 and 200 km ($\Delta\alpha_s$) and between 300 and 400 km ($\Delta\alpha_d$).

4.3.2. Influence of mantle flow on slab dip.

To test the influence of the mantle flow on the slab dip we run simulations with two different velocities of the imposed horizontal flow (2 and 4 cm·yr^{-1}) and two different orientations (Figure 4.4). From now on we will refer to the mantle flow opposing the sense of subduction as *positive mantle flow* (in the positive sense of horizontal axis in our setup) and to the mantle flowing to the same direction of subduction as *negative mantle flow* (in the negative sense of horizontal axis).

During the few first million years there are no great differences in the evolution between the reference model and the simulations with an imposed mantle flow (top panels in Figure 4.4 and Figure 4.5.a). Due to the increased viscosity of the lower mantle, the material finds more resistance to flow through the lower mantle, so it travels mostly in the upper mantle. As the simulations evolve and the tip of the slab approaches the lower mantle, the room for the material to flow through the upper mantle is reduced and the flow gets channeled between the tip of the slab and the top of the lower mantle. Due to the conservation of mass, the velocity around the tip of the slab increases (middle panels in Figure 4.4). The increased velocity around the tip of the slab is crucial as the torque exerted by the mantle flow becomes concentrated in this region, controlling the geometry of the slab. Also, provided that the length of the slab increases with time, the pressure exerted by the mantle flow leads to a greater torque. Consequently, the angular difference increases with time (Figure 4.4 and Figure 4.5.a and b): at 20 Myr $\Delta\alpha_s$ ranges between -3.5º and 1º and $\Delta\alpha_d$ between -6.5º and 2º, whereas at 30 Myr values of $\Delta\alpha_s$ ranges between -7º and

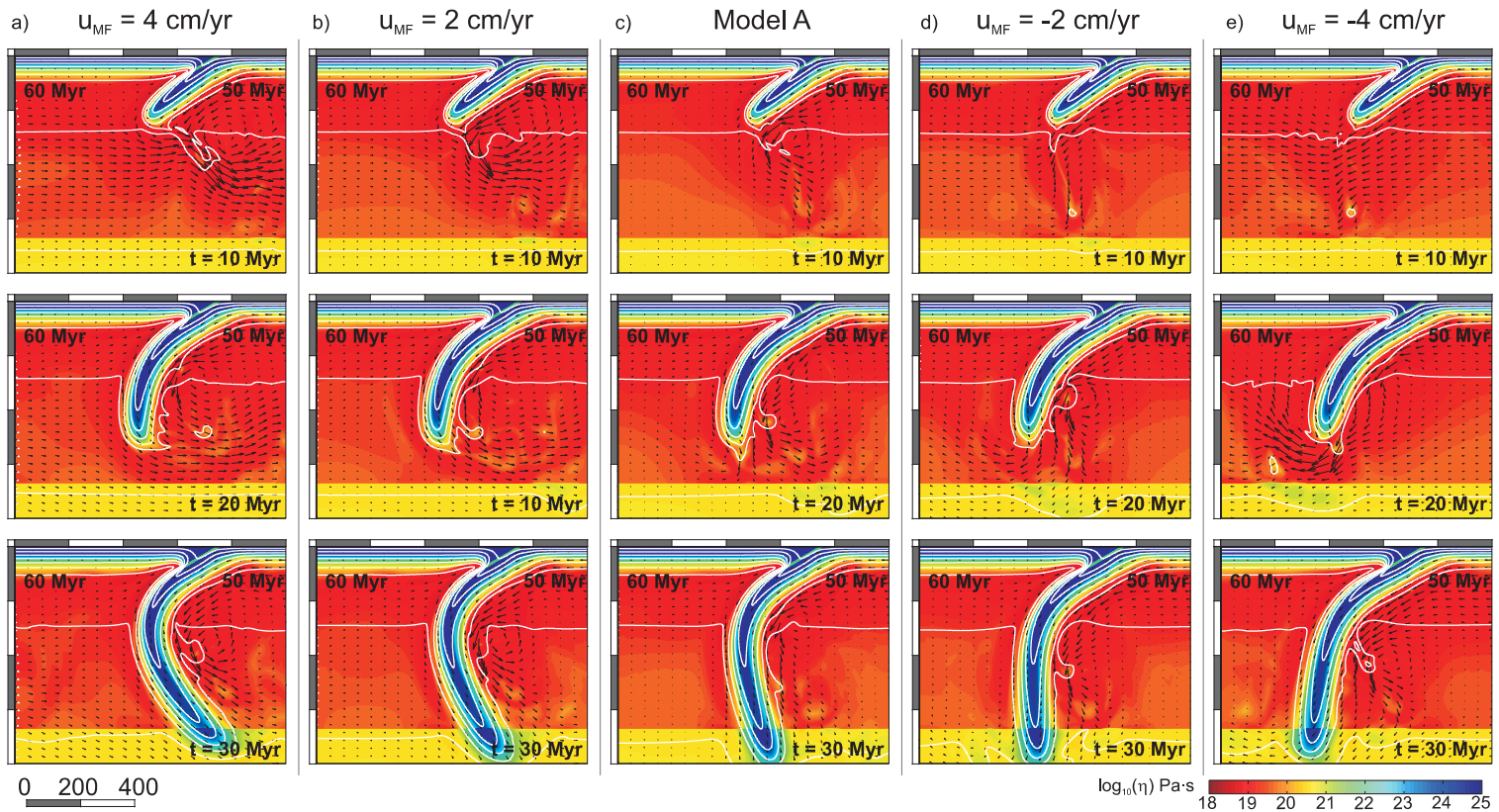

Figure 4.4: Model results at three different evolution times for models with an overriding plate of 60 Myr and subducting plate of 50 Myr for different mantle flow velocities. a) With a positive mantle flow velocity of 4 cm·yr^{-1}, b) with a positive mantle flow velocity of 2 cm·yr^{-1}, c) the reference Model A with no imposed mantle flow, d) with a negative mantle flow velocity of 2 cm·yr^{-1}, and d) with a negative mantle flow velocity of 4 cm·yr^{-1}. Decimal logarithm of the viscosity (color), isotherms every 200 K (contour) and velocity field (arrows) are shown. Subducting plate moves at 5 cm·yr^{-1}.

3º, and values of $\Delta\alpha_d$ vary between -14º and 11.5º. At the last time-step considered (35 Myr) $\Delta\alpha_s$ ranges between -9º and 5.5º, and values of $\Delta\alpha_d$ vary between -21º and 16º.

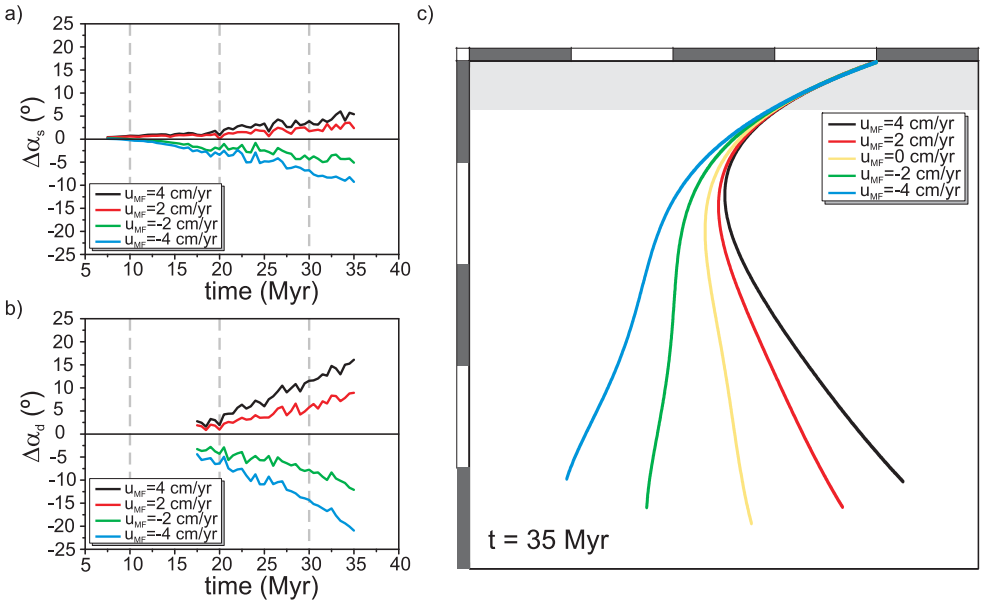

Figure 4.5: Comparison of evolution of models with different mantle flow velocities. Slab dip deviation from the reference model, a) $\Delta\alpha_s$ measured between 100 and 200 km and b) $\Delta\alpha_d$ measured between 300 and 400 km. Grey dashed lines indicate the time at which the snapshots of Figure 4.4 have been taken. c) Profiles of the top of the slabs after 35 Myr.

It is also important to notice that not only the angular deviation increases with depth and time, but the angular deviation along the slab accumulates. Therefore, at the final computed time (35 Myr) the geometries of the slabs are completely different depending on the intensity and the sense of the mantle flow (Figure 4.5.c). In fact, while in the reference model the slab slightly curves backwards, in models with a positive mantle flow the slab curves much more and its tip even goes beyond the trench. On the contrary, if the mantle flow velocity is negative, the flow supports the slab and, while the slab dip of the reference model increases with time, the slab dip of models with a negative mantle flow decreases. Therefore, the slab does not curl backwards, but sinks vertically for a mantle flow of -2 cm·yr^{-1} or even sinks at dips between 30º and 40º if the mantle flow velocity is -4 cm·yr^{-1}.

4.3.3. Influence on long-term evolution of subduction

The results obtained for 35 Myr of evolution raise the question of how the imposed mantle affects the slab for longer periods of time, and in particular the influence of the negative mantle flow to reduce the slab dip. In order to test the influence of the mantle flow for longer periods of time we have developed a model in which the bottom of the modeled region is set at 2000 km and with a negative mantle flow of 4 cm·yr^{-1}. The results of this model (Figure 4.6) show how during the first stages, the increased effect of slab gravitational torque produces a continuous increase of both shallow and deep slab dips. At 20 Myr, α_s reaches a maximum value of 40° and then decreases to 28° at 55 Myr, and α_d varies from 78° at 25 Myr to 65° at 55 Myr. After 55 Myr the low viscosity wedge closes, both plates become coupled and subduction stops. Provided that the subducting plate cannot move, but the deeper portion of the slab is still affected by the mantle flow and, after some time, the slab starts to tear.

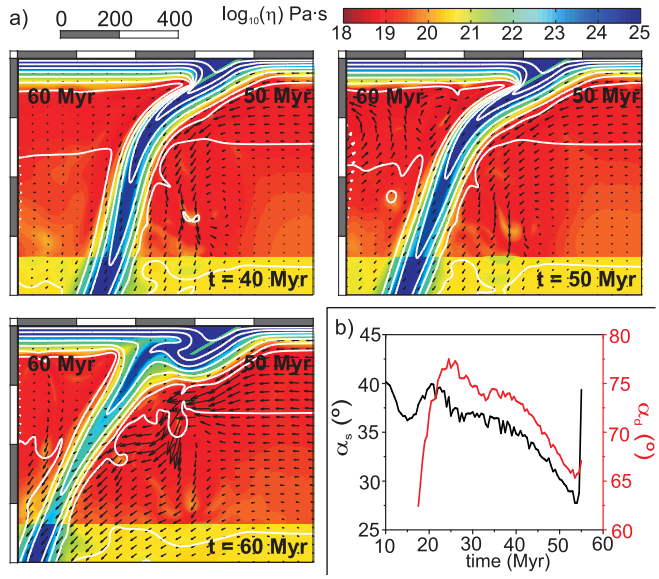

Figure 4.6: Results from a model with a negative mantle flow of -4 cm·yr^{-1}. Snapshots at 3 different evolution times. Colors, contours and arrow are the same as in Figure 4.4. b) Evolution of the slab dip measured at two different depths: between 100 and 200 km (α_s; black) and 300 and 400 km (α_d; red).

For a similar setup but with an even stronger negative mantle flow (-8 cm·yr^{-1}), the decrease of the slab dip is even greater (Figure 4.7). The purpose of this test is to simulate a scenario where the mantle flow velocity is higher than the

subduction velocity in order to see how the slab deforms in response to this differential motion. First, the maximum value of α_s reaches is reached before, at 10 Myr, when it takes a value of 49° and then decreases to 20° at 41 Myr, while α_s decreases from 74° at 20 Myr to 46° at 41 Myr. After about 41 Myr the low viscosity mantle wedge closes, both plates become coupled and subduction stops. In this case, subduction cessation takes place almost 25 Myr before than in the case with u_{MF}=-4cm·yr^{-1}.

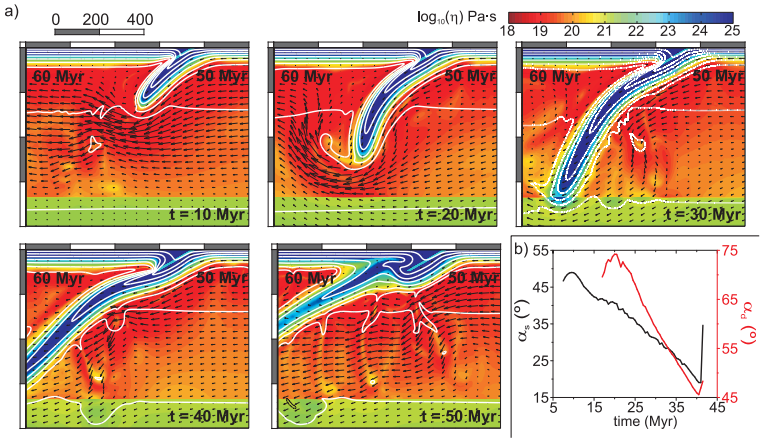

Figure 4.7: Results from a model with a negative mantle flow of -8 cm·yr^{-1}. Snapshots at 5 different evolution times. Colors, contours and arrow are the same as in Figure 4.4. b) Evolution of the slab dip measured at two different depths: between 100 and 200 km (α_s; black) and 300 and 400 km (α_d; red).

4.3.4. Effect of the slab strength

Depending on the slab strength, the mantle flow effect on the slab dip changes. We have run models with an imposed mantle flow of 4 cm·yr^{-1} (in both senses) in which the maximum allowed viscosity η_{max} is reduced to 10^{24} and 10^{23} Pa·s (in the reference model η_{max}=10^{25} Pa·s) and we compute the angular deviation from a model without mantle flow and with the same maximum viscosity (Figure 4.8). It is clear from these results that weaker slabs are more affected by a regional mantle flow and the angular deviation is greater than in the original models (η_{max}=10^{25} Pa·s), specially for the shallowest portion of the slab. After 35 Myr, for models with a maximum viscosity η_{max}=10^{24} Pa·s, the total angular deviation is around 30 degree for positive mantle flow and -25º for negative mantle flow when measured between 100 and 200 km ($\Delta\alpha_s$). For a

deeper portion of the slab, the angular deviation ($\Delta\alpha_d$) is around 20º for positive mantle flow and -30º for negative mantle flow. Modes that are even weaker (η_{max}=10^{23} Pa·s) show an even greater influence of the mantle flow, especially for negative mantle flow, and the angular deviation is around 30º for positive mantle flow and -40º for negative mantle flow when measured between 100 and 200 km ($\Delta\alpha_s$). For a deeper portion of the slab, the angular deviation ($\Delta\alpha_d$) is around 25º for positive mantle flow and -40º for negative mantle flow.

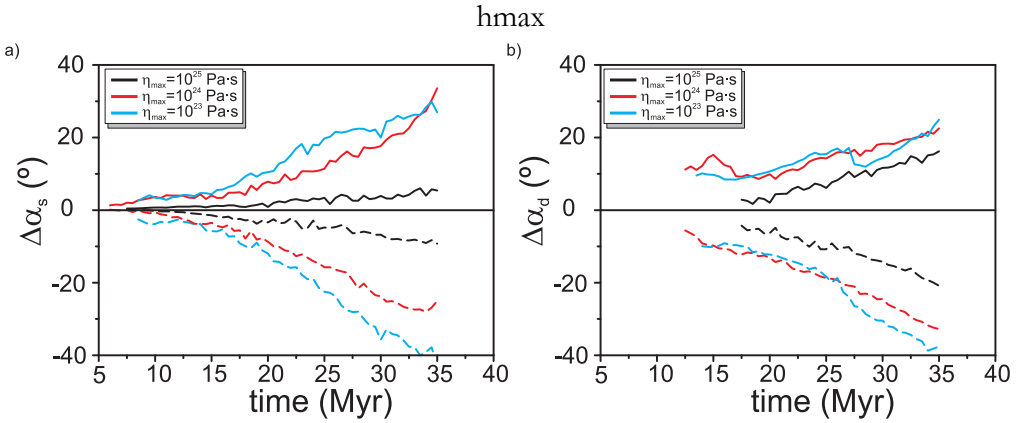

Figure 4.8: Comparison of evolution of models with different maximum allowed viscosities η_{max} for models with positive (solid lines) and negative (dashed lines) mantle flow. Slab dip deviation from the reference model, a) $\Delta\alpha_s$ measured between 100 and 200 km and b) $\Delta\alpha_d$ measured between 300 and 400 km.

4.4. Discussion

4.4.1. Slab dip deviation

Our modeling results point to a strong control of mantle flow with respect to the lithospheric plate on the geometry of the slab. In particular, mantle flowing in a direction opposite to the dip direction of the slab (i.e., mantle flow encroaching the slab) increases the angle of subduction. On the contrary shallower subduction zones are obtained when the mantle flows in the same direction of the dip of the slab (i.e., mantle sustaining the slab). The magnitude of increase or decrease of the slab dip is dependent on the mantle flow rate, with faster rates being more effective and the strength of the slab. The mantle flow is channeled between the tip of the slab and the top of lower mantle, increasing the

flow velocity as the slab reaches deeper depths and also increasing the torque caused by the mantle flow on the deeper portion of the slab. Consequently, the dip changes induced by mantle flow are larger at depth than at shallower levels. In principle, comparing results from models with opposed mantle flow sense, the total difference in slab dip after 35 Myr is almost 15º for α_s and more than 35º for α_d. These differences are even greater for weaker slabs, and the total slab dip difference comparing models with opposite mantle flow sense, (for $\eta_{max}=10^{24}$ Pa·s), reach values of 55º for and 50º α_s for α_d.

An important point to take into consideration is the fact that the models are 2D. Provided that only 2D flow is allowed, the mantle flow is forced to surround the slab around its tip, increasing the flow, but if the geometry was 3D and the material could flow around the edges of the slab the toroidal component of flow would increase. Therefore, in 3D models, the pressure exerted by the mantle flow on the slab would be lower. 2D models are a good approximation for the central region of wide slabs (e.g., *Schellart et al.*, 2007, and refferences therein) as is the case for Andean subduction zone. Therefore, these results should be understood as an upper bound of the slab dip variations generated by a regional mantle flow. In order to fully understand the influence of a mantle flow on toroidal and poloidal flow and slab geometry, 3D evolutive models incorporating mantle flow are needed.

4.4.2. Comparison with natural subduction zones and previous works.

It is important to compare the results obtained with the numerical simulations with slab dip variability found in nature. In previous works, variations of 60º are found in the deepest portions of the slabs along different subduction zones (*Cruciani et al.*, 2005; *Lallemand et al.*, 2005). In our simulations, for a mantle flow velocity of 4 cm·yr^{-1} and for strong slabs, the total angular deviation for the deep portion of the slab (35º comparing models with opposite mantle flow sense) would explain half of these variations, and for weaker slabs (50º comparing models with opposite mantle flow senses). This would explain an important part of the slab dip variability found in nature. However, it must be taken into account that the geometry of a slab strongly curled backwards that we obtain for positive mantle flow (facing the slab) is rarely found in nature. For this reason we

hypothesize that this flow would produce trench retreat (moving away from the overriding plate), rather than slab rollover geometry. Future work with models allowing for trench motions is needed to quantify this possible effect. In contrast, the model assumption of a fixed trench is expected to be less restrictive for negative mantle flow, as it is 'easy' for the flow to surround the slab along its base and it simply contributes to sustain shallower subduction. Actually trench retreat is much more commonly found in nature than trench advance (*Schellart et al.*, 2007). On the basis of our results, we speculate that trench retreat being more common than trench advance is compatible with the existence of global eastward mantle flow postulated by some authors (*Doglioni et al.*, 1999; *Riguzzi et al.*, 2009), with this east-directed mantle flow causing trench retreat in west directed subduction zones (Figure 4.2).

Mantle flow in the sense of subduction is also shown to further contribute to the occurrence of shallow and flat subduction and to put a limit of few tens of millions years on the duration of subduction. Extrapolating this result backwards in time, it could have important implications for the proposed multi-stage subduction history under North America (*Sigloch et al.*, 2008).

Our modeling results are in good agreement with the analog models of Boutelier and Cruden (2008). These authors performed 2D experiments of mantle flow, in which flow was directed to the upper plate in the upper mantle and in the opposite sense in the lower mantle. They showed that the imposed mantle flow with velocities similar to the convergence rate, lead to a reduction in the slab dip of around 30º, which agrees very well with the deviation that we obtain for slabs with similar viscosity. Their setup lead to opposite sense of flow in the upper and lower mantle, which strongly conditioned the evolution of deep slabs as it always produced slab roll over, and is therefore not appropriate to analyze long term subduction evolution. Our results are also in good agreement with Olbertz et al. (1997) that showed that mantle flow in the same sense of subduction decreases the slab dip and can even prevent penetration into the lower mantle for the case of low Rayleigh numbers. However, in contrast to Olbertz et al. (1997) we always obtain slab penetration into the lower mantle, even for very weak slabs. We interpret this difference to be partly caused by our choice of non-linear rheology, instead of the linear rheology they assumed, and use of kinematic conditions with a strong slab. It is well known that a linear

rheology leads to shallower slabs because hydrodynamic suction in the mantle wedge is higher than in the non-linear case (*Billen and Hirth*, 2005).

Future studies, including a 3D geometry and mobile trench, are needed to investigate with further complexity the effect of mantle flow in slab geometry and trench motion.

4.5. Conclusions

We have tested the effect of an imposed horizontal mantle flow with respect to the lithospheric plates on the geometry of the slab, and have shown that it is an important factor controlling the long-term slab evolution. As the slab sinks deeper into the mantle, the flow is channeled between the tip of the slab and the more viscous lower mantle, flow velocity increases and the effect of the mantle flow becomes stronger.

The magnitude of increase or decrease of the slab dip is dependent on the mantle flow rate and on the strength of the slab. For strong slabs dip changes induced by mantle flow are larger at depth than at shallower levels. Comparing results from models with opposed mantle flow sense, the total difference in slab dip after 35 Myr is almost 15º for α_s and more than 35º for α_s. These differences are even greater for weaker slabs, reaching values as high as 55º for α_s and 50º for α_a. for $\eta_{max}=10^{24}$ Pa·s.

Mantle flow in the sense of subduction is shown to enhance the occurrence of shallow and flat subduction. Moreover, it produces a progressive slab shallowing, which eventually ends ups with the closure of the mantle wedge and subduction inhibition.

5

3D MODELING

5.1. Introduction

In the models presented in Chapter 3 we focused on studying the influence of the thermal state of the overriding plate using 2D models, but some features can only be accounted for when using 3D models. First, the structure of the plates is not laterally uniform and some subduction processes take place beneath overriding plates with variable thermal state along the trench. This is the case of the subduction of the Cocos plate beneath the North America and Caribbean plates (See section 3.4), or the Nazca plate subducting beneath South America (Figure 5.1), which shows areas of increased elastic thickness (*Pérez-Gussinyé et al.*, 2008), increased plate thickness and seismic velocity (*Feng et al.*, 2007) and reduced heat flow (*Hamzaa et al.*, 2005; *Muñoz*, 2005). Beneath the Andes, there is a wide segment of flat subduction that has been suggested to be caused by the subduction of the so called "lost Inca Plateau" (*Gutscher et al.*, 1999). In central Chile, there is a narrow segment of flat subduction, which is thought to be related with the subduction of the Juan Fernandez Ridge (*Gutscher et al.*, 2000a). Bearing this in mind and according to the results from Chapter 3, we develop 3D models to test the influence on subduction dynamics of a non uniform overriding plate, containing regions of high and low temperature.

Mantle flow related to subduction also shows a 3D pattern, as inferred from geochemical and seismological studies. Shear wave splitting occurs when shear waves propagate through an anisotropic material and split into two orthogonally polarized waves that travel at different velocities. Shear-wave splitting of seismic waves travelling through the mantle is generally considered to be due to flow-induced shear strain and resulting lattice-preferred orientation (LPO) of mantle minerals (*Fouch and Rondenay*, 2006); thus, fast seismic splitting directions are assumed to be a good proxy for the direction of horizontal upper mantle flow. In general, far from subduction zones, fast seismic splitting direction (and therefore, mantle flow direction) correlates with plate motions, but observations from numerous subduction zones show that sub-slab fast seismic splitting directions are parallel or sub-parallel to the trench, giving support to a model in which sub-slab flow is usually trench-parallel and is induced by trench migration(*Long and Silver*, 2008, 2009). Shear wave splitting patterns in the mantle wedge are substantially more complicated, often showing sharp transitions between trench-parallel and trench-perpendicular fast directions (Figure 5.2).

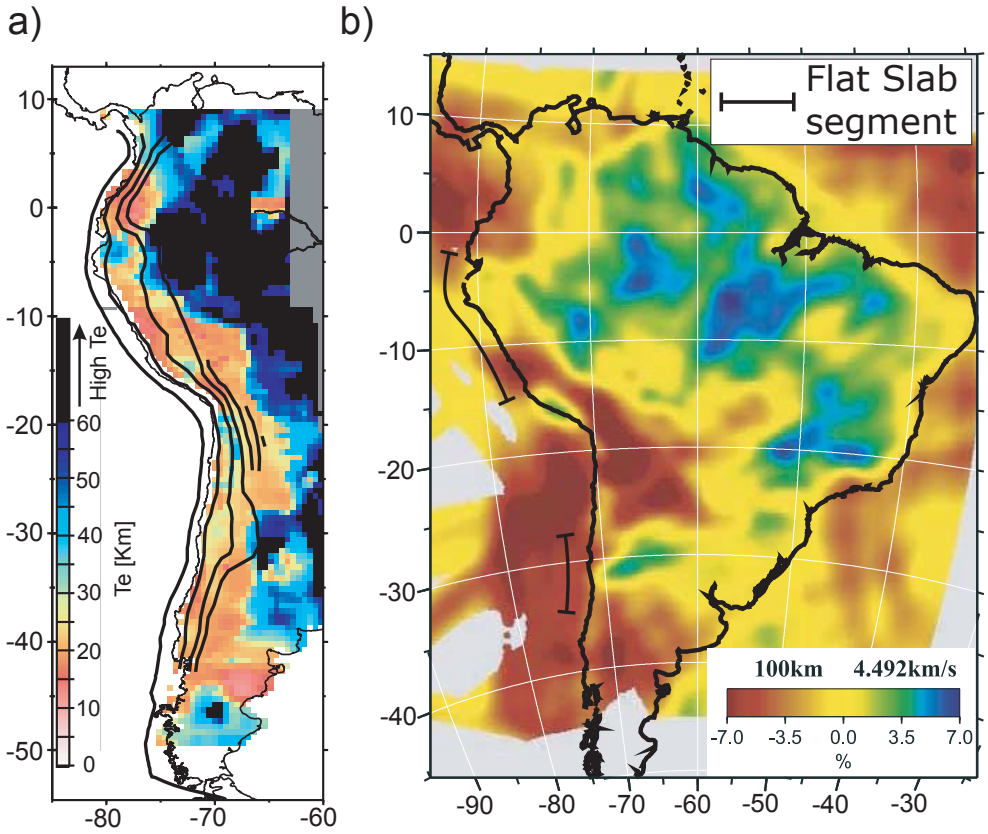

Figure 5.1: Example of non-uniform overriding plate and non-uniform slab dip in South America. a) Slab contours (black lines) and elastic thickness (color), from Pérez-Gussinyé . b) S-wave velocity anomaly at 100 km, from Feng et al. (2007).

Many subduction zones show a complex pattern of shear wave splitting that reflects an important component of trench parallel flow. For example, it has been suggested that mantle material underneath the South American subduction zone is flowing around the northern and southern edges of the slab (*Russo and Silver*, 1994). In another example, shear wave splitting and volcanic geochemistry suggest flow around the northern edge of the Tonga slab (*Turner and Hawkesworth*, 1998). Seismic anisotropy also reflects flow around the Northern (*Soto et al.*, 2009) and Southern (*Hoernle et al.*, 2008; *Abt et al.*, 2010) edges of the Cocos plate. Trench-parallel flow is not only inferred to occur at the edges of the slabs, but also in the central region of subduction zones like Cocos (*Rabble et al.*, 2011) or South America, beneath the flat segment beneath Perú (*Polet et al.*, 2000), and in Central Chile (*Anderson et al.*, 2004; *Anderson et al.*, 2007).

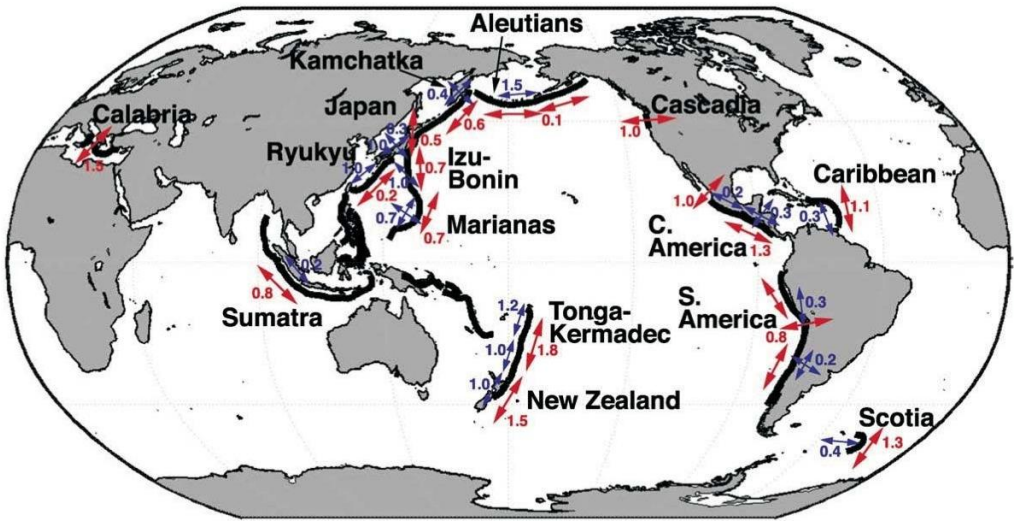

Figure 5.2: Sketch of constraints on subduction zone anisotropy from shear wave splitting measurements from Long and Silver(*Long and Silver*, 2008, 2009). Red arrows indicate average fast directions for the sub-slab splitting signal from SKS, local S, and source-side teleseismic S splitting measurements. The associated average sub-slab delay times are shown in red. Blue arrows indicate average fast directions for wedge anisotropy from local S splitting. Modified from Long and Becker (2010)

Different sources have been proposed to be responsible for the trench-parallel flow, such as oblique subduction or fast rotation of the plates, but here we focus on simple cases in which the slab subducts perpendicular to the trench. In this case, in 3D, subducting slabs induce two different types of flow in the mantle (Figure 5.3). First, the poloidal flow is the shear induced flow in the vertical plane parallel to subduction direction, which is captured in 2D models. Second, the toroidal and trench-parallel flow are horizontal flows only captured by 3D models. Toroidal flow around the slab edges is commonly related to the roll-back of the slab (*Funiciello et al.*, 2003; *Kincaid and Griffiths*, 2003; *Funiciello et al.*, 2006; *Piromallo et al.*, 2006; *Royden and Husson*, 2006; *Stegman et al.*, 2006; *Schellart et al.*, 2007) and is thought to be responsible for the trench parallel flow bellow the slab. Another factor that can also induce or enhance toroidal and trench-parallel flow is the heterogeneity of the slab shape and buoyancy along strike (*Kneller and van Keken*, 2007, 2008; *Jadamec and Billen*, 2010; *Capitanio and Faccenda*, 2012).

Numerical and analog models show that the toroidal flow around the edges of the slab has a strong influence on the slab geometry and trench migration rates (*Royden and Husson*, 2006). Stegman et al. (2006) showed that weak and thick slabs lead to enhanced toroidal flow. Another factor controlling the intensity of the

toroidal flow is the width of the slab, being stronger for wider slabs, although the ratio between toroidal and poloidal flow is found to be independent of the slab width (*Piromallo et al.*, 2006). However, for wider slabs, the effect of the toroidal flow only affects the slab locally, leading to deformation localized at the edges of the slab and a lower trench migration rate. For intermediate slab widths both periods of trench retreat and advance are found with velocities between 0 and 2 $cm \cdot yr^{-1}$(*Schellart et al.*, 2007). Nevertheless, all these models are set up with only a subducting plate, lacking overriding or lateral plates, which leads to overestimated trench migration rates and roll-back, generating slabs that sink almost vertically. If lateral and overriding plates are added the results show lower slab dips and less deformation (*Yamato et al.*, 2009).

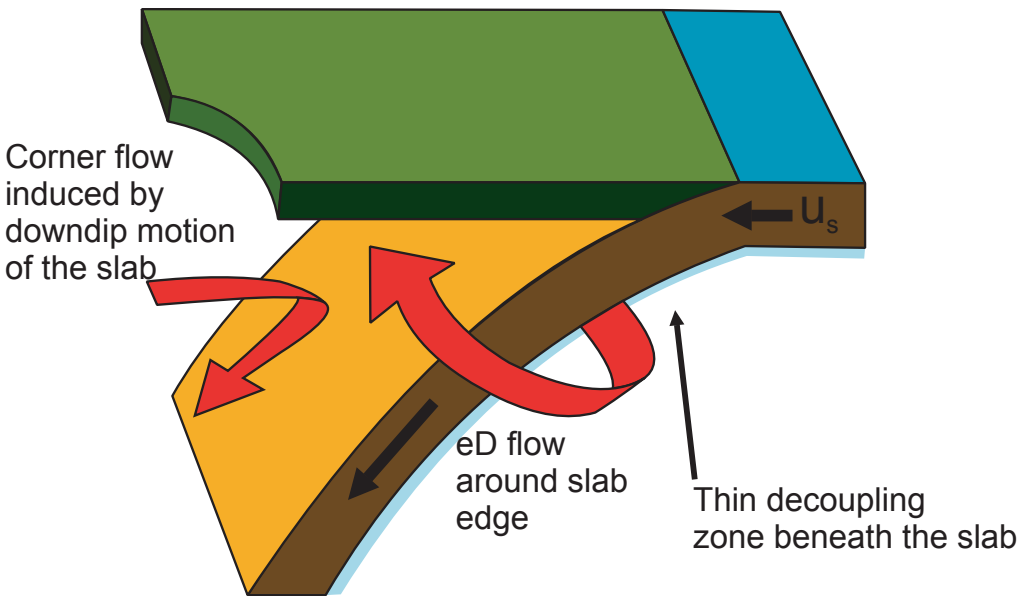

Figure 5.3: Schematic diagram of model, showing the dominance of 3D flow beneath the slab and the competing influence of 2D and 3D flow fields in the mantle wedge (*Long and Silver*, 2008).

Trench-parallel flow in the central region of a subduction zone has been obtained by means of 3D numerical modeling in which a prescribed slab with along trench dip variations is introduced (*Kneller and van Keken*, 2007, 2008). Differences in the dynamic pressure along the trench due to variations on the slab dip generate a strong trench-parallel flow that varies overtime as the slab subducts. Similarly, recent 3D instantaneous numerical models for the Alaska subduction (*Jadamec and Billen*, 2010, 2012) showed that the slab geometry, the

slab depth and the rheology are important factors controlling the flow pattern, including localized high velocities and trench parallel flow. Capitanio and Faccenda (2012) showed that along-trench variations of the buoyancy of the subducting plate drives pressure gradients triggering sub-slab trench parallel mantle flow. Faccenda and Capitanio (2012) calculated strain-induced LPO in 3D dynamic models of subduction and predicted trench-parallel sub-slab seismic anisotropy related to enhanced toroidal motions under retreating slabs. In contrast, they predicted trench-perpendicular fast seismic directions in the mantle wedge above the slab associated with poloidal flow and slab roll-back. In spite of these advances, the effect of lateral (along trench) heterogeneities of the overriding plate on mantle wedge flow pattern has not been investigated before. In this sense, Capitanio et al. (2011) studied the influence of an overriding plate of variable thickness on trench migration rates and margin morphology, but they did not focus on pressure gradients or flow gradients in depth, so no conclusions about mantle flow were drawn.

5.2. Modeling strategy

5.2.1. Governing equations and numerical method.

The modeled domain represents a spherical cap (Figure 5.4) in which equations of conservation of mass, momentum and energy are solved. Assuming that the fluid is incompressible and has a high Prandtl number, we can neglect inertial forces on the momentum equation. For simplicity, we also assume the Boussinesq Approximation, for which all thermodynamical variables (including density) are considered constant, but buoyancy force term due to temperature variations is included in the momentum equations (2.56), (2.61), (2.62) and (2.65).

To solve the models described in this section we use CitcomS v.3.1.1 using the multi-grid solver (section □). The modeled section is discretized through a mesh of brick elements with eight velocity nodes, linear shape functions and one constant pressure node for each element. The element density varies from one element every 4 km in the area of the plate boundary to one every 15 km in the lower mantle.

5.2.2. Model setup

The modeled region is 1500 km deep and extends 35° in the longitudinal direction and 25º or 45º in the latitudinal direction. Subduction takes place in the direction parallel to the longitudinal coordinate, from west to east and the plate boundary is located 22.5° from the western side of the model (Figure 5.4).

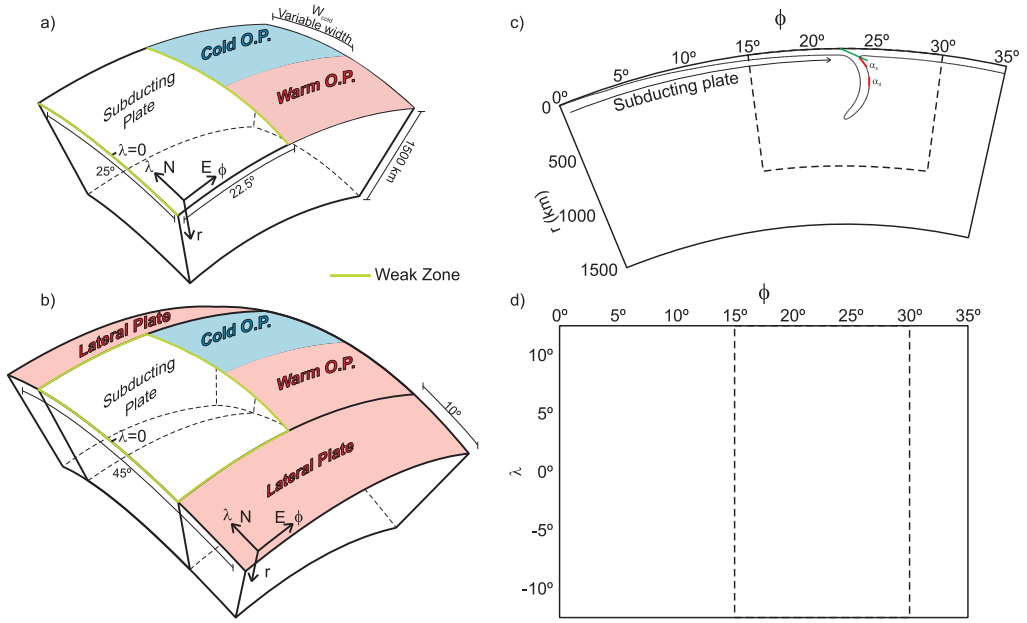

Figure 5.4: Schematic of the setup of the 3D models. a) Setup for models without lateral plates (Models 3D-A through 3D-H). b) Setup for models with lateral plates (Models 3D-I through 3D-K). c) Vertical cross section perpendicular to the trench and schematic representation of the two depth intervals at which the slab dip is measured (red lines). d) Map view of the model. In figures c and d, the dashed line represents the region of the model at which vertical and horizontal snapshots are shown in the next figures.

As explained in Chapter 3, if a kinematic-boundary condition is imposed on the subducting plate of a 2D model, it accounts for convergence induced by the combination of forces driving subduction, as the negative buoyancy of the full 3D slab. As the models presented in this section are already 3D, using a kinematic boundary condition is not the best choice. Therefore we develop models that are kinematically-driven only for comparison purposes (Models 3D-A, 3D-B and 3D-C in section 5.3.1), and models that are dynamically driven (Models 3D-D to 3D-K in sections 5.3.2, 5.3.3 and 5.3.4). In the second kind of models we impose a free-slip condition on the top of the subducting plate and

subduction evolves freely driven by pull force provided by a preexisting proto-slab. As in previous models, the plates are separated by a plate boundary modeled as a narrow low viscosity zone. The rest of the surfaces (top of the overriding plate, bottom and side boundaries) are also set as free slip (reflecting) surfaces. The setup consisting of a slab extending through the whole domain will be valid for the central region of a wide slab that continues as a mirror image on the sides of the modeled domain. This setup will be appropriate to simulate long subduction zones, that are surrounded by nearby slabs, as is the case of South America and Kuriles-Japan-Izu-Bonin-Mariana's system. On the contrary, models with lateral plates allow for flow around the slab edges, and are more appropriate to represent isolated and intermediate-width subduction zones, such as Middle America.

5.2.3. Initial Thermal Structure

For the kinematically-driven models (section 5.3.1) the initial temperature follows a Half Space Cooling Model (HSCM), which assumes that material in mid oceanic ridges is at a temperature T_1, and it cools down by vertical conduction as is moves away from the ridge, due to the effect of seawater at a lower temperature T_0. This is modeled as the cooling of a semi-infinite space where the surface is suddenly brought to the temperature T_0, and maintained at this value [6]. The resulting temperature profile is:

$$T = T_1 + T_0 - T_1 \; erfc\left(\frac{z}{2\sqrt{\kappa t'}}\right) \tag{5.1}$$

where *erfc* is the conjugate error function:

$$erfc(x) = 1 - \frac{2}{\sqrt{\pi}} \int_0^x e^{-y^2} dy \tag{5.2}$$

We adopt the value T_1=1400ºC. As before, the age of the subducting plate increases with the distance to the western boundary (which represents an oceanic ridge), but in this case, provided that we are using a spherical geometry, the age is computed as $t'=R_T\phi/u_s$, where R_T is the Earth radius and ϕ is the longitude and u_s

[6] Note that for the plate model used in the previous chapter, material cooled between two boundaries separated a distance L, at 0ºC and T_L.

is the subducting plate velocity. Therefore, for a subduction velocity of u_s=5 cm·yr^{-1}, and a plate boundary located at $\phi = 22.5^o$, the age of the subducting plate at the boundary is uniform along the trench and equals 50 Myr.

The temperature of the overriding plate does not vary in the trench-perpendicular direction, but can vary in the trench-parallel direction (Table 5.1). To study the effect of laterally varying overriding plates we divide the plate into two portions of widths W_{cold} and W_{warm} (Figure 5.4). We only modify the thermal state of the northern portion of the plate, while keeping the southern portion always war.

We choose a HSCM temperature profile because CitcomS solves the Navier-Stokes equation under the Boussinesq Approximation, which assumes that there are not temperature variations due to pressure changes, and therefore we cannot assume an adiabatic profile for the sublithospheric mantle as we did in Chapter 3. Due to the fact that the initial temperature profile is not exactly the same as in our previous models, the same ages are related to different thermal state. Therefore, to avoid confusion, we do not focus anymore in the age of the overriding plate but in its thermal state. In order to compare the thermal state of different models, we use the temperature at a depth of 100 km T_{100} .

The temperature of the top boundary of the domain is fixed at 0ºC and the bottom at T_1=1400ºC. The side boundaries are thermally insulated.

Dynamically-driven models (3D-D through 3D-K, Table 5.1) require a preexisting proto-slab to obtain a self-sustaining subduction process. This proto-slab provides enough slab-pull to drive the process and is obtained from a previous model with an imposed velocity on the top of the subducting plate. In other words, the subduction process of dynamically-driven models is modeled in two stages: in the kinematic stage the models start running with an imposed subduction velocity of 5 cm·yr^{-1}, until the subducted slab is long enough to provide enough slab-pull to keep subduction going; at that moment (t=0 Myr), the dynamic stage starts, the imposed subduction velocity is removed and subduction evolves freely. This way of proceeding ensures that the initial temperature distribution is smooth, which makes the models more easily convergent. Moreover, this temperature distribution is more realistic than a synthetic distribution.

Table 5.1: Parameters for all the models completed for this study. S.P.: Subducting plate. O.P.: Overriding Plate

Model	*S.P. boundary condition*	*Warm portion of the O.P.*			*Cold portion of the O.P.*			*Proto-slab*	*Lateral Plates*	*Max* $\Delta\alpha_{s,d}$
		Width W_{warm}	T_{100} ºC	*Age (Myr)*	*Width* W_{cold}	T_{100} ºC	*Age (Myr)*			
A	Kinematic	25º	1290	50	Uniform			No	No	--- ---
B	"	19.5º	"	"	5.5º	1140	90	"	"	25º 40º
C	"	"	"	"	"	1100	100	"	"	45º 30º
D	Dynamic	25º	"	"	Uniform			Uniform	"	--- ---
E	"	19.5º	"	"	5.5º	1140	90	Non-uniform	"	20º 25º
F	"	"	"	"	"	1100	100	"	"	50º 20º
G	"	"	"	"	"	970	150	Uniform	"	30º 20º
H	"	12.5º	"	"	12.5º	"	"	"	"	30º 25º
I	"	25º	"	"	Uniform			"	Yes	--- ---
J	"	19.5º	"	"	5.5º	970	150	Non-uniform	"	15º 10º
K	"	12.5º	"	"	12.5º	"	"	"	"	20º 20º

3D models are much more computationally demanding than 2D models, therefore, we are not able to make an extensive systematic study for different overriding and subducting plates as we did in Chapter 3. The subducting plate is 50 Myr at the plate boundary throughout all the models. The southern portion of the overriding plate is always warm T_{100}=1290ºC while the northern portion has different thermal states in different models.

5.2.4. Rheology

As in the previous chapter, we use a composite rheology, equations (2.29) and (2.30), but this time we also add a more realistic pseudo-plastic behavior, equation (2.31), that also facilitates subduction, as it favors the bending of the plate by weakening it at the plate boundary (Figure 5.5). We also impose a maximum viscosity cut-off, $\eta_{\max}=10^{24}$ Pa·s for cold temperatures[7] and a minimum viscosity cut-off $\eta_{\min}=10^{19}$ Pa·s. The rheological parameters used in this section are listed in Table 5.2 and are in accordance with those given by Hirth and Kohlstedt (2003). These parameters are chosen so that the total viscosity at 250 km is $\eta_{250}=10^{20}$ Pa·s, and the viscosity in the lower mantle is uniform with a viscosity of $8.8\cdot10^{21}$ Pa·s. The flow-law pre-exponent has been multiplied by a factor F_2 (0.33333 for diffusion creep; 0.30079 for dislocation creep) to account for the fact that the numerical code uses the second invariant of strain-rate and stress, rather than the differential stress and axial strain-rate used in the experimental setting (see *Gerya*, 2009, p. 75-76).

We are using the HSCM, which does not include and adiabatic increase for the mantle. Therefore, for the viscosity, we need to include a compressibility gradient in the mantle. To do so, we introduce in the composite viscosity expression, equation (2.29), a modified temperature T_t:

$$T_t = T + m_{ad} z \tag{5.3}$$

where $m_{ad} = 0.3$ K/km is the adiabatic temperature gradient and z is the depth.

[7] We run tests that show that there is not significant difference in the geometry of the slab between models with $\eta_{\max}=10^{25}$ Pa·s and $\eta_{\max}=10^{24}$ Pa·s, but the second set of models converge much faster.

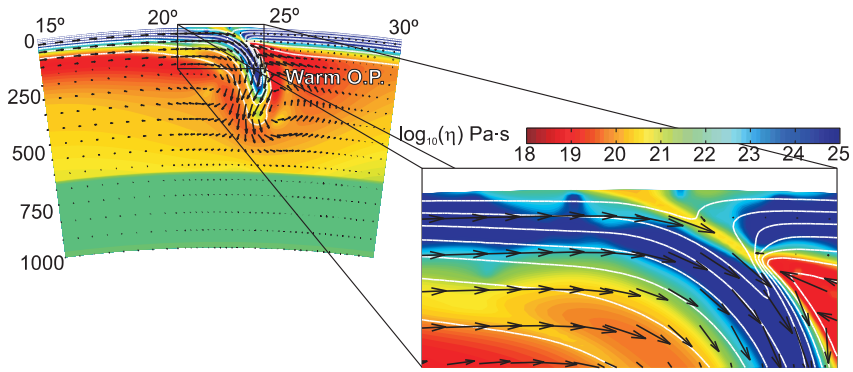

Figure 5.5: Weakening due to pseudo-plastic yielding. Detail of the initial time-step from Model 3D-D (Table 5.1). Decimal logarithm of the viscosity (color), isotherms every 200 K (contour) and velocity field (arrows) are shown.

As in previous models we impose a 30º dipping low viscosity channel at the plate boundary, but this time we also include a vertical low viscosity channel at the ridge (western boundary) to detach the subducting plate from this boundary and enable subduction. When lateral plates are added, vertical low viscosity channels of 35 km are imposed on both sides of the subducting plate to decouple it from the lateral plates (Figure 5.4). As before, the viscosity at the channels is calculated according to its temperature, pressure and strain rate using equation (2.29), but the maximum allowed viscosity is $\eta_{lvc}=10^{21}$ Pa·s.

5.3. Results.

The main objective in this section is to develop more realistic models that will allow generalizing the results Chapter 3 for 3D geometries. We develop several sets of models in which the complexity is increased gradually, in order to correctly interpret the results of more complex models analizing the effect of each of the new added features.

First, in Models 3D-A to 3D-C (section 5.3.1) we develop models with similar characteristics, using a similar geometry (expanded in 3D), background viscosity and boundary conditions (these models are still kinematically driven), but we add a more complex rheology (as explained in section 5.2.4). Second, in Models 3D-D to 3D-K (sections 5.3.2 and 5.3.3), we change the boundary conditions to allow for a dynamically–driven subduction. And finally, in Models 3D-I to 3D-K (section 5.3.4), we add lateral plates on both sides of the model in order to allow flow around the edges of the slab.

Table 5.2: Model parameters

Symbol	Meaning		Value	
u_s	Subduction velocity		5 cm yr^{-1}	
	Domain horizontal extent		Latitude: 25º to45º Longitude: 35º	
H	Domain vertical extent		1500 km	
T_0	Temperature at top of the plate		273 K	
T_1	Temperature at the bottom of the lower mantle		1673 K	
κ	Thermal diffusivity		10^{-6} m^2 s^{-1}	
α	Thermal expansion coefficient		2×10^{-5} K^{-1}	
Ra	Rayleigh number		$2.34\cdot10^{9}$	
ρ_0	Reference density (at 273 K)		3300 kg m^{-3}	
η_b	Maximum viscosity at the shear zone		10^{21} Pa s	
η_{max}	Maximum viscosity		10^{24} Pa s	
	Rheological Parameters [a]		**Diffusion**	**Dislocation**
n	Stress exponent		1	3.5
A	Preexponential factor (Pa)		1	$90\cdot10^{-21}$
E	Activation energy (J·mol^{-1})		335000	480000
V	Activation volume (m^3·mol^{-1})	Up. mantle	$4.0\cdot10^{-6}$	$12.0\cdot10^{-6}$
		Low. mantle	$1.54\cdot10^{-6}$	
d	Grain size (m)	Up. mantle	$6.0\cdot10^{-3}$	
		Low. mantle	$45.0\cdot10^{-2}$	
p	Grain size exponent		3.0	
C_{OH}	OH concentration (ppm-H/Si)		1000/1	1000/1
r	C_{OH} exponent		1.0	1.2

[a] Hirth and Kohlstedt (2003)

As we did in Chapter 3, in order to analyze the results, we focus on the slab geometry and the slab dip, comparing slab dip variations with time, variations along the trench and variations between different models. We present figures showing the results for specific vertical and horizontal sections of the modeled domain (dashed lines in Figure 5.4.c and d) and the result derived from computing the slab dip at different depths and time-steps. Due to the lack of tracers, the top surface of the slab is defined using the 1100ºC isotherm. The slab dip is computed using a linear approximation of this isotherm at two different depth intervals (Figure 5.4.c): the first 100 km starting from the base of the coldest portion of the overriding plate α_s and between 200 and 300 km from the base of the coldest portion of the overriding plate α_d.

5.3.1. Kinematically-driven models

In the first set of models, as for the 2D models from Chapter 3, subduction is kinematically-driven by imposing a subduction velocity of 5 cm·yr^{-1} on the top boundary of the subducting plate. The two main objectives of this section are to validate the conclusions from Chapter 3 and to test the effect of non-uniform overriding plates when the subducting plate is kinematically-driven.

For comparison purposes, it is useful to start by focusing on a model equivalent to the 2D models, i.e., a model with a uniform overriding plate and a setup consisting of a 3D expansion (along the latitudinal coordinate) of a 2D geometry. Model 3D-A (Figure 5.6 and Video 5.A) has a warm uniform overriding plate (T_{100}=1290ºC) and the evolution is similar to that of the 2D models, provided that only poloidal flow occurs. Some of the common characteristics are: initially, the slab dip increases with time reaching values of 60º at 9.0 Myr; the slab dip has a period of stability in which dip remains constant until 15.8 Myr; the slab dip is higher for the deeper portion of the slab. On the other hand, there is a significant difference with the 2D models. In this case, when the slab reaches the lower mantle at 15.8 Myr, the viscous resistance forces the tip of the slab to bend backwards, leading to a flattening of the slab, whereas in 2D models this did not occur. This was described by Billen and Hirth (2007) and is a consequence of the fact that it is easier for the slab to migrate laterally to accommodate the decrease in sinking rates between the lower viscosity upper mantle and higher Newtonian-viscosity lower mantle. This backward bending did

not occur in 2D models because a hotter and less viscous mantle was assumed. The adiabatic temperature profile used in 2D models leaded to a temperature as high as about 1700 ºC at the upper-lower mantle boundary, whereas the temperature at the upper-lower mantle boundary in 3D models, including the adiabatic increase of the temperature in equation (5.3), is 1600 ºC (see Section 0). This means that in 3D models the mantle is colder and therefore more viscous ($1.5 \cdot 10^{21}$ Pa·s in the 2D models vs. $1 \cdot 10^{22}$ Pa·s in the 3D models). This increases the viscous resistance making it more difficult for the slab to penetrate into the lower mantle and leads to more bending.

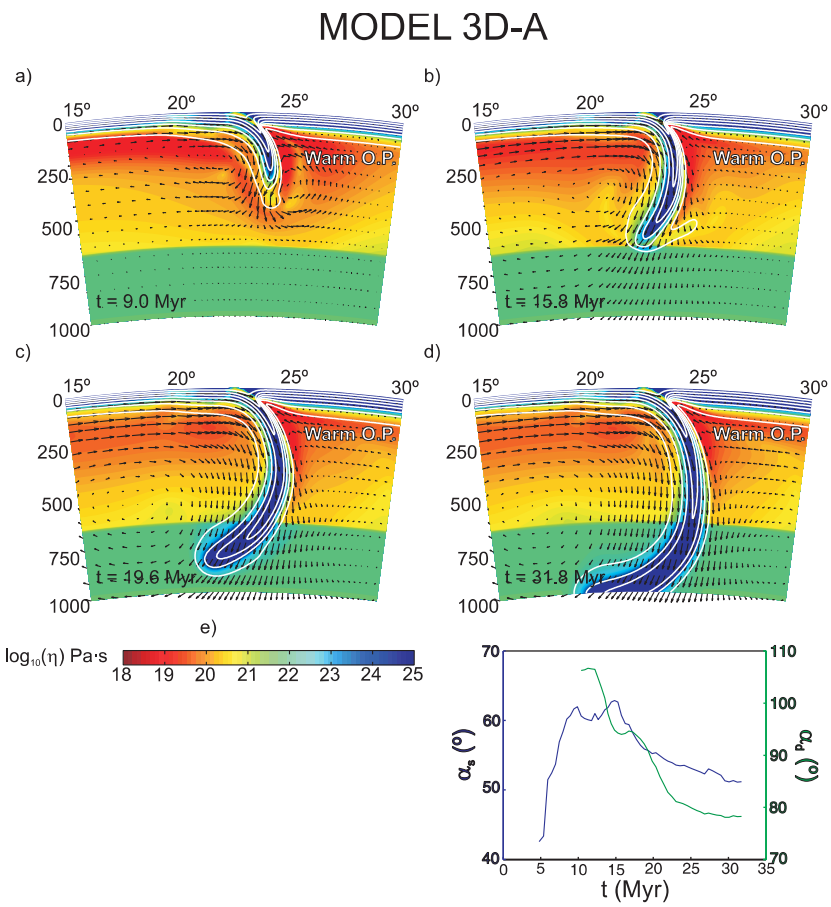

Figure 5.6: Evolution of Model 3D-A (Table 5.1) with time. (a-d) Vertical sections at four different time-steps. Colors, contours and arrow are the same as in Figure 5.5. Subducting plate moves at 5 cm·yr^{-1}. e) Variations of the slab dip with time computed at two different depth ranges.

For a colder, but still uniform, overriding plate (figure not shown), the behavior is similar to 2D models, and the slab dip decreases for colder overriding

plates. With this test of control we corroborate that with a different geometry, a different mesh resolution, a different rheology and using different software, we still obtain the same conclusion as in the 2D modeling, namely the significant role played by the thermal state of overriding plate on slab dip.

It is more interesting to take a look at what happens when the overriding plate is not uniform. The control test described above shows that, also in 3D models, if the overriding plate is colder, the hydrodynamic suction increases and the slab dip decreases. The question we now address is what happens when the suction only increases beneath a portion of the overriding plate. There are three possible scenarios: if the plate is rigid and the suction is high enough beneath the northern portion, the dip of the whole slab will be lower; if the plate is rigid and the suction beneath the northern part is not high enough, the dip of the whole slab will be similar to that of Model 3D-A; if the plate is not rigid, the plate will bend, resulting in a laterally (along the trench) variable slab dip, being lower in the northern region than in the southern region.

Model 3D-B (Figure 5.7and Video 5.B) shows the results of a simulation in which the northern 5.5º wide portion of the overriding plate is colder (T_{100}=1140ºC). From the beginning of the simulation, the increased suction beneath the cold portion of the overriding plate causes the slab to subduct at a shallower dip than beneath the warm portion (Figure 5.7.a vs. Figure 5.7.b) and at 13.0 Myr the slab has reached the depth range where α_d can be measured in the warm region but not in the cold region (Figure 5.8.a). Beneath the warm region the slab dip is much higher, which causes the plate to contort, presenting a variable slab dip. With time, the slab dip variations along the trench persist, but decreases significantly with time (Figure 5.8.a): for α_s, the maximum difference reaches 25º at 9 Myr and 10º at 28.6 Myr for α_d, the maximum slab dip variation is 40º at 13.8 Myr and 20º after 28.6 Myr.

In Model 3D-C (Figure 5.9 and Video 5.C) the cold portion of the overriding plate is even colder (T_{100}=1100ºC) than in Model 3D-B (T_{100}=1140ºC). The suction in the cold region is even higher, which reduces the slab dip so much that it reverses its curvature, leading to a flat slab (Figure 5.9.a to c). With time, the northern portion of the slab keeps subducting flatly, but the steeper portion of the slab (Figure 5.9.d) starts pulling down the flat section. This causes the flat

section to start steepening from south to north and the flat segment narrows, but the slab-dip variations remain (Figure 5.8.b). The slab dip in the cold region is lower than in Model 3D-B, but in the warm region, slab dips from both models are similar. Therefore, for α_s at 8.5 Myr the maximum slab dip variations is greater than 45º and at 25.6 Myr it decreases to 15º. For α_d the maximum variation remains approximately constant around 30º.

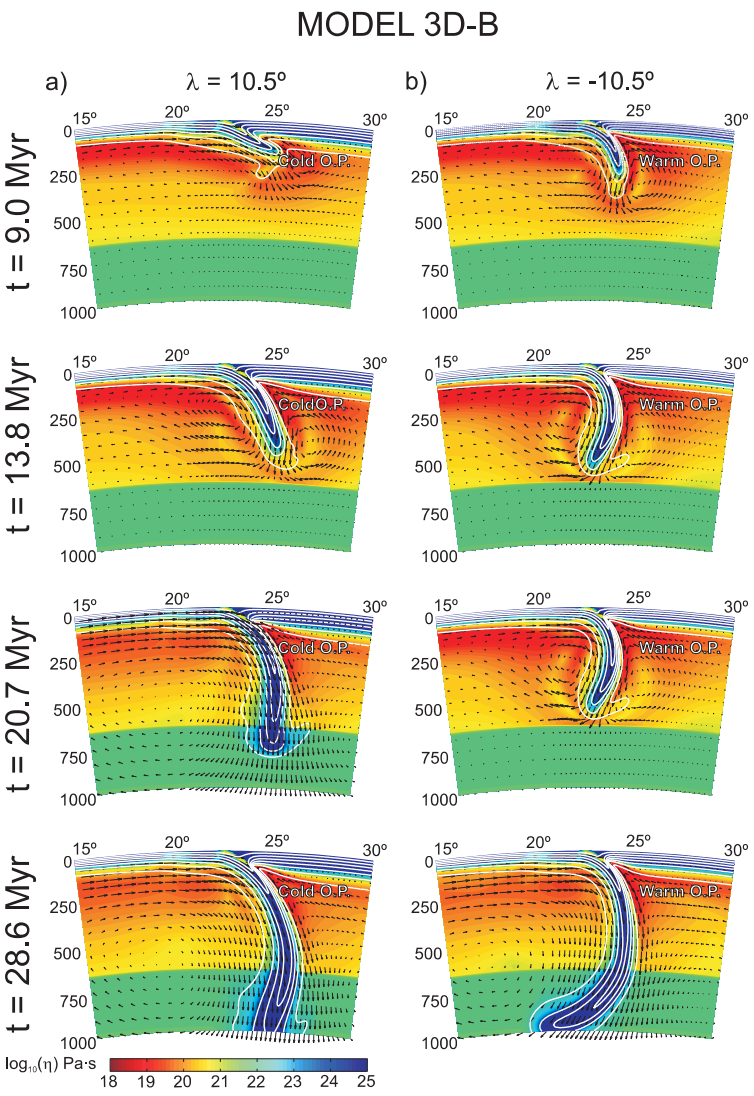

Figure 5.7: Evolution of Model 3D-B (Table 5.1) with time. Vertical sections at two different time-steps taken at two different latitudes: a) λ = 10.5º and λ = -10.5º (λ = 0º is located in the center of the model domain, Figure 5.4). Colors, contours and arrows are the same as in Figure 5.6. c) Variations of the slab dip along the trench (the slab dip is computed at two different depth ranges). Note that vertical scale is variable in panels in c)

5.3.2. Dynamically-driven models: Non-uniform initial slab-dip

The previous results show how differences in the hydrodynamic suction created by variations of the thermal state of the overriding plate can induce slab dip variations if the plates are kinematically-driven. However, we would also like to know if these variations can be maintained even if the plates are not driven by any external force, but subduct only due to its own negative buoyancy.

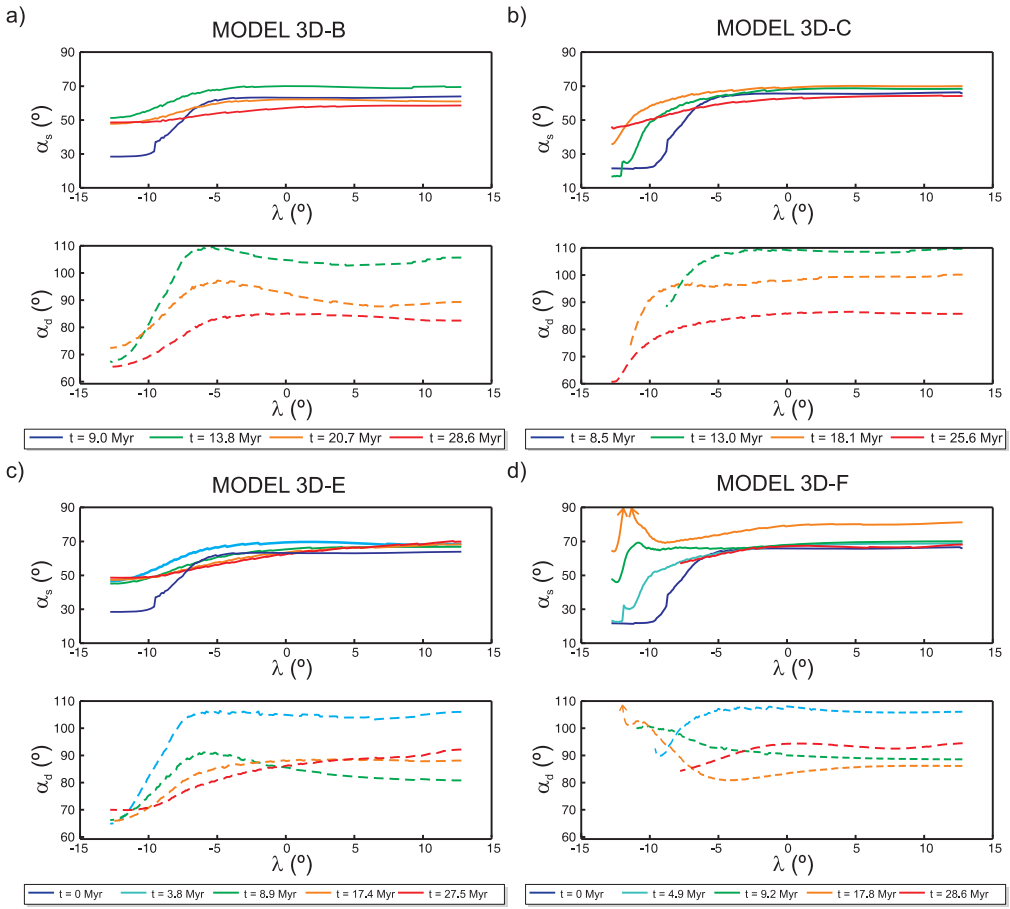

Figure 5.8: Variations of the slab dip along the trench computed at different depths and time-steps. Four models are shown (Table 5.1): a) Model 3D-B, b) Model 3D-C, c) Model 3D-E, d) Model 3D-F.

In this next set of models we change the boundary conditions and set a free-slip condition at the top of the subducting plate. If there is a proto-slab at the moment the simulation begins, it sinks due to its negative buoyancy. If the

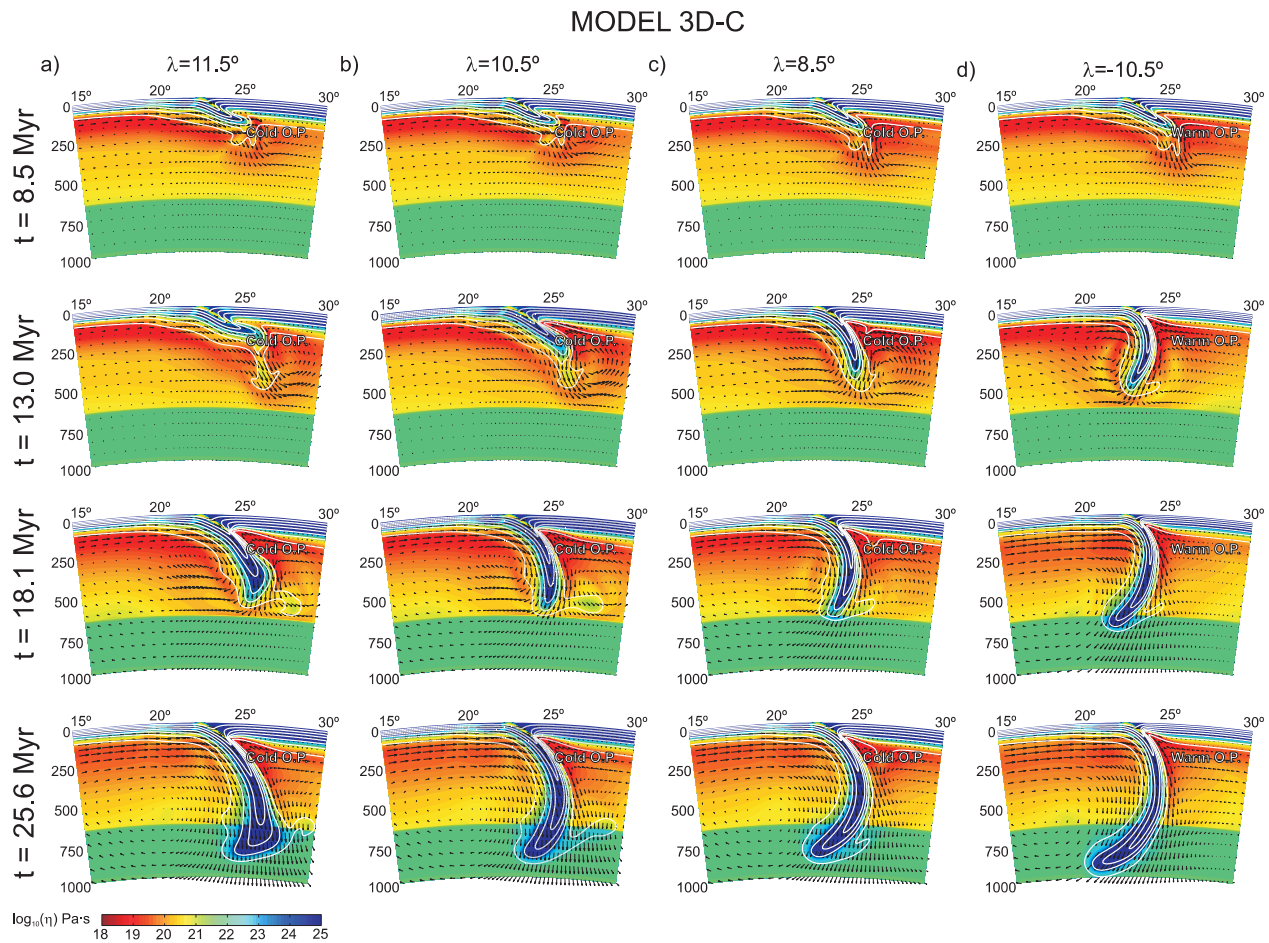

Figure 5.9: Evolution of Model 3D-C (Table 5.1). Vertical sections at four different time-steps taken at four different latitudes: a) λ = 11.5°, b) λ = 10.5°, c) λ = 8.5°, d) λ = -10.5°. Colors, contours and arrows are the same as in Figure 5.6.

pull force provided by the proto slab is high enough it drives the subducting plate and subduction is maintained in a self-consistent way. The proto slabs used in these models are obtained from the kinematically-driven models from section 5.3.1. After a certain evolution time, the resulting temperature distribution is used as the initial temperature for these dynamic models. Another important factor to achieve self-driven subduction is the strength of the slab. The subducting plate has to be weak in order to bend at the plate boundary, and to do so there are two options, i.e., weakening the whole slab to at least 10^{23} Pa·s or using a weakening mechanism to reduce the viscosity of the slab locally, only at the plate boundary. We use the second option by adopting a pseudo-plastic rheology, equation (2.31). This choice is more realistic and less restrictive than introducing an overall weakened slab.

Model 3D-D (Figure 5.10 and Video 3D-D) shows the evolution of a slab beneath a uniform warm overriding plate (T_{100}=1290ºC), and it is started from a solution of Model 3D-A after 9.0 Myr, therefore, its initial slab dip is uniform. The tip of the slab reaches approximately 260 km deep (measured from the base of the overriding plate), which provides enough slab-pull to drive subduction. Initially, the average velocity is 4.6 cm·yr^{-1} (Figure 5.11.a) and it is uniform through the plate (Figure 5.12.a). As the model evolves and the slab length increases, the mean velocity increases up to 11.5 cm·yr^{-1} at 3.8 Myr. Therefore, the slab reaches the lower mantle faster than in Model 3D-A (were de subduction velocity was 5 cm·yr^{-1}), and the flattening takes place earlier (Figure 5.10.f). Also, when the slab reaches the lower mantle, the velocity decreases significantly (4.2 cm·yr^{-1} at 9.6 Myr) due to the increased viscous resistance in the lower mantle. After some time, once the tip of the slab goes through the upper-lower mantle boundary, the slab tip starts unbending and sinks vertically again (Figure 5.10.e).

If the overriding plate is colder, but still uniform, the initial dip of the proto-slab is lower. In spite of this, as soon as the model starts evolving dynamically, the slab steepens, subducting at a higher angle and the rest of the evolution is similar to that of Model 3D-D.

These results show that dynamically-driven models tend to produce vertical sinking slabs, making the existence of shallow slab dips more difficult. But we are going to show that the dynamics changes when the overriding plate is not uniform.

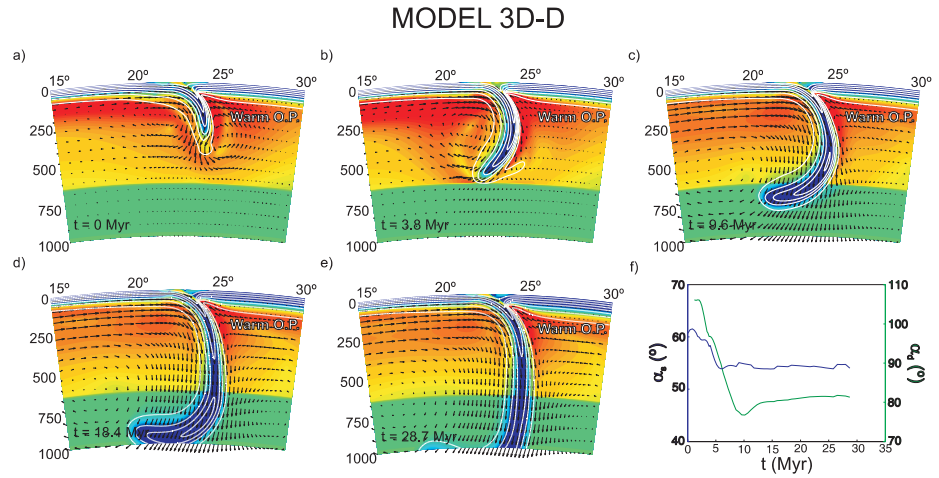

Figure 5.10: Evolution of Model 3D-D (Table 5.1) with time. (a-e) Vertical sections at five different time-steps. Colors, contours and arrows are the same as in Figure 5.6. f) Variations of the slab dip with time computed at two different depths.

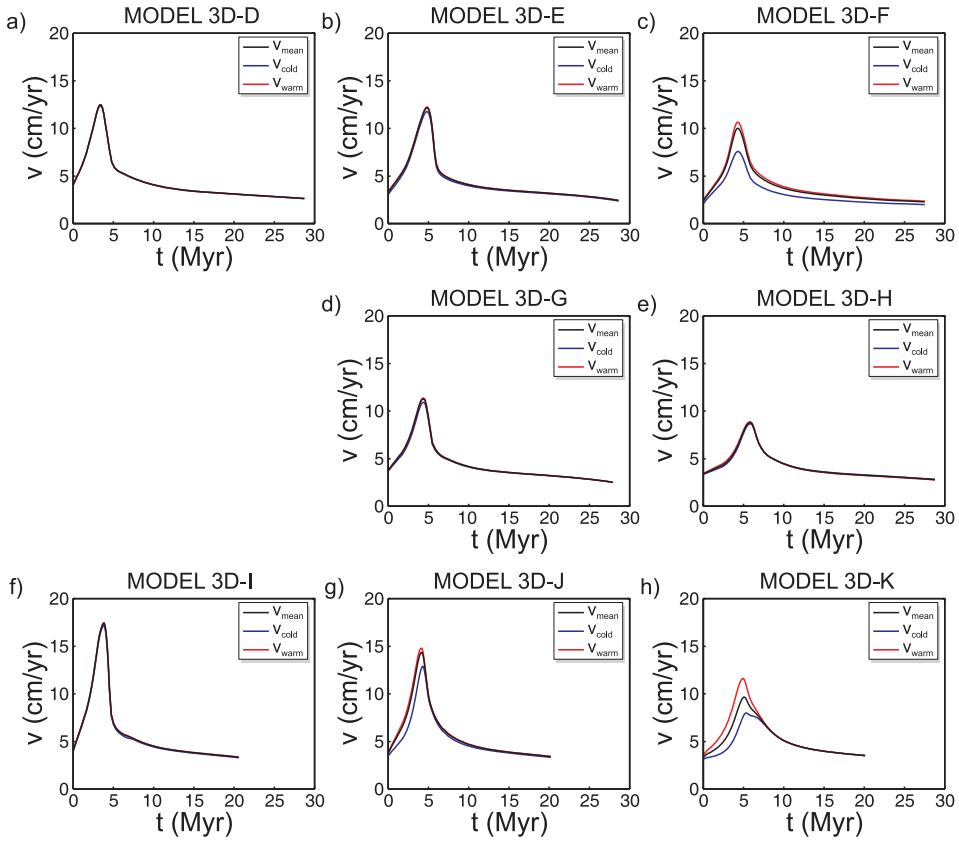

Figure 5.11: Mean plate velocity with time for eight different dinamically-driven models (Table 5.1). Top row: non-uniform proto-slab. Middle row: uniform proto-slab. Bottom row: uniform proto-slab and lateral plates. The velocity is computed for the whole plate (v_{mean}), the portion of the plate subducting in the cold region (v_{cold}) and in the warm region (v_{warm}).

Model 3D-E (Figure 5.13 and Video 5.E) is started from Model 3D-B after 9.0 Myr of evolution, therefore, not only the overriding plate is non-uniform, but also the initial dip of the proto-slab. Initially, the portion of the slab beneath the coldest portion of the slab steepens (Figure 5.13.a), but its slab dip is still lower than beneath the warm region (Figure 5.13.b). As the simulation evolves, the variations in the slab dip along the trench are maintained (Figure 5.8.c) due to the increased suction beneath the cold portion of the overriding plate. The initial proto-slab shows differences of 25º for the shallow portion, and after 27.5 Myr it decreases to 20º (Figure 5.8.c). For the deep portion, after 3.8 Myr, the slab dip varies around 45º, and at 27.5 Myr the difference is still around 25º. Therefore, the slab dip variations are similar to those of the kinematically-driven Model 3D-B. The mean velocity of the subducting plate is similar to that of Model 3D-D (Figure 5.11.b), and is still relatively uniform (Figure 5.12.b) showing that the portion of the slab with a lower angle does not slow down the subducting plate.

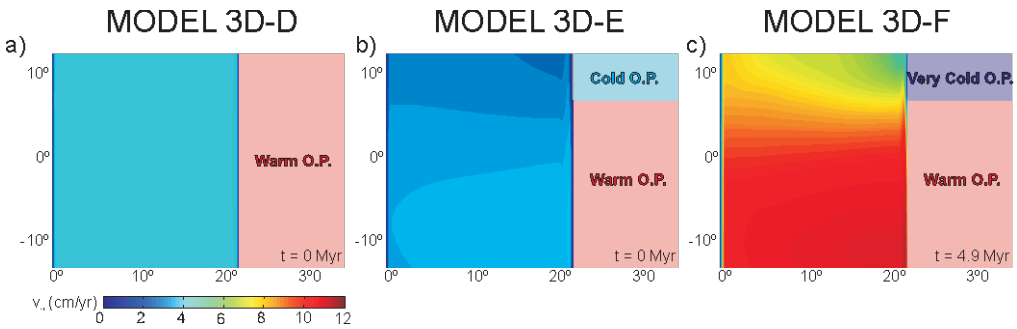

Figure 5.12: Map view of the surface velocity (colors) for the subducting plate of the dynamically-driven Models 3D-D (a), 3D-E (b) and 3D-F (c).

Model 3D-F (Figure 5.14 and Video 5.F) is started from Model 3D-C after 8.5 Myr of evolution, therefore, the northern portion of the overriding plate is even colder and the initial proto-slab subducts flatly beneath it. Initially, the flat segment does not provide any slab-pull but the steeper segment does. In this case, the steeper segment provides slab-pull for the whole plate, even the flat segment. Therefore, the steep segment drags down the flat segment, whereas the flat segment slows down the steep one. After 4.9 Myr this results in lower mean velocity for the whole plate of 9.3 cm·yr^{-1} (Figure 5.11.c) a non-uniform velocity (Figure 5.12.c) that subducts faster beneath the southern portion of the overriding plate (at 9.9 cm·yr^{-1}), where the steep segment of the slab is pulling the

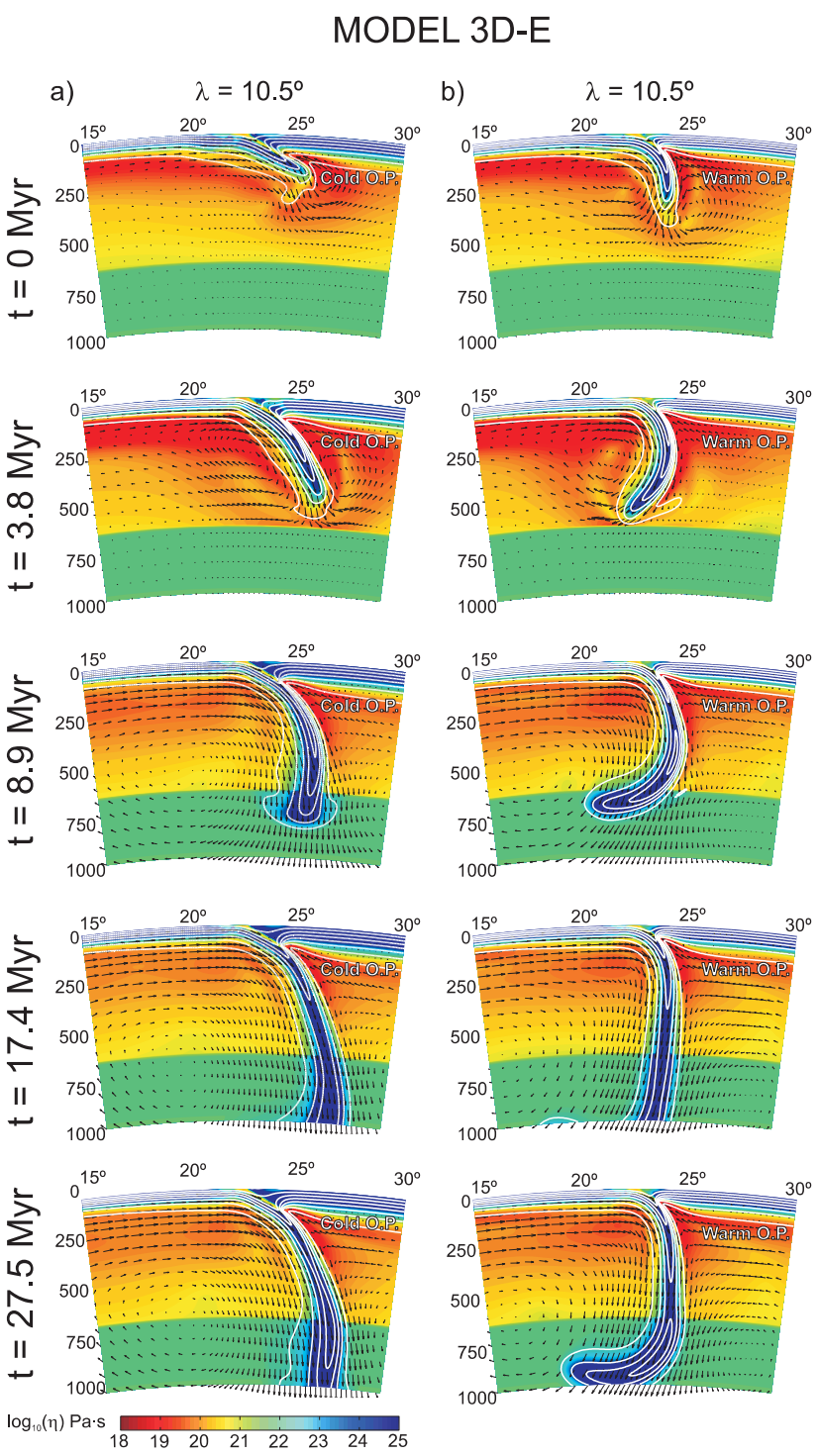

Figure 5.13: Evolution of Model 3D-E (Table 5.1) with time. Vertical sections at five different time-steps taken at two different latitudes: a) λ = 10.5º and b) λ = -10.5º. Colors, contours and arrows are the same as in Figure 5.6.

plate more effectively. In contrast, the plate subducts at 6.9 cm·yr^{-1} in the cold region, where the slab subducts flatly. As the simulation evolves the northernmost portion of the plate (Figure 5.14.a) continues to subduct flatly driven by the force provided by the steeper segment. Pull force provided by the step portion also causes the flat segment to steepen from south to north leading to a narrower flat segment. After 9.2 Myr of evolution most of the slab is vertical, but the remaining flat segment couples to the overriding plate (Figure 5.14.a), dramatically reducing the velocity of the plate in this region (Figure 5.12.c). This leads to a situation in which the southernmost portion of the slab, which is steeper, is trying to drag the northernmost portion, which is stuck due to coupling. As a consequence, the slab starts tearing beneath the cold portion of the overriding plate (Figure 5.15).

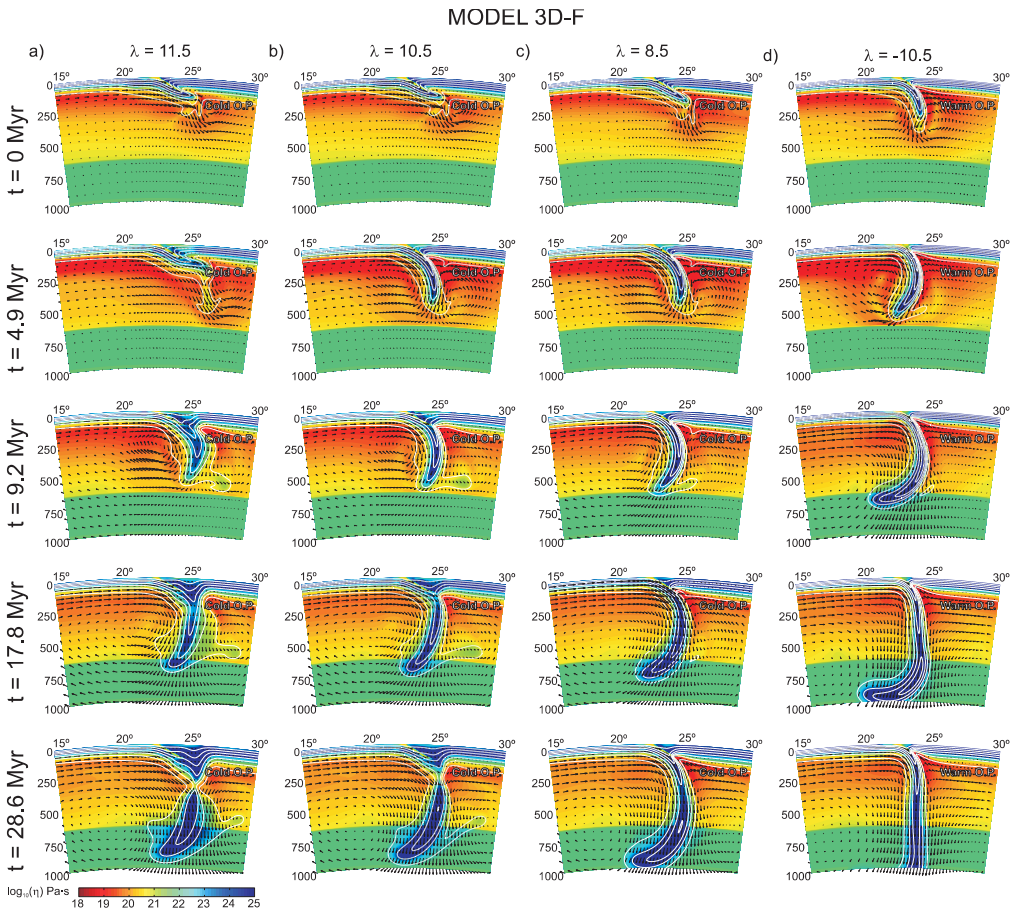

Figure 5.14: Evolution of Model 3D-F (Table 5.1) with time. Vertical sections at five different time-steps taken at four different latitudes: a) λ = 11.5º, b) λ = 10.5º, c) λ = 8.5º, d) λ = -10.5º. Colors, contours and arrows are the same as in Figure 5.6.

In this model the computed slab dip shows variations as it evolves, but is different from Models 3D-D and 3D-E (Figure 5.8.d). After 17.8 Myr, as the subduction velocity is very low, the flow in the mantle wedge is rather weak, causing the hydrodynamic suction to decrease. This leads to rapid steepening of the slab beneath the colder portion of the overriding plate in the north. After 28.6 Myr, when the slab in the cold region is detaching from the plate, it is not possible to compute the slab dip, so it is not defined in that region. At that moment, the variations of the dip for the rest of the slab are lower than 10º. The final evolution of the northern edge of the slab is clearly affected by the free-slip (reflecting) side-wall boundary conditions. Note that this evolution here should be envisaged as representative for the center of a long slab that continues as a mirror image outside the model domain.

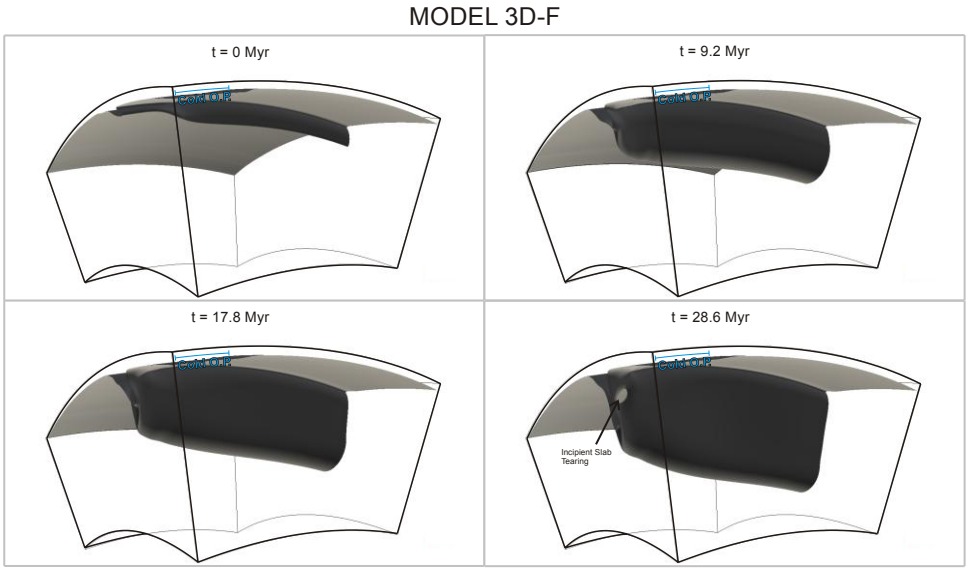

Figure 5.15: 3D plot of the 1100ºC isosurface or Model 3D-F at four different evolution times.

5.3.3. Dynamically-driven models: Uniform initial slab-dip

Results from the previous section show that the increased suction beneath the cold portion of a non-uniform overriding plate is capable of maintaining initial slab dip variations along the trench through time. The next step is to analyze whether increased suction in a portion of the slab is also able to produce these variations from an initially uniform slab dip. Therefore, we develop the next

set of models in which we test the effect of a non-uniform overriding plate on a uniform proto-slab, trying to determine if variations of the thermal state of the overriding plate along the trench are capable of triggering slab dip variability by themselves.

Model 3D-G (Figure 5.16 and Video 5.G) is started from a solution of Model 3D-A after 9.0 Myr where a portion 5.5º wide of the originally warm overriding plate is replaced by a very cold portion (970ºC at 100 km deep). This way the initial proto-slab has a uniform dip of around 70º but the overriding plate is colder on the north. Right at the beginning of the simulation an interesting feature is noticed when looking at the horizontal velocity at 300 km deep. Figure 5.17.a shows that a toroidal cell develops in the region where the overriding plate changes its thermal state. This cell, with a clockwise rotation when viewed from above, appears due to the difference in the hydrodynamic suction in this region.

After 4.4 Myr, the slab dip beneath the cold portion of the overriding plate diminishes due to the increased suction in the region, and α_s reaches values of 42º (Figure 5.16.a). At the same time the slab dip beneath the warm portion of the overriding plate does not changes and remains at 70º (Figure 5.16.b). This yields a shallow slab dip variation of up to almost 30º in the first 100 km (Figure 5.18.a). At this point the slab reaches a deeper portion and the deep slab dip does not show great slab dip variability yet and it has values between 100º and 110º.

At 4.4 Myr, when looking at the horizontal velocity at 300 km deep (Figure 5.17.b) we notice that the toroidal cell is now more intense due to the variations in the slab geometry, which is steep in the south but has a lower dip in the north. This cell contributes to further deform the slab enhancing the slab dip variability in this region. Also, the appearance of this kind of toroidal cell generates an intense trench parallel flow away from the slab edges that reaches velocities of more than 5 $cm \cdot yr^{-1}$ above the slab (to the right) and 1 $cm \cdot yr^{-1}$ beneath it. The flow in the mantle wedge shows sudden variations on its directions, in good agreement with observations of mantle flow derived form seismic anisotropy.

After 8.9 Myr the slab reaches the lower mantle and the dynamics slightly change. Due to the partial support of the more viscous lower mantle the slab dip in the warm region remains approximately constant for the shallowest portion (α_s), but the deepest portion (α_d) decreases, reaching values of 80º after 9.6 Myr

and 90º after 18.2 Myr (Figure 5.18.a). Beneath the coldest portion of the overriding plate α_s is still lower than beneath the warmest portion, and reaches values between 45º and 50º, making the slab dip variations close to 20º. The velocity shows a similar behavior compared to Model 3D-E, increasing as the slab lengthens, but slowing down once the slab reaches the lower mantle and remains uniform (Figure 5.11.d).

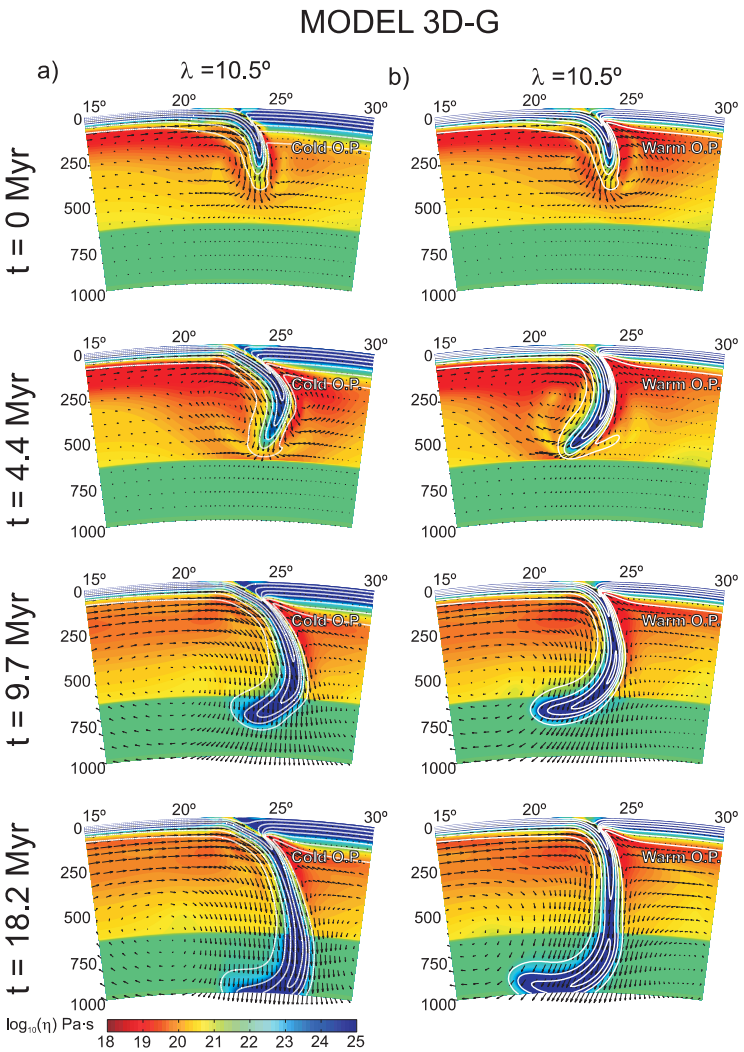

Figure 5.16: Evolution of Model 3D-G (Table 5.1) with time. Vertical sections at four different time-steps taken at two different latitudes: a) λ = 10.5º b) λ = -10.5º. Colors, contours and arrows are the same as in Figure 5.6.

Model 3D-H (Figure 5.19 and Video 3D-H) is started form a solution of Model 3D-A after 9.0 Myr where a portion of 12.5º (half of the width of the model) of the originally warm overriding plate is substituted by a very cold

portion T_{100}=970 ºC. Therefore, the only difference between Models 3D-G and 3D-H is that the cold portion of the overriding plate is wider in 3D-H. The behavior of this model is similar to that of Model 3D-G and α_s is lower beneath the coldest portion of the overriding plate (Figure 5.19.a), therefore, the portion of reduced slab dip is wider in this model. After 5.6 Myr, in the cold region, the shallow slab dip reaches values of around 45º, and remains approximately stable with time (Figure 5.18.a). In the warm region the slab dip also varies only a few degrees (less than 10º in the overall process) showing a slight steepening at the beginning until the slab reaches the lower mantle, at about 6 Myr, when the slab dip slightly decreases. The variations of the shallow slab dip along the trench during the process are always close to 25º.

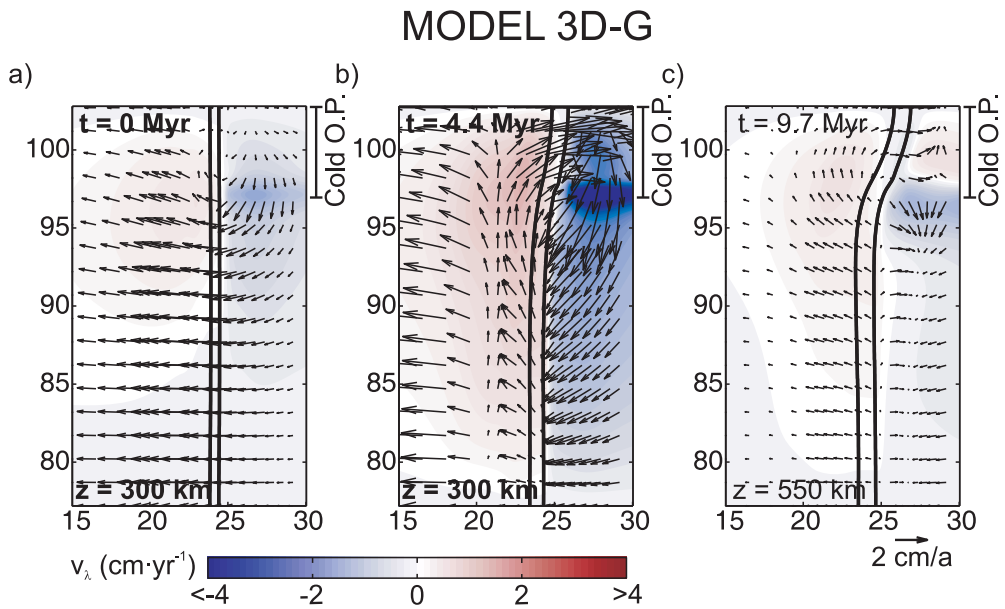

Figure 5.17: Map view of the velocity field of Model 3D-G at different depths and time-steps. a) Initial state at 300 km deep; b) after 4.4 Myr at 300 km deep; c) after 9.7 Myr at 550 km deep. The velocity parallel to the trench (color), the location of the slab (black isotherm at 900K) and velocity field (arrows) are shown. The slab subducts from left to right.

During the process α_d also decreases when the slab reaches the lower mantle, but deep slab dip variations along the trench are more complex. After 5.6 Myr there are not great variations in the slab dip. After 11.1 Myr the differences in the slab dip reach values of 15º and the greatest variations are found beneath the transition from cold to warm overriding plate (now in the center of the modeled region). After 19.6 Myr the model presents the highest variations in the slab dip at deep regions, reaching values of around 25º.

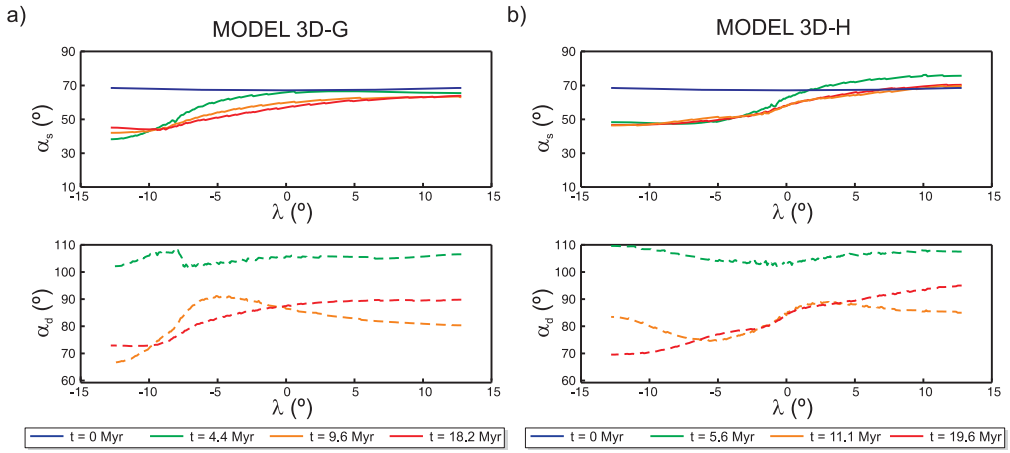

Figure 5.18: Variations of the slab dip along the trench computed at different depths and time-steps. a) Model 3D-G. b) Model 3D-H.

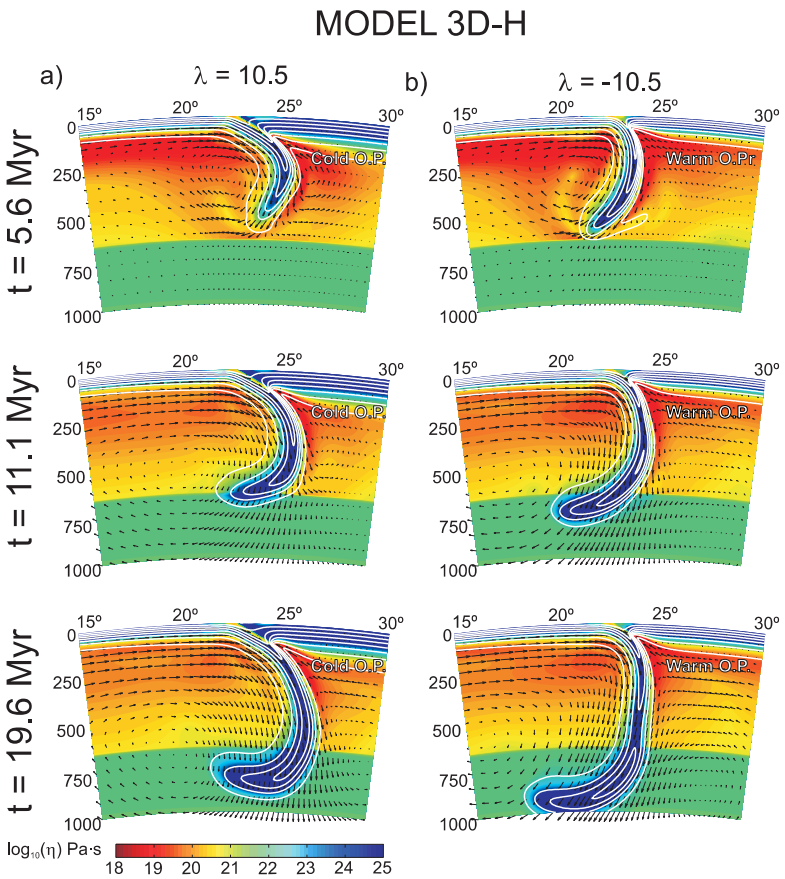

Figure 5.19: Evolution of Model 3D-H (Table 5.1) with time. Vertical sections at three different time-steps taken at two different latitudes: a) λ = 10.5° and b) λ = -10.5°. Colors, contours and arrows are the same as in Figure 5.6.

To explain this behavior it is interesting to take a look at the horizontal velocity at different depts. As before, at the beginning of the simulation, a toroidal cell appears beneath the transition from cold to warm overriding plate (Figure 5.20.a). After 5.6 Myr this cell is more intense due to variations of the slab geometry and the hydrodynamic suction (Figure 5.20.b) and contributes to further deform the slab. As a consequence, at 550 km deep the maximum deformation is localized beneath where the overriding plate changes its thermal state (Figure 5.20.c) and presents a more complex geometry (Figure 5.21), whereas in Model 3D-G the plate presented a much simpler geometry (Figure 5.17.c).

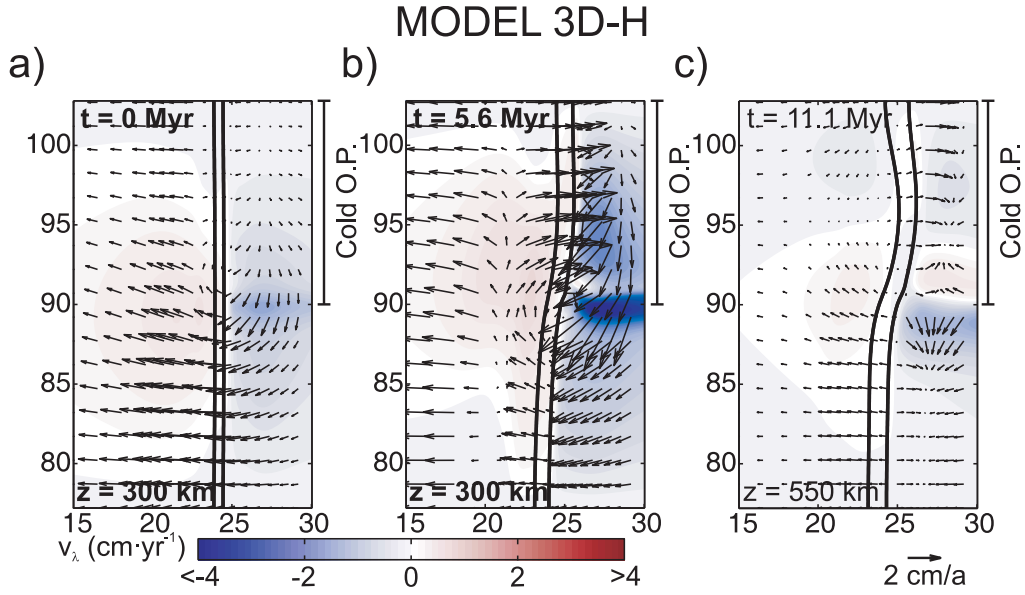

Figure 5.20: Map view of the velocity field of Model 3D-H at different depths and time-steps. a) Initial state at 300 km deep; b) after 5.6 Myr at 300 km deep; c) after 11.1 Myr at 550 km deep. Colors and arrows are the same as in Figure 5.17.

The growth of the toroidal cell also generates an intense trench-parallel flow, but in this case, as the toroidal cell is located in the center of the modeled domain, the region where trench-parallel flow appears above the slab is wider (around 10º). The trench-parallel component of the flow reaches values close to 4 $cm \cdot yr^{-1}$ near the region where the thermal state changes (away from the edges) and of 1 $cm \cdot yr^{-1}$ close to the edge of the model. Similarly to Model 3D-G, the trench parallel flow shows a complex pattern in the mantle wedge.

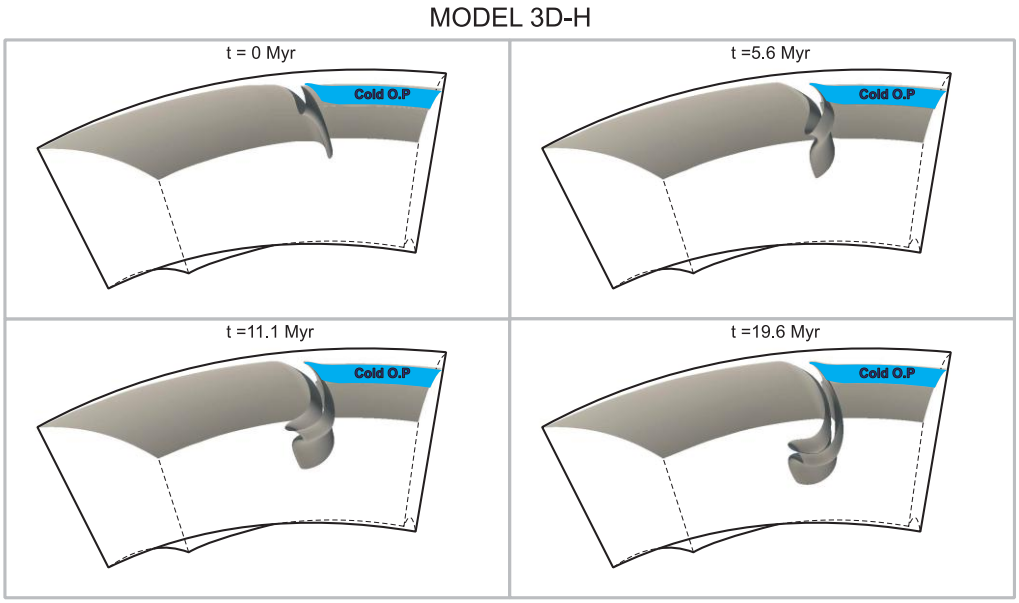

Figure 5.21: 3D plot of the 1100ºC isosurface of Model 3D-H at four different evolution times.

5.3.4. Dynamic models: Uniform initial slab-dip and lateral plates

One of the most important results from the previous section is the appearance of toroidal cells and trench parallel flow and how this affects the geometry of the slab. It is therefore important to study how the results change if we allow for the material to flow around the edges of the slab, as this might change the flow pattern in the models.

Model 3D-I (Figure 5.22 and Video 5.I) is a dynamically-driven model started from a solution of Model 3D-A after 9.0 Myr, keeping the overriding plate uniform, and lateral plates 10º wide, with the same thermal state as the overriding plate, are added on each side of the model (Figure 5.4.b). Therefore, this model is similar to Model 3D-D but with lateral plates. The addition of these two plates allows us to separate the lateral (northern and southern) boundaries of the model from the edges of the slab, which allows the material to flow around them. The evolution of the slab in this model is similar to the evolution of Model 3D-D, showing an initial increase of the subduction velocity, followed by a decrease of the velocity of the subducting plate after slab penetration into the lower mantle (Figure 5.11.f). The results also show a reduction of the slab dip

(Figure 5.23.a) once the slab reaches the lower mantle, and α_s changes from around 70º to 55º, and α_d from 100º to 80º. As in Model 3D-D, the velocity of the plate is uniform, but in this case is much higher, reaching values of more than 17 cm·yr^{-1} (Figure 5.24.a).

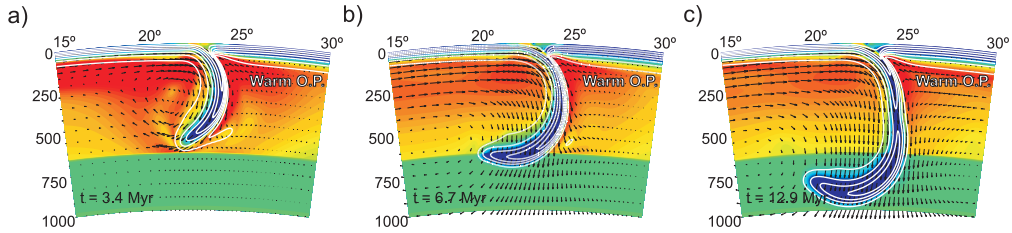

Figure 5.22: Evolution of Model 3D-I (Table 5.1) with time. (a-c) Vertical sections at three different time-steps. Colors, contours and arrows are the same as in Figure 5.6.

The main difference between these two models is appreciated when looking at some horizontal sections. Initially, at 300 km (Figure 5.25.a) the horizontal velocity shows two toroidal cells, one on each side of the slab. These cells appear due to the roll back motion of the slab in the initial stages. These cells are symmetrical and after 3.4 Myr are more intense (Figure 5.25.b). This toroidal flow contributes to deform the slab at the edges, which after 6.3 Myr leads to a slightly curved slab that can be appreciated at 500 km deep (Figure 5.25.). This is also seen in the slab dip, which presents small variations that reach values of less than 10º (Figure 5.23.a). The retreating of the slab generates trench parallel flow beneath the slab (Figure 5.25.b) with values of 2 cm·yr^{-1}.

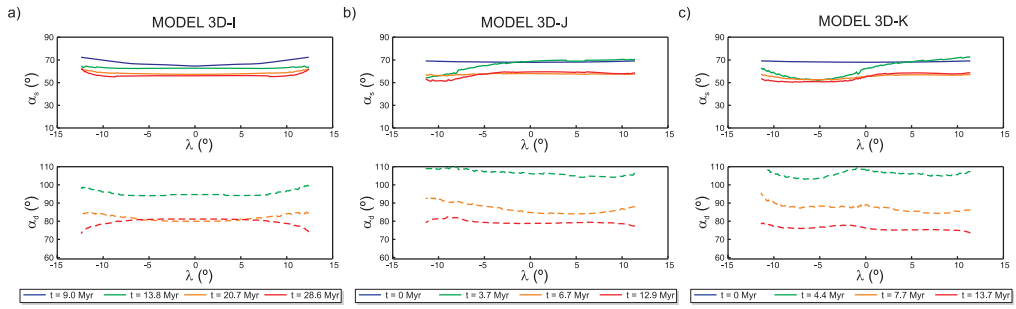

Figure 5.23: Variations of the slab dip along the trench computed at different depths and time-steps. a) Model 3D- I. b) Model 3D-J. c) Model 3D-K.

Model 3D-J (Figure 5.26 and Video 5.J) is started form the solution of Model 3D-A after 9.0 Myr of evolution, when a portion 5.5º wide of the

originally warm overriding plate is replaced by a very cold portion (T_{100}=957 ºC). As in the previous model lateral plates of 10º, with the same thermal state of the warm portion of the overriding plate, are added on each side of the model. Therefore, Model 3D-J is similar to Model 3D-G but with lateral plates, and is similar to Model 3D-I but with a colder portion of the overriding plate to the north. The dimensions of this model mimic the subduction of the Cocos plate. The evolution of the slab dip in this model is similar to that of Model 3D-I, and the slab dip variations found in Model 3D-G diminish and are now subtle (Figure 5.23.b) reaching a maximum difference of 15º for α_s and not even 10º for α_d. The evolution of the mean velocity of the subducting plate with time is also similar to Model 3D-I (Figure 5.11.g), but now is not uniform (Figure 5.24.b) and at 3.7 Myr the mean velocity in the cold region is 11.9 cm·yr^{-1} and in the warm region is 14.6 cm·yr^{-1}.

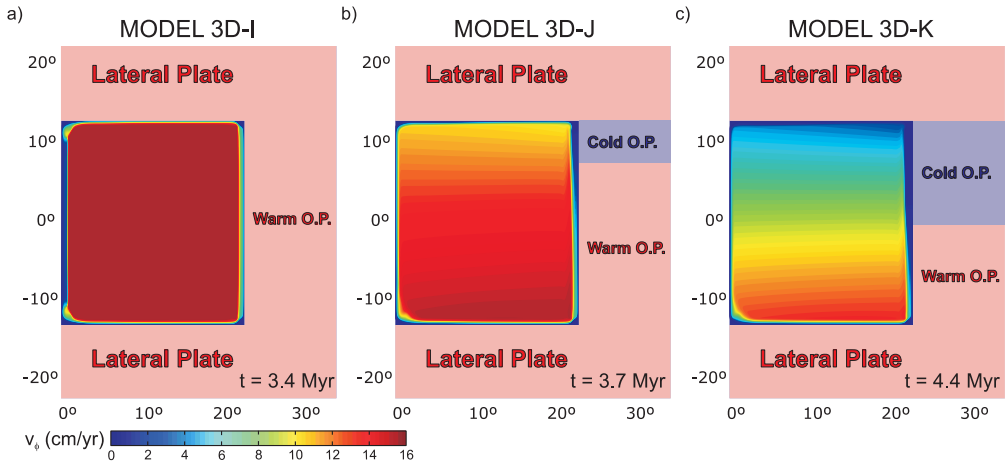

Figure 5.24: Map view of the surface velocity for the subducting plate of the dynamically-driven models with lateral plates 3D-I (a), 3D-J (b) and 3D-K (c).

At the beginning of the simulation the horizontal velocity (Figure 5.26.a) shows two toroidal cells at the edges of the slab, but in this case, the cell beneath the warmest portion of the overriding plate is wider and more intense than under the cold portion. After 3.7 Myr that same cell grows and a wide area of trench-parallel flow develops beneath the slab with values of 4 cm·yr^{-1}. The reduction of slab dip variations can be explained by means of the hydrodynamic suction: as the material is now allowed to flow around the edges of the slab, it moves towards the edge in the trench-parallel direction, which reduces the

intensity of the corner flow in the mantle wedge, which in turn reduces the hydrodynamic suction and the slab does not flatten.

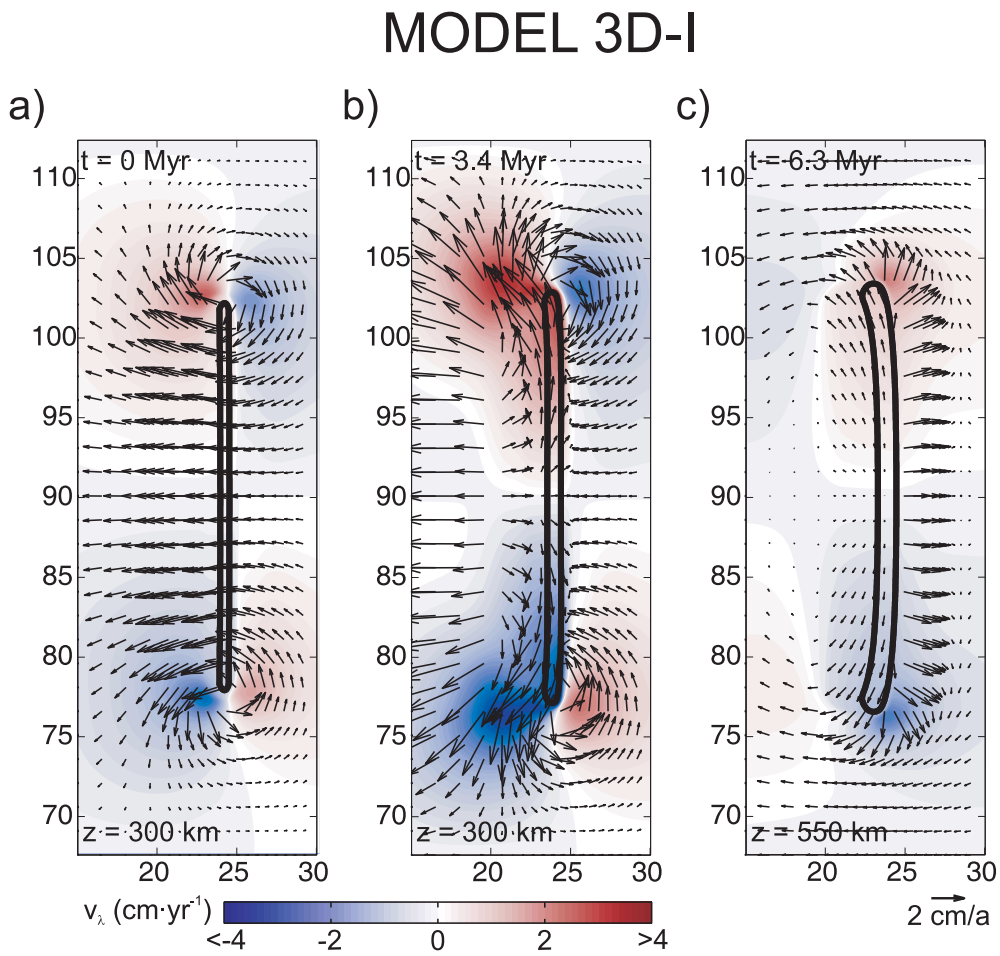

Figure 5.25: Map view of the velocity field of Model 3D-I at different depths and time-steps. a) Initial state at 300 km deep; b) after 3.4 Myr at 300 km deep; c) after 6.3 Myr at 550 km deep. Colors and arrows are the same as in Figure 5.17.

Model 3D-K (Figure 5.27 and Video 5.K) is started form a solution of Model 3D-A after 9.0 Myr, when a portion 12.5º wide (half of the width of the model) of the originally warm overriding plate is substituted by a very cold portion (T_{100}=970 ºC). As in the previous model lateral plates 10º wide are added on each side of the model. This model is similar to Model 3D-H but with lateral plates or similar to Model 3D-J but with a wider cold portion of the overriding plate. The evolution of the slab dip in this model is similar to those of Models 3D-I and 3D-J, and the variations of the slab dip are much lower than in the equivalent model without lateral plates (Model 3D-H). However, slab dip

variations along the trench are higher than in Model 3D-J, reaching a maximum difference of 20º for α_s (Figure 5.23.c). The evolution of the mean velocity of the subducting plate follows the same trend as in previous models (Figure 5.11.h) but now shows a great non-uniformity, increasing gradually from about 13 cm·yr^{-1} in the northern part to about 4 cm·yr^{-1} in the southern one at 4.2 Myr (Figure 5.24.c). Also, the overall velocity is much lower that in Model 3D-I and 3D-J as the increased suction beneath the cold portion of the overriding plate is slowing down the plate.

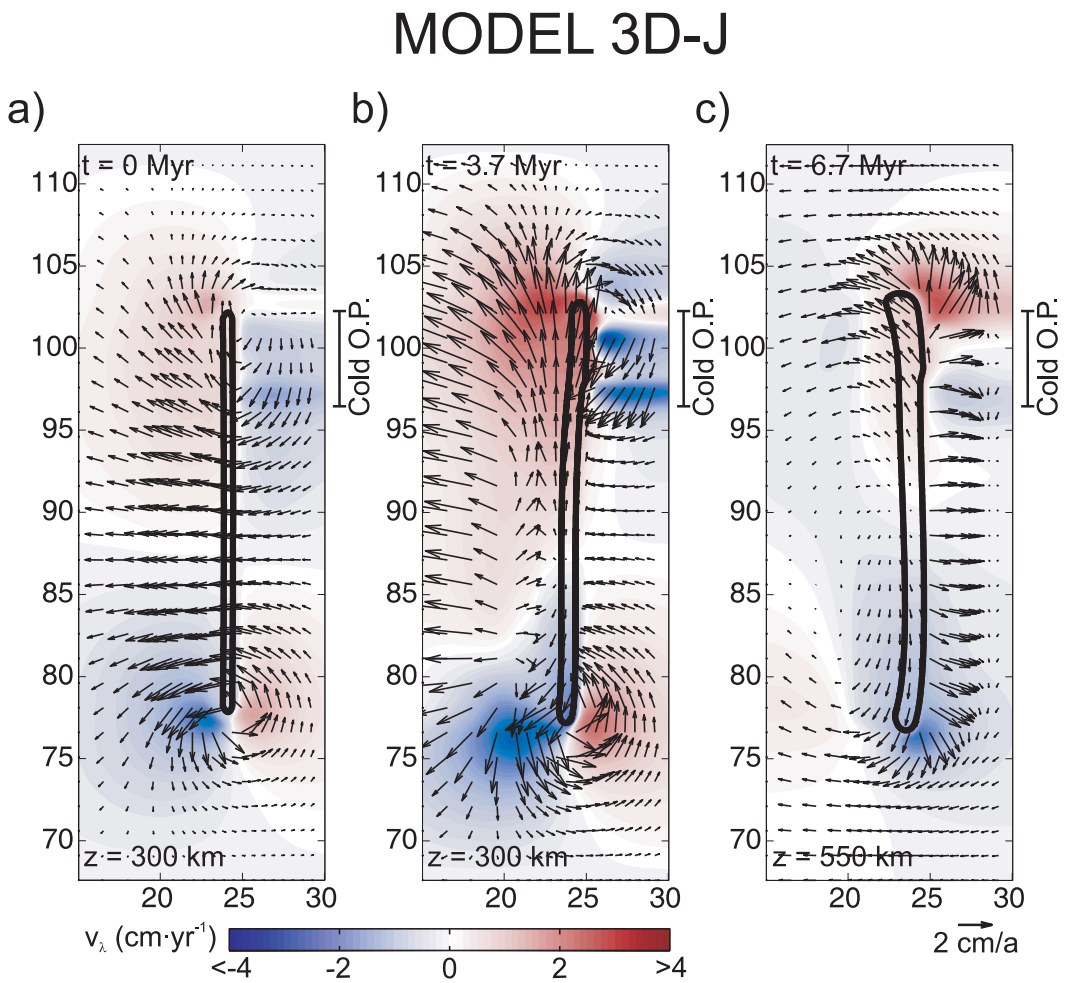

Figure 5.26: Map view of the velocity field of Model 3D-J (Table 5.1) at different depths and time-steps. a) Initial state at 300 km deep; b) after 3.7 Myr at 300 km deep; c) after 6.7 Myr at 550 km deep. Colors and arrows are the same as in Figure 5.17.

At the beginning of the simulation the horizontal velocity (Figure 5.27.a) is similar to that of Model 3D-J but now the toroidal cell beneath the cold portion of the overriding plate is much wider than the toroidal cell beneath the warm

portion. After 4.2 Myr (Figure 5.27.b) the cell in the cold region becomes more intense, and there is a wide region of trench-parallel flow beneath the slab, where velocities reach values of 3 cm·yr^{-1}. Also a wide region of trench-parallel flow develops above the slab, where the velocities are lower, but reach values of about 1 cm·yr^{-1}. Also in the mantle wedge, the induced flow shows a complex pattern with sudden changes in the direction and velocities up to 3 cm·yr^{-1}. At this point, the deformation of the slab is greater than in Model 3D-J. After 7.7 Myr, at 550 km deep (Figure 5.27.c), the slab also shows more deformation than Model 3D-J, but still less than the equivalent model without lateral plates (Model 3D-H). As in Model 3D-J, the addition of the lateral plates is responsible for the reduction of the variations of the slab dip and the increase of trench-parallel flow, as the material is now allowed to flow around the edges of the slab.

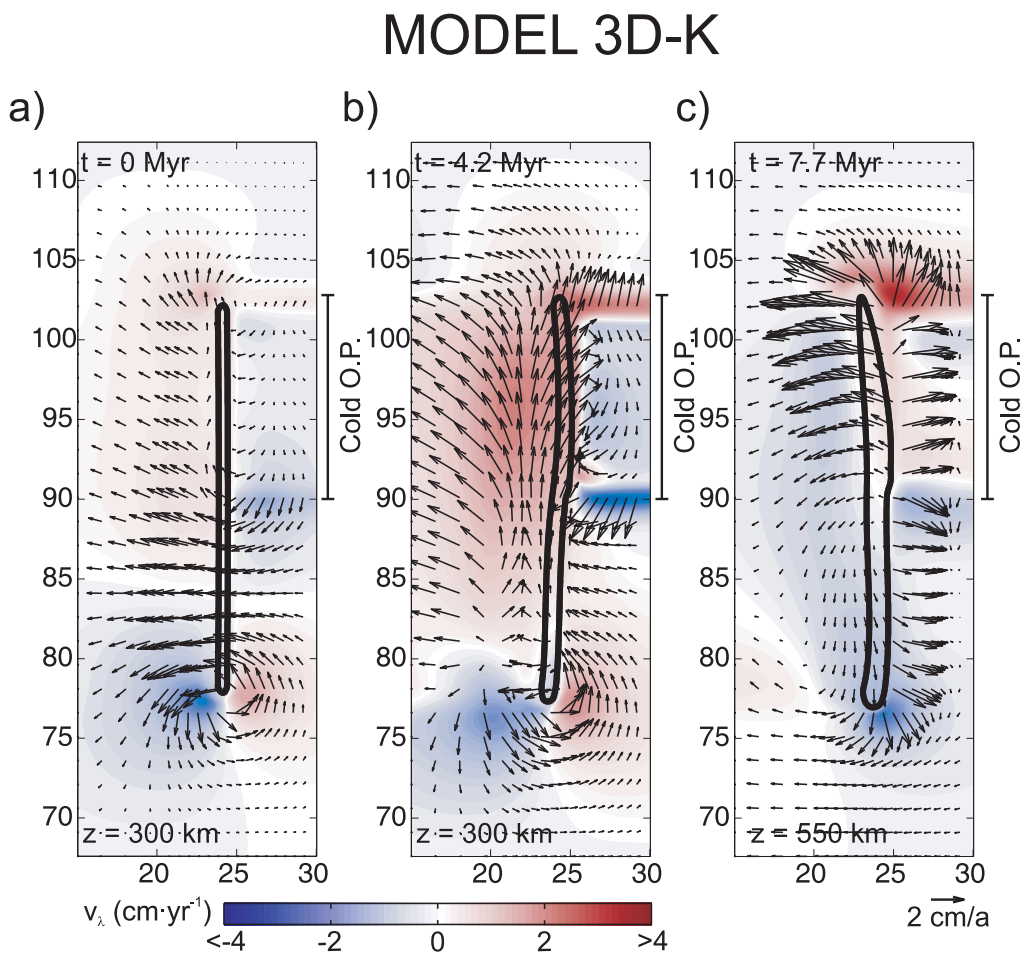

Figure 5.27: Map view of the velocity field of Model 3D-K (Table 5.1) at different depths and time-steps. a) Initial state at 300 km deep; b) after 4.2 Myr at 300 km deep; c) after 7.7 Myr at 550 km deep. Colors and arrows are the same as in Figure 5.17.

5.4. Discussion

The 3D models presented here show coherent results, but still show significant differences among them. Kinematically-driven models with a non-uniform overriding plate (3D-B and 3D-C) and dynamically-driven models with a non-uniform initial slab dip (Models 3D-E and 3D-F) show greater slab dip variations than dynamically-driven models with uniform initial slab dip (Models 3D-G and 3D-H) during the first stages, but as the simulations evolve, slab dip variations along the trench in these different models become similar. The slab dip variability is minimum for models with lateral plates (Models 3D-J and 3D-K). Also, in absolute terms, the slab dip is greater for models with a uniform initial slab dip (Models 3D-D, 3D-G, 3D-H and 3D-I through 3D-K).

We show that lateral variations in the thermal state of the overriding plate are able not only to maintain slab dip variations along the trench as large as 30º through time, but also to create them from an initially uniform proto-slab dip. This contorted geometry of the slab is shown to generate a strong component of trench-parallel mantle flow, both above and below the slab, particularly in the region of change of overriding plate thermal state. This result is in agreement with mantle flow inferred from seismic anisotropy (Figure 5.2), showing uniform trench-parallel flow beneath the slab and complex flow patterns in the mantle wedge. In particular results are in agreement with the interpreted southward asthenospheric flow to the south of the Sierras Pampeanas flat slab (often called central Chile flat slab) region (*Anderson et al.*, 2004). Trench parallel flow in the mantle wedge beneath Costa Rica and Nicaragua has been inferred from isotope geochemistry, seismic velocity attenuation and anisotropy data (*Hoernle et al.*, 2008). In addition, we show that slab contortions created in a self consistent way (instead of being kinematically imposed), thus in response to the momentum balance, strongly modify the pattern of mantle flow and should be taken into account in interpretations of shear wave anisotropy data. In fact, the toroidal flow created in the areas of change in overriding plate thermal state could provide an explanation for sharp changes in fast seismic anisotropy directions often observed in the mantle wedge (*Long and Silver*, 2008; Figure 5.2). Differently from recent 3D numerical modeling, which predicts trench-parallel flow always associated with toroidal flow around slab edges (*Jadamec and Billen*, 2010; *Capitanio and Faccenda*, 2012; *Faccenda and Capitanio*, 2012; *Jadamec and Billen*, 2012), we show

here that slab dip variations produce trench-parallel flow also in models not allowing for flow around the slab edges. Capitanio et al. (2011) also studied the effect of a non-uniform overriding plate on trench migration rate and topography, but that study only focused on surface processes and therefore, did not observe the effect of a non-uniform overriding plate on the pattern of mantle flow. A non-uniform subducting plate does generate a significant trench-parallel component, with values around 1.5 $cm \cdot yr^{-1}$(*Capitanio and Faccenda*, 2012). In contrast, our results show that a non-uniform overriding plate is capable of generating a much more intense trench-parallel flow, with values up to 4 $cm \cdot yr^{-1}$. Jadamec and Billen (2010, 2012) showed that slabs with a variable geometry induce very localized super-fast velocities (up to 80 $cm \cdot yr^{-1}$), but such high velocities are not found in our results. This is probably due to the fact that they used a minimum allowed viscosity of 10^{18} Pa·s, which is lower than the value used in our models (η_{min}=1019 Pa·s), as lower minimum viscosity allow for faster velocities.

The dimensions of the models with a 5.5º wide cold portion of the overriding plate mimic the dimensions of the subduction of Cocos plate beneath the North America and Caribbean Plates (See section 3.4). Results from these models show that variation of the thermal state of the overriding plate is a plausible explanation for the slab dip variability in this area, even when the cold portion of the overriding plate is narrow. The flat segment beneath the central Andes (Peru flat slab) has been explained before in terms of the "lost Inca Plateau", already subducted (*Gutscher et al.*, 1999), but no clear evidence of that plateau has yet been found. Therefore, variations of the thermal state of the overriding plate provide a plausible explanation also in this region. In other regions, such as the narrow flat slab in Sierras Pampeanas, the presence of flat subduction has been proposed to be related to the subduction of an aseismic ridge (in this case Juan Fernandez Ridge) (*Gutscher et al.*, 2000b; *Anderson et al.*, 2007), but numerical models show that a ridge subducting perpendicular to the trench is not buoyant enough to generate a flat slab (*Gerya et al.*, 2009). The presence of a colder overriding plate at the moment of the subduction of the ridge provides a new plausible explanation, as the increased hydrodynamic suction would favor the formation of a flat slab. It is worth noting that a clear correlation between the occurrence of flat subduction and the proximity to areas of high elastic thickness (likely cold areas) has been obtained for both the Peru

and Sierras Pampeanas flat subduction zones (*Pérez-Gussinyé et al.*, 2008; Figure 5.1a).

A simplification assumed in this modeling is that the trench is fixed in all the models, which limits the deformation of the slab, especially in shallow regions. If the trench were free to move, we would expect more deformation both due to the toroidal flow in the edges of the slab and the increased hydrodynamic suction beneath the cold portion of the overriding plate. On the basis of previous work considering variable thickness of the overriding plate (*Capitanio et al.*, 2011), we expect trench migration rates to be affected by the thermal state of the overriding plate, leading to curved trenches.

Slab dip variations predicted by our models are significantly reduced when lateral plates are added, although shallow slab dip variations of about 20º are still reproduced. When comparing examples in nature with these results it is important to take into account that models with lateral plates, allowing for flow around the edges, are not necessarily more realistic. Instead, models with lateral plates are appropriate to represent isolated subduction zones, whereas models without lateral plates would better represent subduction zones surrounded by other slabs, where flow around the edges of the slab is not permitted.

A remarkable new result obtained in this modeling is that the increased hydrodynamic suction under the cold portion of overriding plate is able to produce a decrease in slab dip of about 30º in shallow regions (α_s) in only 4.4 Myr as shown by Model 3D-G (Figure 5.18.a). This mechanism of local slab shallowing or 'roll-up' and its consequences in natural examples (e.g. migration of volcanic arc) deserves further investigation. In previous works by Capitanio et al (2011) this slab flattening was not observed in the presence of a thickened overriding plate, but this is due to the fact that in their models the thermal equation is not solved and therefore, the overriding plate does not affect the viscosity structure of the mantle wedge.

Another result with significant potential implications for natural areas is incipient slab break-off after coupling between the subducting plate and cold portion of the overriding plate (Model 3D-F). We suggest that this process could represent an alternative mechanism for slab break-off, possibly acting in areas where other mechanisms such as slab break-off after continental collision (*van*

Hunen and Allen, 2011) and after ocean ridge subduction (*Burkett and Billen*, 2009) are excluded. We speculate that this process of break-off after plate coupling could be responsible for break-off of the very shallow angle subducting Farallon plate, which has been proposed to occur when the plate becomes coupled to the edge of the North American craton (*Sigloch et al.*, 2008). Similarly, this slab tearing associated to plate coupling could be responsible for break-off of greater India lithosphere subducting under the thickened Tibetan lithosphere (e.g., *Replumaz et al.*, 2010).

5.5. Conclusions

We have developed 3D thermal mechanical models that account for features with a potential influence on the 3D slab geometry and on the pattern of mantle flow. These features are along-trench variations of the thermal state of the overriding plate and the possibility of having trench-parallel and toroidal mantle flow.

Results for kinematically-driven models with a non-uniform overriding plate show that the subducting plate is affected locally by the different hydrodynamic suction, which leads to along-trench variations of slab dip.

Models of dynamically-driven subduction indicate that the increased suction beneath the cold portion of the overriding plate is enough to maintain preexisting variations of the slab dip. Moreover, this variable suction is shown to be even able to deform an initially uniform slab, creating significant variations on the slab dip along the trench. Due to the variations on the hydrodynamic suction and slab geometry, intense toroidal cells are generated in the region where the thermal state changes. These cells produce a component of trench-parallel flow far away from the edges of the slab, and not related to mantle flow around them.

We infer that the presence of very cold areas in the overriding plate (e.g. cratons) can lead to complete coupling between overriding and subducting plates along segments of the plate boundary and to subsequent slab tearing.

Adding lateral plates to 3D models enables the material from the mantle to flow around the edges of the slab, which leads to wide regions of intense trench-parallel flow both beneath and above the slab. This trench-parallel flow has

values between 1 and 4 $cm \cdot yr^{-1}$. The flow in the mantle wedge shows a complex pattern with sudden variations in the direction of the flow and the magnitude of the velocity.

6

CONCLUDING REMARKS AND FUTURE WORK

6.1. General Conclusions

Mechanisms controlling subduction dynamics and the resulting slab geometry are not yet fully understood. Even though many numerical and laboratory experiments, together with compilations of data, have lead to significant advances in understanding subduction dynamics and related consequences, there are still many questions that need to be answered. The work developed in this thesis addresses some of these questions and allows us to improve our knowledge about subduction processes by means of 2D and 3D numerical modeling.

In order to test the influence of the thermal state of the overriding and subducting plates on the dynamics and geometry of subduction, we have developed 2D numerical models using the commercial software Comsol Multiphysics. We have carried out a systematic study in which we vary separately the age of both plates.

Our results indicate that, as expected, a higher gravitational torque is exerted on older subducting plates due to their increased negative buoyancy. As a consequence, older subducting plates start subducting with a higher angle than young plates. The gravitational torque increases with time until it reaches a period of stabilization in which it barely changes. Therefore, the influence of the thermal state of the subducting lithosphere is only significant during the first stages of subduction, and diminishes with time, as slab geometry tends to reach steady state.

The mantle beneath older overriding plates is colder and more viscous, and therefore, the hydrodynamic suction on the upper surface of the slab in the mantle wedge is higher. Therefore, plates subducting underneath cold overriding plates are predicted to subduct with lower slab dip, due to the increased suction torque. The slab dip is a result of the competing effects of the gravitational and suction torques. The lower viscosity beneath warmer overriding plates triggers thermal erosion in the mantle wedge that causes the warm material to migrate upwards. This contributes to further reduce the hydrodynamic torque, leading to steeper slabs. The influence of thermal state of the overriding plate on slab dip can have a noticeable effect even for long evolution times. This study

demonstrates that the influence of thermal state of the overriding plate on slab dip is more important than that of the subducting plate, and persists for long-term evolution.

We have shown that the thermal state of the overriding and subducting plates has an important effect on the slab geometry independently of other factors. We have run tests for weaker slabs, faster and slower subducting plates and even for different initial dips (by changing the inclination of the weak zone at the plate boundary), and all the results show the same trends: older plates subduct with higher dips during initial stages and subduction beneath older overriding plates takes place at lower dips. We have also shown that the qualitative effects of the thermal state of the overriding plate is independent of the amount of coupling between both plates, and that trench perpendicular variations in the temperature of the overriding plate also have a great influence on slab geometry.

With simple 2D models, varying only the age of the subducting and overriding plates we have been able to reproduce a wide range of slab geometries and different styles of subduction such as high-angle subduction, low-angle subduction and coupled slabs. We have even been able to reproduce long slab segments that subduct flatly for a limited period of time.

Another factor controlling the dynamics of subduction is an external horizontal mantle flow. In order to study its effect on the slab geometry, we have added to our previous 2D models a horizontal flow acting in both senses (opposing and accompanying subduction) and with different velocities.

The mantle flow is shown to have little influence on the geometry of the slab for the early stages of subduction. For longer evolution times, as the slab sinks deeper into the mantle, the flow is channeled between the tip of the slab and the more viscous lower mantle, and flow velocity increases. Therefore, the effect of the horizontal mantle flow becomes stronger and, if the mantle flow has the opposite sense to subduction, the resulting slab dip will be higher. On the contrary, if the mantle flow has the same sense as subduction, the slab flattens with time. For very long evolution times, once the slab has reached the lower mantle, the slab dip is reduced so much that the overriding and the subducting plates become coupled and subduction stops.

We have also developed 3D models using CitcomS, and we have included more realistic geometry (using spherical coordinates), boundary conditions (allowing for self-driven subduction) and rheology (implementing a pseudo-plastic behavior). With these models we aim to generalize the results from 2D models and to study the different behavior derived form 3D features (e.g., along-trench variations of the thermal state of the overriding plate or trench-parallel and toroidal flow).

First, these new models showed that conclusions drawn from 2D models are also valid with the new configuration. If the overriding plate is not uniform but has two regions with different thermal states, the hydrodynamic suction is greater beneath the coldest portion. The subducting plate is affected locally by the different hydrodynamic suction, which leads to along-trench variations of slab dip, because these variations are greater for greater temperature differences.

If the subduction is dynamically-driven slabs tend to sink vertically, but the increased suction beneath the cold portion of the overriding plate is enough to maintain preexisting variations of the slab dip. The variable suction in the mantle wedge is even able to deform the initially uniform slabs, creating significant variations on the slab dip along the trench. Also, due to the variations on the hydrodynamic suction and slab geometry, intense toroidal cells are generated in the region where the thermal state changes. This toroidal flow contributes to increase the deformation of the slab, and also causes the appearance of trench-parallel flow far away from the edges of the slab.

Adding lateral plates to 3D models enables the material from the mantle to flow around the edges of the slab. This leads to the formation of toroidal cells in the edges of the slab. Allowing the material to flow around the edges of the slab together with variations of the thermal state of the overriding plate, leads to wide regions of intense trench-parallel flow both beneath and above the slab. Beneath the slab the flow show a simple pattern with a wide region of uniform trench parallel flow with values around 3 $cm \cdot yr^{-1}$. In the mantle wedge the flow shows a much complex pattern with sudden variations of the flow direction an the velocity magnitude, presenting values between 1 and 3 $cm \cdot yr^{-1}$.

Finally, we compare our modeling predictions, in qualitative terms, with some subduction zones that show slab dip variability along the trench, as the

subduction of Cocos Plate or subduction in South America, where a wide flat slab segment is found beneath Peru and a narrow flat segment I subducts in Northern Chile. Regarding Cocos Plate, we provide a plausible explanation for this variability in terms of the change of the thermal state of the overriding plates, with flat and low-angle subduction occurring under the cold lithosphere of the Maya block of North America and steep subduction under the warmer lithosphere of the Chortis block of the Caribbean plate. We suggest that the flat segment in Peru can be explained in terms of the proximity of the area of increased elastic thickness and reduced heat flow in the region.

6.2. Future work

The results drawn from 2D and 3D models show that still some improvements should be made to the model setup and data analysis. First, it would be important to calculate the Lattice Preferred Orientation derived from the flow pattern of 3D models. This would allow us to compare the model results with observations of shear wave splitting data from particular subduction zones such as Central and South America.

It is also important to add new features to the models, especially to the three dimensional ones. The first point that should be addressed is the implementation of a mobile trench. A low viscosity layer on top of the subducting plate would substitute the low viscosity channel at the plate boundary. If this layer were advected using tracers, it would act as a decoupling layer but would also move with the plates, allowing the trench to migrate. A free moving trench would allow us to study the relationship between trench migration rates and variations on the thermal state of the overriding plate. Developing 3D models with a mobile trench will allow us to quantify the effects of mantle flow on trench motion and on the resulting stress regime in the overriding plate and slab.

In addition, another feature that should be addressed is the implementation of 3D models that include an imposed horizontal mantle flow. The horizontal mantle flow will most likely increase the toroidal and trench-parallel flow. The mantle flow might also affect the geometry of the slab but not as much as was shown by 2D models, and its influence will be less significant especially for narrow slabs.

Other features that should be added to the current setup are phase transitions and compositional differences. Phase transitions may affect the behavior of the slab when it reaches the transition zone, leading to stagnation. Studying the combined effect of variations on the thermal state of the overriding plate and the subduction of aseismic ridges and oceanic plateaus would provide important information about the causes of flat subduction.

Finally, we will develop models that will mimic other natural subduction zones to validate our results and compare the resulting slab dips and flow patterns with observations. We will set up new models with more realistic trench geometries and adding constraints of the overriding and subducting plates thermal state.

APPENDIX A
CITCOMS CONFIGURATION

CitcomS configuration options are modified through a .cfg file (ASCII text file), and example of which can be found in http://tinyurl.com/thesis-JRG (reference.cfg). Only an overview of how these options are set will be provided here, but a more detailed explanation can be found in the CitcomS manual (http://www.geodynamics.org/cig/software/citcoms/citcoms.pdf). The main features that have been modified through the different models are:

Mesh

Locally refined meshes can be used with CitcomS. To do so, an ASCII file (coord.dat found in http://tinyurl.com/thesis-JRG) must be provided. This file contains three vectors, one for each of the coordinates (θ, φ and r) specifying the location of the nodes on each direction.

Choosing the appropriate mesh is key to achieving convergence of the model. The mesh is refined in the regions where large variations of viscosity, temperature and velocity are expected and is coarsened in the rest of the domain to optimize computational resources. It is important to take into account that the transition from coarse to fine regions must be gradual, and the aspect ratio between the element sizes in two different directions must not be greater than 1:3. The mesh of the final models has either 19,902,337 nodes (257x481x161, for models without lateral plates) or 34,77,009 nodes (449x481x161 in models with lateral plates).

Solver

The solver is highly customizable. First one can choose between a Conjugate Gradient Solver and a Geometric Multi-grid Solver. We have chosen the second one for which several parameters can be modified (see section for more details on how these parameters affect the solver. First, we can choose between a V or a W cylces (we have chosen the default V cycle), second the number of levels of the multi-grid cycle (set to 4), then the number of smoothing passes for the downward and upward smoothing (set both to 16), also the number of smoothing passes for the highest and lowest level can be set (set to 412 and 8 respectively), the maximum number of iterations for the various loops can be set

(to 1000 for the pressure loop and 150 for the velocity loop) and finally the accuracy for the three different loops can be modified (we have set 0.001 for the pressure and the velocity and 0.01 for the stress). Several tests have been run to determine the most suitable set of parameters to achieve convergence in the optimal amount of time, loosing the minimum accuracy possible.

Finally, also in the configuration file, we need to set the number processors in which the model will be running. For the final models I used 160 processors (4x10x4) each one with 1.5 GB of RAM.

Boundary conditions

Several kinds of boundary conditions can be selected for both the Navier-Stokes equation and the energy equations. In particular, for the Navier-Stokes equation we have used three different boundary conditions: free-slip, no-slip and imposed velocity. When applying an imposed velocity, the values of the velocity are read from an ASCII file previously generated with Matlab (bvel.dat, found in http://tinyurl.com/thesis-JRG). In this file, the velocities for each of the nodes of the top boundary are specified.

Initial temperature

There are several built in functions to set the initial temperature in CitcomS, but for the problem studied, where the initial thermal state is the key for the evolutions of the system, we need a more flexible way of establishing the initial temperature profile. In this case, the selected method reads the temperature value for each of the nodes in the domain from a binary file previously created with Matlab (an ASCII version of this file is included in http://tinyurl.com/thesis-JRG with the name reference_regmodtic.dat).

Rheology law

Several rheology laws can be selected with CitcomS and we have chosen one as defined in equation (2.29). This includes a non-linear composite mechanism and a pseudo-plastic behavior. Also, the parameters of the selected viscosity law

can be established, allowing us to change the pre-exponential factor, the activation energy and volume and the exponential coefficient. The values of these coefficients are set in the configuration file in the non-dimensional form.

Weak zones

To establish the location of the regions where the material have an imposed decreased viscosity, CitcomS reads the data form a binary file. This file is previously created using Matlab and contains one value for each of the nodes of the domain that ranges from one to zero, where on nodes with values of zero the viscosity remains unchanged, and the nodes with values of one have the maximum reduction of viscosity. These values are set so we never find a variation in the viscosity of more than a factor of three for two adjacent elements. An ASCII version of this file is included in http://tinyurl.com/thesis-JRG with the name reference_weakregion.dat

REFERENCES

Abt, D. L., K. M. Fischer, G. A. Abers, M. Protti, V. González, and W. Strauch (2010), Constraints on upper mantle anisotropy surrounding the Cocos slab from SK(K)S splitting, *Journal o f Geophysical Research*, *115*, B06316.

Álvarez-Gómez, J. A. (2009), Tectónica Activa y Geodinámica en el Norte de Centroamérica., Ph.D. thesis, Universidad Complutense de Madrid.

Anderson, D. L. (2001), Top-Down tectonics, *Science*, *293*, 2016-2018.

Anderson, M. L., P. Alvarado, G. Zandt, and S. Beck (2007), Geometry and brittle deformation of the subducting Nazca Plate, Central Chile and Argentina, *Geophysical Journal International*, *171*, 419–434.

Anderson, M. L., G. Zandt, E. Triep, M. Fouch, and S. Beck (2004), Anisotropy and mantle flow in the Chile-Argentina subduction zone from shear wave splitting analysis, *Journal o f Geophysical Research*, *31*, v.

Arcay, D., S. Lallemand, and M.-P. Doin (2008), Back-arc strain in subduction zones: Statistical observations versus numerical modeling, *Geochemistry Geophysics Geosystems*, *9*(5), Q05015.

Artemieva, I. M. (2006), Global 1°×1° thermal model TC1 for the continental lithosphere: Implications for lithosphere secular evolution, *Tectonophysics*, *416*, 245-277.

Barazangi, M., and B. L. Isacks (1979), Subduction of the Nazca plate beneath Peru: Evidence from spatial distribution of earthquakes, *Geophysical Journal of the Royal Astronomical Society*, *57*(3), 537-555.

Batchelor, G. K. (1967), *An introduction to Fluid Dynamics*, New York.

Becker, T. W. (2006), On the effect of temperature and strain-rate dependent viscosity on global mantle flow, net rotation, and plate-driving forces *Geophysical Journal International*, *167*, 943-957.

Becker, T. W. (2008), Azimuthal seismic anisotropy constrains net rotation of the lithosphere, *Geophysical Research Letters*, *35*, L05303.

Becker, T. W., and C. Faccenna (2009), A review of the role of subduction dynamics for regional and global plate motions, in *Subduction Zone Geodynamics*, edited by S. Lallemand and F. Funiciello, p. 3ç34, Int. J. Earth Sci.

Bellahsen, N., C. Faccenna, and F. Funiciello (2005), Dynamics of subduction and plate motion in laboratory experiments: Insights into the "plate tectonics" behavior of the Earth, *Journal of Geophysical Research*, *110*(1), B01401.

Benioff, H. (1954), Orogenesis and deep crustal structure: additional evidence from seismology, *Bull. Geol, Soc. Am.*, *65*, 385-400.

Billen, M. I. (2008), Modeling the Dynamics of Subducting Slabs, *Annual Reviews of Earth and Planetary Science*, *36*, 325-356.

Billen, M. I., and G. Hirth (2005), Newtonian versus non-Newtonian upper mantle viscosity: Implications for subduction initiation, *Geophysical Research Letters*, *32*, L19304.

Billen, M. I., and G. Hirth (2007), Rheologic controls on slab dynamics, *Geochemistry Geophysics Geosystems*, *8*(8), Q08012.

Bird, P. (1988), Formation of the Rocky Mountains, western United States: a continuum computer model, *Science*, *239*(4847), 1501-1507.

Blackwell, D., and M. Richards (2004), Geothermal Map of North America, American Assoc. Petroleum Geologist.

Bodri, L., and B. Bodri (1978), Numerical investigation of tectonic flow in island-arc areas, *Tectonophysics*, *50*, 163-175.

Bostrom, R. C. (1971), Westaward displacement of the lithosphere, *Nature*, *234*(5331).

Boussinesq, J. (1903), *Théory analytique de la chaleur mise en harmonie avec la thermodynamique et avec la théory de la lumière*, Paris.

Boutelier, D. A., and A. R. Cruden (2008), Impact of regional mantle flow on subducting plate geometry and interplate stress: insights from physical modelling, *Geophysical Journal International*, *174*, 719-732.

Briggs, L., V. E. Henson, and S. F. McCormick (2000), *A Multigrid Tutorial*, Siam.

Brooks, A. N., and T. J. R. Hughes (1982), Streamline upwind/Petrov-Galerkin formulations for convection dominated flows with particular emphasis

on the incompressible Navier-Stokes equation, *Computer Methods in Applied Mechanics and Engineering*, *32*, 199-259.

Brooks, E. (1981), A Petrov-Galerkin Finite Element Formulation for Convecton Dominated Flows. Unpub- lished doctoral thesis, California Institute of Technology, Pasadena, CA.

Buffett, B. A., and D. B. Rowley (2006), Plate bending at subduction zones: Consequences for the direction of plate motions *Earth and Planetary Science Letters*, *245*(1-2), 359-364.

Burkett, E., and M. I. Billen (2009), Dynamics and Implications of Slab Detachment Due to Ridge-Trench Collision, *Journal of Geophysical Research*, *114*(B12).

Butler, R. (2001), Dynamic Earth, edited.

Butterworth, N. P., L. Quevedo, G. Morra, and R. D. Muller (2012), Influence of overriding plate geometry and rheology on subduction *Geochemistry Geophysics Geosystems*, *13*, Q06W15.

Capitanio, F. A., and M. Faccenda (2012), Complex mantle flow around heterogeneous subducting oceanic plates, *Earth and Planetary Science Letters*, *353-354*, 29-37.

Capitanio, F. A., D. R. Stegman, L. N. Moresi, and W. Sharples (2010), Upper plate controls on deep subduction, trench migrations and deformations at convergent margins, *Tectonophysics*, *483*(1-2), 80-92.

Capitanio, F. A., C. Faccenna, S. Zlotnik, and D. R. Stegman (2011), Subduction dynamic and the origin of Andean orogeny and the Bolivian orocline, *Nature*, *480*, 83-86.

Carminati, E., and P. Petricca (2010), State of stress in slabs as a function of large-scale plate kinematics, *Geochemistry Geophysics Geosystems*, *11*, Q04006.

Carslaw, H. S., and J. C. Jaeger (1984), *Conduction of Heat in Solids*

, Clarendon Press, Oxford.

Chen, J., and S. D. King (1998), The influence of temperature and depth dependent viscosity on geoid and topography profiles from models of mantle convection, *Physics of the Earth and Planetary Interiors*, *106*, 75–92.

Christensen, U. R. (1996), The influence of trench migration on slab penetration into the lower mantle, *Earth and Planetary Science Letters*, *140*, 27-39.

Christeson, G. L., S. P. S. Gulick, H. J. A. van Avendonk, L. L. Worthington, R. S. Reece, and T. L. Pavlis (2010), The Yakutat Terrane; dramatic change in crustal thickness across the Transition Fault, Alaska, , *Geology*, *38*(10), 895-898.

Cízcová, H., J. van Hunen, and A. P. van den Berg (2007), Stress distribution within subducting slabs and their deformation in the transition zone, *Physics of the Earth and Planetary Interiors*, *161*, 202-214.

Cizkova, H., J. van Hunen, A. P. van den Berg, and N. J. Vlaar (2002), The influence of rheological weakening and yield stress on the interaction of slabs with the 670 km discontinuity, *Earth and Planetary Science Letters*, *193*(3-4), 447-457.

Conrad, C. P., and B. H. Hager (1999), Effects of plate bending and fault strength at subduction zones on plate dynamics, *Journal of Geophysical Research*, *104*(B8), 17551-17571.

Conrad, C. P., and C. Lithgow-Bertelloni (2002), How Mantle Slabs Drive Plate Tectonics, *Science*, *298*, 207-209.

Conrad, C. P., and C. Lithgow-Bertelloni (2004), The temporal evolution of plate driving forces: Importance of "slab suction" versus "slab pull" during the Cenozoic, *Journal o f Geophysical Research*, *109*(B10), B10407.

Crespi, M., M. Cuffaro, and C. Doglioni (2007), Space geodesy validation of the global lithospheric flow, *Geophysical Journal International*, *168*(2), 491-506.

Cruciani, C., E. Carminati, and C. Doglioni (2005), Slab dip vs. lithosphere age: No direct function, *Earth and Planetary Science Letters*, *238*, 298– 310.

Cuffaro, M., and D. M. Jurdy (2006), Microplate motions in the hotspot reference frame, *Terra Nova*, *18*(4), 276-281.

Cuffaro, M., and C. Doglioni (2007), Global kinematics in deep versus shallow hotspot reference frames, *GSA Spec.*, *430*, 359-374.

de Franco, R., R. Govers, and R. Wortel (2007), Numerical comparison of different convergent plate contacts: subduction channel and subduction fault, *Geophysical Journal International*, *171*(435 - 450).

di Giuseppe, E., J. van Hunen, F. Funiciello, C. Faccenna, and D. Giardini (2008), Slab stiffness control of trench motion: Insights from numerical models, *Geochemistry Geophysics Geosystems*, *9*, Q02014.

Dickinson, W., and T. Lawton (2001), Carboniferous to Cretaceous assembly and fragmentation of Mexico, *Geol. Soc. Am. Bull.*, *113*, 1142/1160.

Doglioni, C., P. Harabaglia, S. Merlini, F. Mongelli, A. Peccerillo, and C. Piromallo (1999), Orogens and slabs vs. their direction of subduction *Earth-Science Reviews*, *45*, 167-208.

Eberle, M. A., A. Grasset, and C. Sotin (2002), A numerical study of the interaction between the mantle wedge, subducting slab, and overriding plate, *Physics of the Earth and Planetary Interiors*, *134*, 191 - 202.

Enns, A., T. W. Becker, and H. Schmeling (2005), The dynamics of subduction and trench migration for viscosity stratification, *Geophysical Journal International*, *160*, 761-775.

Espurt, E., F. Funiciello, J. Martinod, B. Guillaume, V. Regard, C. Faccenna, and S. Brusset (2008), Flat subduction dynamics and deformation of the South American plate: Insights from analog modeling, *Tectonics*, *27*, TC3011.

Evans, B., J. T. Fredrich, and T. F. Wong (1990), The brittle-ductile transition in rocks: recent experimental and theoretical progress., in *In The Brittle-Ductile Transition in Rocks: The HeardVolume*, edited by A. G. Duba, W. B. Durham, J. W. Handin and H. F. Wang, pp. 1-20, Geophys. Monogr.

Faccenda, M., and F. A. Capitanio (2012), Development of mantle seismic anisotropy during subduction-induced 3-D flow, *Geophysical Research Letters*, *39*, L11305.

Faccenda, M., T. V. Gerya, and L. Burlini. (2009), Deep slab hydration induced by bending-related variations in tectonic pressure. , *Nature Geoscience*, *2*(790 - 793).

Faccenna, C., A. Heuret, F. Funiciello, S. Lallemand, and T. W. Becker (2007), Predicting trench and plate motion from the dynamics of a strong slab, *Earth and Planetary Science Letters*, *257*, 29-36.

Feng, M., S. van der Lee, and M. Assumpçâo (2007), Upper mantle structure of South America from joint inversion of waveforms and fundamental mode group velocities of Rayleigh waves, *Journal o f Geophysical Research*, *112*, B04312.

Forte, A. M., and J. X. Mitrovica (2001), Deep-mantle high viscosity flow and thermochem- ical structure inferred from seismic and geodynamic data, *Nature*, *410*, 1049-1056.

Fouch, M. J., and S. Rondenay (2006), Seismic anisotropy beneath stable continental interiors, *Physics of the Earth and Planetary Interiors*, *158*(2-4), 292-320.

Foulger, G. R. (2005), Mantle plumes: Why the current skepticism?, *Chinese Science Bulletin*, *50*(15), 1555-1560.

Funiciello, F., C. Faccenna, D. Gardini, and K. Regenauer-Lieb (2003), Dynamics of retreating slabs: 2. Insights fromthree-dimensional laboratory experiments., *Journal of Geophysical Research*, *108*(B2), 2207.

Funiciello, F., M. Moroni, C. Piromallo, C. Faccenna, A. Cenedese, and H. Bui (2006), Mapping mantle flow during retreating subduction: laboratory models analyzed by feature tracking, *Journal of Geophysical Research*, *111*(B3).

Funiciello, F., C. Faccenna, A. Heuret, S. Lallemand, E. D. Giuseppe, and T. W. Becker (2008), Trench migration, net rotation and slab–mantle coupling., *Earth and Planetary Science Letters*, *271*, 233-240.

Gerya, T. V. (2009), *Introduction to numerical geodynamic modelling*, Cambridge University Press, Cambridge, UK.

Gerya, T. V., D. Fossati, C. Cantieni, and D. Seward (2009), Dynamic effects of aseismic ridge subduction: numerical modelling, *European Journal of Mineralogy*, *21*, 649–661.

Goetze, C., and B. Evans (1979), Stress and temperature in the bending lithosphere as constrained by experimental rock mechanics, *Geophysical Journal of the Royal Astronomical Society*, *59*, 463-478.

Griffiths, R. W., R. I. Hackney, and R. D. van der Hilst (1995), A laboratory investigation of effects of trench migration on the descent of subducted slabs, *Earth and Planetary Science Letters*, *133*, 1-17.

Grip, A. E., and R. G. Gordon (2002), Young treack of hotspots and current plate velocities, *Geophysical Journal International*, *150*, 321-364.

Gudmundsson, O., and M. Sambridge (1998), A regionalized uppre mantle (RUM) seismic model, *Journal of Geophysical Research*, *103*, 7121-7136.

Guillou-Frottier, L., J. Buttles, and P. Olson (1995), Laboratory experiments on structure of subducted lithosphere, *Earth and Planetary Science Letters*, *19*(5), 814-833.

Gurnis, M., C. Eloy, and S. Zhong (1996), Free-surface formulation of mantle convection, part 2: Implication for subduction zone observables, *Geophysical Journal International*, *127*, 719-727.

Gutscher, M.-A., R. Maury, J.-P. Eissen, and E. Bourdon (2000a), Can slab melting be caused by flat subduction?, *Geology*, *28*(6), 535–538.

Gutscher, M.-A., W. Spakman, H. Bijwaard, and E. R. Engdahl (2000b), Geodynamics of flat subduction: Seismicity and tomographic constraints from the Andean margin, *Tectonics*, *19*(5), 814-833.

Gutscher, M.-A.-, J.-L. Olivet, D. Aslanian, J.-P. Eissen, and R. Maury (1999), The "lost Inca Plateau": Cause of flat subduction beneath Peru?, *Earth and Planetary Science Letters*, *171*(335-341).

Hager, B. H., and R. J. O'Connell (1981), A simple global model of plate dynamics and mantle convection, *Journal of Geophysical Research*, *86*, 4843-4867.

Hager, B. H., and M. A. Richards (1989), Long-wavelength variations in Earth's geoid: physical models and dynamical implications, *Philosophical Transactions of the Royal Society A*, *328*(309-327).

Hall, C. E., M. Gurnis, M. Sdrolias, L. Lavier, and R. D. Müller (2003), Catastrophic initiation of subduction following forced convergence across fracture zones, *Earth and Planetary Science Letters*, *212*, 15-30.

Hamzaa, V., F. S. J. Silva Dias, A. J. L. Gomesa, and Z. J. Delgadilho Terceros (2005), Numerical and functional representations of regional heat flow in South America, *Physics of the Earth and Planetary Interiors*, *152*, 223–256.

Han, L., and M. Gurnis (1999), How valid are dynamic models of subduction and convection when plate motions are prescribed? , *Physics of the Earth and Planetary Interiors*, *110*, 235-246.

Heuret, A., F. Funiciello, C. Faccenna, and S. Lallemand (2007), Plate kinematics, slab shape and back-arc stress: a comparison between laboratory models and current subduction zones, *Earth and Planetary Science Letters*, *256*, 473-483.

Hirth, G. (2003), Laboratory constraints on the rheology of the upper mantle, in *Plastic Deformation of Minerals and Rocks*, edited by S.-I. Karato and H.-R. Wenk, pp. 97-116, Mineralogical Society of America, Washington, DC,.

Hirth, G., and D. L. Kohlstedt (1995a), Experimental constraints on the dynamics of partially molten upper mantle: Deformation in the diffusion creep regime., *Journal of Geophysical Research*, *100*, 1981 - 2001.

Hirth, G., and D. L. Kohlstedt (1995b), Experimental constraints on the dynamics of partially molten upper mantle: Deformation in the dislocation creep regime., *Journal o f Geophysical Research*, *100*, 15441 - 15449.

Hirth, G., and D. Kohlstedt (1996), Water in the oceanic upper mantle: Implications for rheology, melt extraction and the evolution of the lithosphere, *Earth and Planetary Science Letters*, *144*(1-2), 93-108.

Hirth, G., and D. L. Kohlstedt (2003), Rheology of the upper mantle and the mantle wedge: A view from the experimentalists., in *Inside the Subduction Factory.*, edited by J. Eiler, pp. 83–105, AGU, Washington, D. C.

Hoernle, K., et al. (2008), Arc-parallel flow in the mantle wedge beneath Costa Rica and Nicaragua, *Nature*, *405*, 1095-1097.

Hughes, T. J. R. (2000), *The finite element method^linear static and dynamic finite element analysis*, Dover Publications.

Isacks, B., and P. Molnar (1969), Mantle earthquake mechanisms and the sinking of the lithosphere, *Nature*, *223*, 1121-1124.

Isacks, B. L., and M. Barazangi (1977), Geometry of Benioff zones: lateral segmentation and downwards bending of the subducted lithosphere, paper presented at Symposium on Island Arcs, Deep Sea Trenches and Back-Arc Basins, American Geophys. Union, New York, NY,.

Ita, J., and S. D. King (1994), Sensitivity of convection with an endothermic phase change to the form of governing equations, initial conditions, boundary conditions and equation of state, *Journal of Geophysical Research*, *99*, 15919–15938.

Jadamec, M. A., and M. I. Billen (2010), Reconciling surface plate motions with rapid three-dimensional mantle flow around a slab edge, *Nature*, *465*, 338-342.

Jadamec, M. A., and M. I. Billen (2012), The role of rheology and slab shape on rapid mantle flow: Three-dimensional numerical models of the Alaska slab edge, *Journal o f Geophysical Research*, *117*, B02304.

Jarrard, R. D. (1986), Relations among subduction parameters, *Reviews of Geophysics*, *24*(2), 217-284.

Jischke, M. C. (1975), On the dynamics of descending lithospheric plates and slip zones., *Journal of Geophysical Research*, *80*, 4809-4813.

Karato, S. I., and P. Wu (1993), Rheology of the upper mantle: a synthesis, *Science*, *260*, 771-778.

Kincaid, C., and P. Olson (1987), An experimental study of subduction and slab migration., *Journal of Geophysical Research*, *92*(B13), 13832-13840.

Kincaid, C., and I. S. Sacks (1997), Thermal and dynamical evolution of the upper mantle in subduction zones, *Journal of Geophysical Research*, *102*, 12295-12315.

Kincaid, C., and R. W. Griffiths (2003), Laboratory models of the thermal evolution of the mantle during rollback subduction., *Nature*, *425*, 58-62.

King, S. D. (2007), Downwellings and the Fate of Subducting Slabs: Constraints from Seismology, Geoid, Topography, Geochemistry, and Petrology, in *Mantle dynamics*, edited by D. Bercovici, pp. 325-370.

Kneller, E. A., and P. E. van Keken (2007), Trench-parallel flow and seismic anisotropy in the Mariana and Andean subduction systems, *Nature*, *450*, 1222-1224.

Kneller, E. A., and P. E. van Keken (2008), Effect of three-dimensional slab geometry on deformation in the mantle wedge: Implications for shear wave anisotropy, *Geochemistry Geophysics Geosystems*, *9*(1), Q01003.

Kohlstedt, D. L., and E. M. Zimmerman (1996), Rheology of partialy molten mantle rocks, *Annual Reviews of Earth and Planetary Science*, *24*, 41 - 54.

Korenaga, J., and S.-I. Karato (2008), A new analysis of experimental data on olivine rheology, *Journal of Geophysical Research*, *113*, B02403.

Kukaèka, M., and C. Matyska (2004), Influence of the zone of weakness on dip angle and shear heating of subducted slabs, *Physics of the Earth and Planetary Interiors*, *141*, 243-252.

Lallemand, S., A. Heuret, and D. Boutelier (2005), On the relationships between slab dip, back-arc stress, upper plate absolute motion, and crustal nature in subduction zones, *Geochemistry Geophysics Geosystems*, *6*, Q09006.

Lee, C.-K., S.-C. Han, and B. Steinberger (2011), Influence of variable uncertainties in seis- mic tomography models on contraining mantle viscosity from geoid observations, *Physics of the Earth and Planetary Interiors*, *184*(51-62).

Long, M. D., and P. G. Silver (2008), The subduction zone flow field from seismic anisotropy: A global view, *Science*, *319*(5861), 315-318.

Long, M. D., and P. G. Silver (2009), Mantle flow in subduction systems: the subslab flow field and implications for mantle dynamics, *Journal o f Geophysical Research*, *114*, B10312.

Long, M. D., and T. W. Becker (2010), Mantle dynamics and seismic anisotropy, *Earth and Planetary Science Letters*, *297*, 341–354.

Manea, V., and M. Gurnis (2007), Subduction zone evolution and low viscosity wedges and channels, *Earth and Planetary Science Letters*, *264*, 22–45.

Marton, G., and R. Buffler (1994), Jurrassic reconstruction of the Gulf of Mexico basin, *Int. Geol. Rev.*, *36*, 545-586.

McKenzie, D. P. (1967), Some remarks on heat flow and gravity anomalies, *Journal of Geophysical Research*, *72*, 6261 - 6273.

McKenzie, D. P. (1969), Speculations on the consequences and causes of plate motions, *Geophysical Journal of the Royal Astronomical Society*, *18*, 1-32.

Melosh, H. J., and A. Rafesky (1980), The dynamical origin of subduction zone topog- raphy, *Geophysical Journal of the Royal Astronomical Society*, *60*, 333-354.

Moresi, L. N., and M. Gurnis (1996), Constraints on the lateral strength of slabs from three-dimensional dynamic flow models, *Earth and Planetary Science Letters*, *138*, 15-28.

Müller, R. D., W. R. Roest, J. Y. Royer, L. M. Gahagan, and J. G. Sclater (1997), Digital isochrons of the worlds ocean floor, *Journal o f Geophysical Research*, *102*, 3211-3214.

Muñoz, M. (2005), No flat Wadati–Benioff Zone in the central and southern central Andes, *Tectonophysics*, *395*, 41– 65.

O'Driscoll, L. J., E. D. Humphreys, and F. Saucier (2009), Subduction adjacent to deep continental roots: Enhanced negative pressure in the mantle wedge, mountain building and continental motion, *Earth and Planetary Science Letters*, *280*(1-4), 61-70.

O'Neil, C., D. Müller, and B. Steinberg (2005), On the uncertainties in hotspot recosntruction and the significance of moving hotspot reference fremes, *Geochemistry Geophysics Geosystems*, *6*.

Olbertz, D., and M. J. R. Wortel (1997), Trench migration and subduction zone geometry, *Geophysical Research Letters*, *240*(3), 221-224.

Pardo, M., and G. Suarez (1995), Shape of the Subducted Rivera and Cocos Plates ins Southern Mexico - Seismic and tectonic implications, *Journal of Geophysical Research*, *100*(B7), 12357 - 12373.

Parsons, B., and J. G. Sclater (1977), An analysis of the variation of the ocean floor bathymetry heat flow and with age, *Journal o f Geophysical Research*, *82*(5), 803-827.

Pérez-Campos, X., Y. Kim, A. Husker, P. M. Davis, R. W. Clayton, A. Iglesias, J. F. Pacheco, S. K. Singh, V. C. Manea, and M. Gurnis (2008), Horizontal subduction and truncation of the Cocos Plate beneath central Mexico, *Geophysical Research Letters*, *35*, L18303.

Pérez-Gussinyé, M., A. R. Lowry, J. Phipps Morgan, and A. Tassara (2008), Effective elastic thickness variations along the Andean margin and their relationship to subduction geometry, *Geochemistry Geophysics Geosystems*, *9*(2), Q02003.

Pindell, J. L., and S. F. Barrett (1990), Geologic evolution of the Caribbean: A plate-tectonic perspective, in *The Geology of North America*, edited by Dengo and J. E. Case, pp. 405-432, Geol. Society of America.

Piromallo, C., T. W. Becker, F. Funiciello, and C. Faccenna (2006), Three-dimensional instantaneous mantle flow induced by subduction, *geophysical Research Letters*, *33*, L08304.

Polet, J., . , P. G. Silver, S. Beck, T. Wallace, G. Zandt, S. Ruppert, R. Kind, and A. Rudloff (2000), Shear wave anisotropy beneath the Andes from the BANJO, SEDA and PISCO experiments, *Journal o f Geophysical Research*, *105*, 6287-6304.

Quinquis, M. E. T., S. J. H. Buiter, and S. Ellis (2011), The role of boundary conditions in numerical models of subduction zone dynamics, *Tectonophysics*, *497*, 57 - 70.

Rabble, W., I. Koulakov, A. N. Dinc, and A. Jakovlev (2011), Arc-parallel shear deformation and escape flow in the mantle wedge of the Central America subduction zone: Evidence from P wave anisotropy, *Geochemistry Geophysics Geosystems*, *12*(6), Q05S31.

Ramage, A., and A. N. Wathen (1994), Iterative solution techniques for the Stokes and Navier-Stokes equations, *International Journal of Numerical Methods*, *19*, 67-83.

Ranalli, G. (1995), *Rheology of the Earth*, Chapman & Hall.

Regenauer-Lieb, K., D. A. Yuen, and J. Branlund (2001), The initiation of subduction: criticality by addition of water, *Science*, *294*, 578.580.

Replumaz, A., A. M. Negredo, A. Villaseñor, and S. Guillot (2010), Indian continental subduction and slab break-off during Tertiary collision, *Terra Nova*, *22*, 290-296.

Ribe, N. M. (2010), Bending mechanics and mode selection in free subduction: a thin-sheet analysis *Geophysical Journal International*, *180*(2), 559-576.

Ricard, Y., C. Doglioni, and R. Sabadini (1991), Differential rotation between lithosphere and mantle: a consequence of lateral mantle variations, *Journal of Geophysical Research*, *96*, 8407-8415.

Richter, F., and D. P. McKenzie (1978), Simple plate models of mantle convection, *Journal o f Geophysical Research*, *4*(4), 441-471.

Riguzzi, F., G. Panza, P. Varga, and C. Doglioni (2009), Can Earth's rotation and tidal despinning drive plate tectonics?, *Tectonophysics*.

Roda, M., A. M. Marotta, and M. I. Spalla (2011), The effects of the overriding plate thermal state on the slab dip in an ocean-continent subduction system, *Comptes Rendus Geoscience*, *343*, 323 – 330.

Rodríguez-González, J., A. M. Negredo, and M. I. Billen (2012), The role of the overriding plate thermal state on slab dip variability and on the occurrence of flat subduction, *Geochemistry Geophysics Geosystems*, *13*, Q01002.

Rogers, R. (2003), Jurassic–Recent tectonic and stratigraphic history of the Chortis block of Honduras and Nicaragua, University of Texas, Austin.

Rogers, R. D., H. Karason, and R. D. van der Hilst (2002), Epeirogenic uplift above a detached slab in northern Central America, *Geology*, *30*(11), 1031-1034.

Royden, L. H., and L. Husson (2006), Trench motion, slab geometry and viscous stresses in subduction systems, *Geophysical Journal International*, *167*, 881–905.

Russo, R., and P. G. Silver (1994), Trench-Parallel Flow Beneath the Nazca Plate from Seismic Anisotropy,, *Science*, *263*, 1105-1111.

Schellart, W. P. (2004), Kinematics of subduction and subduction-induced flow in the upper mantle., *Journal of Geophysical Research*, *109*(B7), B07401.

Schellart, W. P. (2007), The potential influence of subduction zone polarity on overriding plate deformation, trenchmigration and slab dip angle, *Tectonophysics*, *445*(363 - 372).

Schellart, W. P., J. Freeman, D. R. Stegman, L. Moresi, and D. May (2007), Evolution and diversity of subduction zones controlled by slab width, *Nature*, *446*, 308-311.

Schenk, O., and K. Gärtner (2004), Solving Unsymmetric Sparse Systems of Linear Equations with PARDISO, *Journal of Future Generation Computer Systems*, *20*(3), 475-487.

Schenk, O., and K. Gärtner (2006), On fast factorization pivoting methods for symmetric indefinite systems, *Elec. Trans. Numer. Anal.*, *23*, 158-179.

Schmeling, H. (1989), Compressible convection with constant and variable viscosity: the effect on slab formation, geoid and topography,, *Journal of Geophysical Research*, *94*(B9), 12463-12481.

Schmeling, H., R. Monz, and D. C. Rubie (1999), The influence of olivine metastability on the dynamics of subduction, *Earth and Planetary Science Letters*, *165*, 55-66.

Schmeling, H., et al. (2007), A benchmark comparison of subduction models, *Physics of the Earth and Planetary Interiors*, *171*, 198-233.

Schmid, C., S. Goes, S. van der Lee, and D. Giardini (2002), Fate of the Cenozoic Farallon slab from a comparison of kinematic thermal modeling with tomographic images, *Earth and Planetary Science Letters*, *204*, 17-32.

Schubert, G., D. L. Turcotte, and P. Olson (2001), *Mantle convection in the Earth and Planets*, Cambridge University Press.

Shewchuk, J. R. (1994), An Introduction to the conjugate gradient method without the agonizing pain, edited.

Sigloch, K., N. McQuarrie, and G. Nolet (2008), Two-stage subduction history under North America inferred from multiple-frequency tomography, *Nature geoscience*, *1*, 458-462.

Soto, G. L., J. F. Ni, S. P. Grand, E. Sandvol, W. Valenzuela, M. G. Speziale, J. M. Gómez González, and T. Domínguez Reyes (2009), Mantle flow in the Rivera–Cocos subduction zone, *Geophysical Journal International*, *179*, 1004–1012.

Spiegel, E. A., and G. Veronis (1960), On the Boussinesq approximation for a compressible fluid, *Astrophysical Journal*, *131*, 442-447.

Stegman, D. R., R. Farrington, F. A. Capitanio, and W. P. Schellart, 2010. A regime diagram for subduction styles from 3-d numerical models of free subduction (2010), A regime diagram for subduction styles from 3-d numerical models of free subduction, *Tectonophysics*, *483*(29 - 45).

Stegman, D. R., J. Freeman, W. P. Schellart, L. Moresi, and D. May (2006), Influence of trench width on subduction hinge retreat rates in 3-d models of slab rollback, *Geochemistry Geophysics Geosystems*, *7*(1 - 22).

Stein, C. A., and S. A. Stein (1992), A model for the global variation in oceanic depth and heat flow with lithospheric age, *Nature*, *359*, 123-129.

Steinberger, B. (2000), Slabs in the lower mantle – results of dynamic modelling compared with tomographic images and the geoid,, *Physics of the Earth and Planetary Interiors*, *118*, 241-257.

Steinberger, B., R. Sutherland, and R. J. O'Connell (2004), Prediction of Emperor-Hawaii seamount locations from a revised model of global plate motion and mantle flow, *Nature*, *430*(6996), 167-173.

Stevenson, D. J., and J. S. Turner (1977), Angle of subduction, *Nature*, *270*(5635), 334-336.

Suárez, G., T. Monfret, and G. Wittlinger (1990), Geometry of subduction and depth of the seismogenic zone in the Guerero gap, Mexico, *Nature*, *345*, 336-338.

Tan, E., E. Choi, P. Thoutireddy, M. Gurnis, and M. Aivazis (2006), GeoFramework: Coupling multiple models of mantle convection within a computational framework, *Geochemistry Geophysics Geosystems*, *7*, Q06001.

Tetzlaff, M., and H. Schmeling (2000), The influence of olivine metastability on deep subduction of oceanic lithosphere *Physics of the Earth and Planetary Interiors*, *120*(1-2), 29-38.

Tetzlaff, M., and H. Schmeling (2009), Time-dependent interaction between subduction dynamics and phase transition kinetics *Geophysical Journal International*, *178*(2), 826-844.

Toth, J., and M. Gurnis (1998), Dynamics of subduction initiation at pre-existing fault zones, *Journal o f Geophysical Research*, *103*(B8), 18053-18067.

Tovish, A., G. Schubert, and B. P. Luyenduk (1978), Mantle Flow Pressure and the Angle of Subduction: Non-Newtonian Corner Flows, *Journal of Geophysical Research*, *80*(B12), 5892-5898.

Turner, S., and C. Hawkesworth (1998), Using geochemistry to map mantle flow beneath the Lau Basin, *Geology*, *26*(1019-1022).

Uyeda, S., and H. Kanamori (1979), Back arc opening and the mode of subduction, *Journal of Geophysical Research*, *84*, 1049–1061.

van Dinther, Y., G. Morra, F. Funiciello, and C. Faccenna (2010), Role of the overriding plate in the subduction process: Insights from numerical models, *Tectonophysics*, *484*, 74 - 86.

van Hunen, J., and M. B. Allen (2011), Continental collision and slab break-off: A comparison of 3-D numerical models with observations, *Earth and Planetary Science Letters*, *302*(1-2), 37-37.

van Hunen, J., A. P. van den Berg, and N. J. Vlaar (2001), Latent heat effects of the major mantle phase transitions on low-angle subduction *Earth and Planetary Science Letters*, *190*(3-4), 125-135.

van Hunen, J., A. P. van den Berg, and N. J. Vlaar (2002a), The impact of the South-American plate motion and the Nazca Ridge subduction on the flat subduction below South Peru, *Geophysical Research Letters*, *182*, 157-169.

van Hunen, J., A. P. van den Berg, and N. J. Vlaar (2002b), On the role of subducting oceanic plateaus in the development of shallow flat subduction, *Tectonophysics*, *352*, 317-333.

van Hunen, J., A. P. van den Berg, and N. J. Vlaar (2004), Various mechanisms to induce present-day shallow flat subduction and implications for the younger Earth: a numerical parameter study, *Earth and Planetary Science Letters*, *146*, 179-194.

van Keken, P. E., B. Kiefer, and S. M. Peacock (2002), High-resolution models of subduction zones: implications for mineral dehydration reactions and the transport of water into the deep mantle. , *Geol. Geochem. Geophys.*, *3*(10), 1056.

Villaseñor, A., W. Spakman, and E. R. Engdahl (2003), Influence of regional travel times in global tomographic models, *Geoph. Res. Abs.*, *5*, EAE03-A-08614.

Winder, R. O., and S. M. Peacock (2001), Viscous forces acting on subducting lithosphere, *Journal of Geophysical Research*, *106*(B10), 21937-21951.

Yamato, P., L. Husson, J. Braun, C. Loiselet, and C. Thieulot (2009), Influence of surrounding plates on 3D subduction dynamics, *Geophysical Research Letters*, *36*, L07303.

Yoshida, M. (2004), Possible effects of lateral viscosity variations induced by plate-tectonic mechanism on geoid inferred from numerical models of mantle convection, *Physics of the Earth and Planetary Interiors*, *147*, 67-85.

Zhong, S. (2001), Role of ocena-continent contrast and continental keels on plate motion, net rotation of lithosphere, and geoid, *Journal of Geophysical Research*, *106*, 703-712.

Zhong, S., and M. Gurnis (1995), Mantle convection with plates and mobile, faulted plate margins, *Science*, *267*, 838-843.

Zhong, S., M. T. Zuber, L. N. Moresi, and M. Gurnis (2000), The role of temperature-dependent viscosity and surface plates in spherical shell models of mantle convection, *Journal of Geophysical Research*, *105*, 11063 - 11082.fu